NPSEC-98-009

NAVAL POSTGRADUATE SCHOOL

Monterey, California

Photonic Sampling of RF and Microwave Signals

by

Phillip. E. Pace and John P. Powers

March 16, 1998

Approved for public release; distribution is unlimited.

Prepared for: Center for Reconnaissance Research, Naval Postgraduate School, Monterey, CA 93943.

NAVAL POSTGRADUATE SCHOOL
Monterey, California

CAPT James Burin
Superintendent

R. Elster
Provost

This report was sponsored by NPS Center for Reconnaissance Research.

Approved for public release; distribution is unlimited.

The report was prepared by:

John P. Powers
Professor
Department of Electrical and
Computer Engineering

P. E. Pace
Associate Professor
Department of Electrical and
Computer Engineering

Reviewed by:

Herschel H. Loomis, Jr.
Chairman
Department of Electrical and
Computer Engineering

Released by:

David W. Netzer
Associate Provost and
Dean of Research

REPORT DOCUMENTATION PAGE

Form Approved
OMB No. 0704-0188

Public reporting burden for the collection of information is estimated to average 1 hour per response, including the time for reviewing instructions, searching existing data sources, gathering and maintaining the data needed, and completing and reviewing the collection of information. Send comments regarding this burden estimate or any other aspect of this collection of information, including suggestions for reducing this burden to Washington Headquarters Services, Directorate for Information Operations and Reports, 1215 Jefferson Davis Highway, Suite 1204, Arlington VA 22202-4302, and to the Office of Management and Budget, Paperwork Reduction Project (0704-0188), Washington DC 20503.

1. AGENCY USE ONLY (Leave blank)	2. REPORT DATE	3. REPORT TYPE AND DATES COVERED
	March 16, 1998	Technical Report

4. TITLE AND SUBTITLE

5. FUNDING NUMBERS

6. AUTHOR(S)

Phillip. E. Pace, and John P. Powers

7. PERFORMING ORGANIZATION NAME(S) AND ADDRESS(ES)

Department of Electrical and Computer Engineering
Naval Postgraduate School
Monterey, CA 93943-5000

8. PERFORMING ORGANIZATION REPORT NUMBER

NPS-EC-98-009

9. SPONSORING/MONITORING AGENCY NAME(S) AND ADDRESS(ES)

Center for Reconnaissance Research
Department of Electrical and Computer Engineering
Naval Postgraduate School
Monterey, CA 93943

10. SPONSORING/MONITORING AGENCY REPORT NUMBER

11. SUPPLEMENTARY NOTES

The views expressed in this report are those of the author and do not reflect the official policy or position of the Department of Defense or the United States Government.

12a. DISTRIBUTION/AVAILABILITY STATEMENT

Approved for public release; distribution is unlimited.

12b. DISTRIBUTION CODE

A

13. ABSTRACT (Maximum 200 words)

Optical sampling of wideband microwave signals has recently gained a lot of attention due to the availability of high repetition rate mode-locked lasers. This report examines the state-of-the-art in mode-locked lasers and their performance requirements when used for wideband signal sampling. The required sample time uncertainty (jitter) and optical pulsewidth are shown as a function of the Nyquist sampling rate. Nonuniform sampling theory is also presented as a means to quantify the sampling jitter from spectrum analyzer measurements. Various laser configurations and mode locking techniques are discussed with emphasis on the measurement of the laser performance. A summary of the measured pulsewidth and minimum jitter times for a number of lasers reported in the literature is presented. The design for a (NRL) sigma laser currently being constructed at NPS is also discussed. To relax the requirements on a laser's required sample time uncertainty, 1st and 2nd order optical sigma-delta architectures are investigated. Also introduced is an undersampling, optical DFT receiver concept that could allow frequency measurements beyond Nyquist.

14. SUBJECT TERMS

Optical sampling, fiber laser, sampling architectures, mode locked laser, jitter, optical sigma-delta, undersampling, optical DFT

15. NUMBER OF PAGES

95

16. PRICE CODE

17. SECURITY CLASSIFICATION OF REPORT	18. SECURITY CLASSIFICATION OF THIS PAGE	19. SECURITY CLASSIFICATION OF ABSTRACT	20. LIMITATION OF ABSTRACT
UNCLASSIFIED	UNCLASSIFIED	UNCLASSIFIED	SAR

Contents

Table of Contents vi

List of Figures ix

List of Tables xi

Acknowledgements xiii

Overview 1

I Laser Sampling and Jitter Effects 3

1 Introduction 3

2 Modelocking Techniques 5

3 Laser Configurations 6

4 Pulse Shortening and Resonator Stabilization in Modelocked Lasers 7
4.1 Pulse Shortening . . . 7
4.2 Resonator Stabilization . . . 9

5 Laser Performance Measurements 9
5.1 Pulse Repetition Frequency . . . 9
5.2 Autocorrelator Measurement of Pulse Width . . . 10
5.3 Laser Wavelength and Spectral Width . . . 10
5.4 Jitter Measurement . . . 10
5.5 Laser Jitter Measurement from Fundamental Spectrum . . . 15

6 Measurement Results 15
6.1 Measured Pulse Width Performance . . . 15
6.2 Measured Jitter Performance . . . 18

7 NPS Sigma Laser 18
7.1 Resonator Stabilization . . . 20

8 Summary of Laser Sampling Performance Measures 20

II Optical Signal Processing 23

9 Design of Optical Oversampling Architectures 23
9.1 Introduction . . . 23
9.1.1 Advantages of Oversampling Microwave Signals . . . 23
9.1.2 Integrated Optical Processing . . . 23
9.2 ΣΔM Design . . . 24

9.2.1 Signal-to-Noise Relationships . . . 24
9.2.2 First-order ΣΔ Modulator . . . 25
9.2.3 Second Order ΔΣ Modulator . . . 31
9.2.4 L Stable Loops . . . 31
9.3 Integrated Optical ΣΔM Design . . . 35
9.3.1 First-Order Integrated Optical ΣΔM . . . 35
9.3.2 Second-Order ΣΔM . . . 37
9.4 Fiber Lattice Structures . . . 39
9.4.1 Transfer Functions . . . 39
9.4.2 Testing of Fiber Lattice Models . . . 42
9.4.3 First-Order Optical ΣΔM Using Fiber Lattice Accumulator Model . . . 50
9.4.4 Second-Order Sigma-Delta Modulator with Fiber Lattice Accumulator Model 55
9.5 Free-Space S-SEED ΣΔM Designs . . . 56

10 Optical Undersampling DFT Receivers **58**
10.1 Introduction . . . 58
10.2 The DFT and SNS Relationship . . . 59
10.3 Optical DFT Receiver . . . 64

11 Non-Uniform Sampling Jitter **65**
11.1 Spectrum Representations of Non-Uniformly Sampled Signals . . . 65
11.1.1 Specific Case . . . 67
11.1.2 Properties . . . 68
11.1.3 Signal-to-Noise Ratio . . . 68
11.1.4 Independent Random Sampling . . . 69
11.1.5 Simulation Results . . . 70
11.1.6 Other Jitter Models . . . 74
11.2 Reconstruction of Signals from Nonuniform Samples . . . 74
11.3 Summary of Optical Signal Processing . . . 75

III Appendices **77**

A Review of Derivations **77**
A.1 System Jitter . . . 77
A.2 System pulse width . . . 77

B Review of Autocorrelator Measurements **78**

C Characteristic Functions **81**

IV Bibliography **83**

List of Figures

1 Maximum allowed laser jitter vs. pulse repetition frequency in ADCs for 8-, 10-, 12-, and 14-bit converters. . . . 4
2 Maximum allowed ΔT (laser pulse width plus optical propagation time in modulator electrodes) vs. pulse repetition frequency for A-to-D converters for 8-, 10-, 12-, and 14-bit convertors. . . . 5
3 Conceptual layout of a figure-eight laser. (After [2].) . . . 6
4 Conceptual layout of the NRL "sigma-laser" (or "σ-laser"). (After [8].) . . . 7
5 Ring laser with both positive and negative pulse dispersion and output pulse autocorrelation measurements. (From Ref. [9].) . . . 8
6 Optical autocorrelator for use in measuring pulse width of short optical pulses. . . . 10
7 Conceptual spectrum of laser pulse train at (a) the PRF fundamental and (b) the n-th harmonic of the PRF frequency. In part (b) the dotted curve shows the amplitude noise effects without any jitter; the solid curve is the combined effects of amplitude and jitter noise. The jitter noise dominates. . . . 12
8 Representative plot of $L(f)$ from two modelocked lasers. The spectra are referenced from the fundamental frequency of the laser pulse train. From Ref. [19]. . . . 14
9 Experimentally measured laser pulse width vs. pulse repetition frequency in modelocked lasers. Also shown (solid line) is the theoretical curve for the maximum pulse width plus transit time of a 10-bit ADC system that is sampled at the Nyquist frequency rate of twice the value of the maximum frequency in the signal. . . . 16
10 Experimentally measured laser jitter vs. pulse repetition frequency in modelocked lasers. Also shown (solid line) is the theoretical curve for the maximum jitter allowed for a 10-bit ADC system that is sampled at the Nyquist frequency rate of twice the value of the maximum frequency in the signal. . . . 18
11 Design concept for NPS sigma laser. . . . 19
12 Resonator stability circuit for NPS sigma laser. . . . 21
13 a) An example of a uniform multilevel quantization characteristic that is represented by linear gain G and error e, b) For two-level quantization the gain is arbitrary. (Adapted from [57]). . . . 24
14 In-band quantization noise power density with a) Nyquist sampling, b) oversampling factor of 4, and c) output of a LPF with 3 dB bandwidth of $f_s/2$. . . . 26
15 Block diagram of a general first-order ΣM configuration. . . . 27
16 Response of a first-order multilevel $\Sigma\Delta$ [57]. . . . 27
17 First-order sampled data noise model. . . . 28
18 Sampled data first-order $\Delta\Sigma$ modulator using a single delay accumulator. . . . 29
19 RMS spectral density. (Adapted from Ref. [57]). . . . 30
20 First-order single-bit $\Sigma\Delta$ showing (a) block diagram, (b) comparator output, and (c) accumulator output. . . . 32
21 Block diagram of a second-order all-electronic $\Sigma\Delta$M. . . . 33
22 Second-order single-bit $\Sigma\Delta$ showing (a) block diagram, (b) comparator output, and (c) accumulator output. . . . 33
23 RMS noise that enters the signal band [57]. . . . 34
24 Block diagram of a second-order $\Sigma\Delta$ modulator with variable gain accumulators. . . . 35
25 First-order integrated optical $\Sigma\Delta$M, (a) Block diagram,(b) the comparator output, and (c) the comparator input using ideal H_{12}. . . . 36
26 Schematic diagram of a MZI in a push-pull configuration. . . . 36

27 Transfer functions for the MZIs. 37
28 Second-order integrated optical ΣΔM. (a) Block diagram, (b) simulation results with ideal H_{12} and H_{21} and (c) intermediate signals at inputs to Magnitude MZIs. 38
29 General fiber lattice structure. 39
30 $H_{21}(z)$ fiber lattice structure. 40
31 Generation of $H_{21}(z)$ fiber lattice structure. 41
32 $H_{12}(Z)$ fiber lattice structure. 42
33 Generation of $H_{12}(z)$ fiber lattice structure. 43
34 $H_{21}(z)$ Simulink model. (From [64].) 43
35 Tuning for monotonically increasing response. (From [64].) 44
36 (a) Optical gain vs. a_1, (b) $H_{21}(z)$ accumulation rate vs. a_1, (c) $H_{12}(z)$ accumulation rate vs. a_1. (From [64].) 47
37 Modified Simulink model of $H_{12}(z)$ fiber lattice structure. (From [64].) 48
38 Effect of in-line gain on accumulation rate. (From [64].) 49
39 Effect of reducing Accumulate Down G. (From [64].) 50
40 Optical first-order sigma-delta (a) ramp input, (b) $H_{12}(z)$ fiber lattice structure output, and (c) first-order sigma-delta modulator output. (From [64].) 51
41 Ideal first-order sigma-delta (a) ramp input, (b) $H_{12}(z)$ transfer function output, and (c) first-order sigma-delta modulator output. (From [64].) 52
42 Effect of Accum Down G on first-order sigma-delta modulator output (a) Accum Down $G = 1.62$, (b) Accum Down $G = 1.5$, (c) Accum Down $G = 1.38$, and (d) Accum Down $G = 1.26$. (From [64].) 53
43 Accumulation with Accum Up equal Accum Down (a) $H_{12}(z)$ output, (b) discrete output. (From [64].) 54
44 First-order sigma-delta discrete output with 0.43 V input. (From [64].) 54
45 Second-order sigma-delta accumulation (a) $H_{21}(z)$ output, (b) $H_{12}(z)$ output, and (c) modulator output. (From [64].) 55
46 Block diagram of recursive error diffusion modulator. (From Ref. [70].) 57
47 First-order interferometric error diffusion modulator. (From Ref. [70].) 57
48 First-order non-interferometric error diffusion modulator. (From Ref. [70].) 58
49 (a) z-plane mapping of an input analog signal, (b) sampled frequency output. 60
50 DFT mapping for input frequencies $f = 0$ to 23 for (a) $f_{s1} = 10$ and (b) $f_{s2} = 11$. . 62
51 Block diagram of a two-channel optical undersampling DFT/SNS receiver. 64
52 A diffraction grating directs two wavelengths λ_1 and λ_2 into two directions θ_1, θ_2 (spectrum analyzer). 65
53 Non-uniformly sampled data sequence. 66
54 Line spectra at integer multiples of the sampling frequency. 68
55 Asynchronous spectral averaging. 71
56 Simulation results using a four-term Blackman-Harris window ($E_B = 2$), a sampling frequency of 20 MHz, N=256, f_0=9,135,780 Hz and σ_r =0.001. (From [79].) 71
57 Simulation results using a four-term Blackman-Harris window ($E_B = 2$), a sampling frequency of 20 MHz, N=512, f_0=9,135,780 Hz and σ_r =0.001. (From [79].) 72
58 Simulation results using a four term Blackman-Harris window ($E_B = 2$), a sampling frequency of 20 MHz, N=1024, f_0=9,135,780 Hz and σ_r =0.001. (From [79].) 72
59 Simulation results using a four-term Blackman-Harris window ($E_B = 2$), a sampling frequency of 20 MHz, N=1024, f_0=4,567,890 Hz and σ_r =0.001. (From [79].) 73
60 Simulation results using a four term Blackman-Harris window ($E_B = 2$), a sampling frequency of 20 MHz, N=1024, f_0=4,567,890 Hz and σ_r =0.01. (From [79].) 73

61 Representative autocorrelation curves. (a) Ideal square coherent pulse. (b) Partially coherent pulse. (c) Representative coherent pulse, showing location of pulse width measurement. 80

List of Tables

1 Measured pulse width of modelocked lasers. 17
2 Measured jitter performance of modelocked lasers. 20
3 $\Sigma\Delta$ Resolution Summary for OSR = 2. 34
4 Optical Gain: Monotonically Increasing Response. (From [64].) 45
5 $H_{12}(z)$ Accumulation Rate: Monotonically Increasing Response. (From [64].) 45
6 $H_{21}(z)$ Accumulation Rate: Monotonically Increasing Response. (From [64].) 45
7 $H_{12}(z)$ Optical and In-Line Gain Necessary for Steady State Response. (From [64].) 46
8 $H_{12}(z)$ Optical Gain Necessary for Steady Accumulation Down. (From [64].) 46
9 Input Frequency and Resulting DFT Bins for Two Channel Example 63
10 Integer Values for the $m_1 = 4$, $m_2 = 3$, and $m_3 = 5$ Example 63
11 Ratio of autocorrelation width to intensity pulse width for three standard mathematical representations of optical pulses. 81

Acknowledgements

The authors wish to thank the sponsors of the Center for Reconnaissance Research at the Naval Postgraduate School for their encouraging support in this research. We acknowledge the many analytic and experimental contributions of our graduate officer-students: Mr. Adam Atherton, Edwards AFB; LT Bill Ringer, USN; LT Jim Butler, USN; and CAPT Rich Leino, USMC. Also, we want to thank Dr. Irl Duling III, Dr. Mike Dennis, and Dr. Tom Carruthers at the Optical Sciences Division (Code 5670) of the Naval Research Laboratory for offering guidance, lending parts, and providing splicing time to us in designing and constructing the NPS fiber sigma laser.

Overview

This report covers aspects of using optical sampling techniques to sample rf and microwave signals for subsequent digitization and processing.

In Part I, we consider the required temporal jitter and required laser pulsewidths to achieve Nyquist sampling of a 10 GHz bandwidth signal at 10 bits of resolution. The 15.5-fs jitter requirement is more severe than the 2.4-ps laser pulsewidth requirement and presents a significant challenge to find a pulsed laser with less jitter than this. After performing a literature investigation, it was found that actively modelocked fiber lasers achieve operating performance close to that desired. In particular, the Naval Research Laboratory has produced a "sigma" fiber laser for high data rate communications that has a picosecond pulsewidth and a temporal jitter on the order of 100 femtoseconds. We have built a sigma laser at the Naval Postgraduate School to investigate its performance and to seek ways to reduce the jitter through cavity stabilization and improved modelocking. Measurement of picosecond pulse widths and femtosecond jitters is a nontrivial task. The report reviews opto-electronic measurement techniques that have been developed. Measurements on the NPS sigma laser are in the initial stages.

In Part II, we consider optical architectures that can be used to reduce the stringent requirements on the sampling source. The signal processing techniques can be divided into optical *oversampling* (relative to the Nyquist sampling rate) and optical *undersampling* methods.

- In optical oversampling methods the extra data that is recorded by the sampling method can be used to increase the bit resolution of the digitizer or, equivalently, to increase the signal-to-noise ratio of the sampled signal. In particular, a novel photonic sigma-delta digital convertor has been developed and studied. This implementation uses optical delay lines as accumulators to produce the digital output. Simulation results for these optical accumulators are included in this report, as is detailed information on the use of optical delay lines used as fiber lattice structures. This section also includes complete simulation results for a first-order optical sigma-delta convertor and preliminary simulation results for a second-order convertor.

- Undersampling the signal does not work if only a single channel is used. Undersampling in a set of parallel channels, however, allows the integration of the additional information into a wider bandwidth and more resolution than can be achieved by any single channel. Handling the parallel information using the Symmetrical Number System (SNS) is shown to be equivalent to the Discrete Fourier Transform technique for finding the spectral content of a signal. A parallel optical processing architecture is explored that implements a two-channel undersampling DFT receiver based on SNS processing.

Additionally Part II considers the amelioration of jitter effects through signal processing. Jitter manifests itself as nonuniform sampling of the signal; techniques have been developed in the signal processing literature to predict the effects of these nonuniformities. Simulations are shown to verify the prediction of performance using low frequency values that were easily computed.

Part I
Laser Sampling and Jitter Effects

1 Introduction

Analog-to-digital converters (ADCs) that can digitize a wide bandwidth portion of the rf spectrum (e.g., a 10 GHz band) with sufficient accuracy (e.g, 10 bits) have been a long-sought goal. Such ADCs typically begin with a sampling of the rf signal with narrow pulses at a sampling frequency, f_s. This sampling frequency must be greater than or equal to twice the highest frequency contained in the wave, f_m, i.e.,

$$f_s \geq 2f_m \,. \tag{1}$$

(The *Nyquist sampling frequency* f_N is obtained when the equality is used, $f_N = 2f_m$.) If our representative 10-GHz-wide signal is a baseband signal (i.e., its lowest frequency is close to zero), then its Nyquist sampling frequency is 20 GHz. (The Nyquist sampling *rate* is 20 gigasamples/s [GS/s].) After the sampling has been accomplished, processing digitizes the sample. In Part I of this report, we investigate the performance of optical pulse trains used as sampling waveforms and do not concern ourselves at this time with the digitization of the sample.

The performance requirement of an optical ADC has been studied by Taylor [1]. He derived expressions for both the maximum pulse width that the sampling pulse can have, as well as the maximum sample-time uncertainty (or "jitter") that the sampling waveform can have. His derivations are repeated in Appendix A of this report.

The sampling waveform will not be perfectly periodic. Each pulse that should arrive at time t_i will have a small timing error of δt. This δt is the *jitter* of the pulse train. This jitter will cause the sample to be taken at a slightly different time than desired. Sampling at the incorrect instant of time leads to an error in the measured voltage. Taylor [1] shows that the maximum jitter that can be tolerated without incurring a error greater than one-half of voltage level corresponding to one least-significant bit is given by

$$\delta t_{\max} \leq \frac{1}{2^{N+1}\pi f_m} = \frac{1}{2^N \pi f_N} \,, \tag{2}$$

where $\delta t_{\max}$ is the maximum jitter, N is the number of bits in the digitized output, f_m is the highest frequency in the signal, and f_N is the Nyquist sampling rate for the signal ($f_N = 2f_m$). For our representative 10-bit, 10-GHz-bandwidth ADC, the Nyquist rate would be 20 GS/s and the maximum allowable jitter is 15.5 fs. This jitter requirement is challenging to meet. Figure 1 shows curves for ADCs with 8-bit, 10-bit, 12-bit, and 14-bit resolutions as a function of the pulse sampling rate. In these curves, a Nyquist sampling rate was assumed (e.g., our 10-GHz wide signal would require a 20 GHz sampling frequency). We see from the figure that sampling rates higher than one GHz require sub-picosecond timing jitter.

Similarly, Taylor [1] considered the maximum pulse width (or interaction time) that the sampling pulse can have. During the sampling width, the measured voltage can be changing. Assuming that the sampling process computes the average of the voltage during the sampling pulse width rather than the instantaneous value at time t_i, Taylor found that the maximum sampling pulse width, ΔT, is

$$\Delta T \leq \frac{\sqrt{3}}{\pi f_m \sqrt{2^{N-1}}} \,. \tag{3}$$

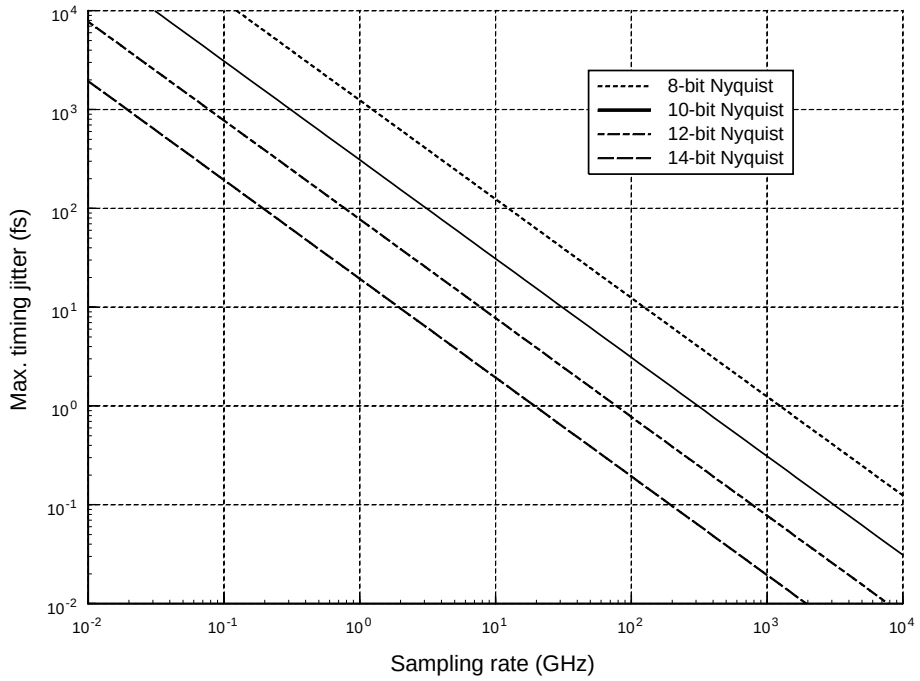

Figure 1: Maximum allowed laser jitter vs. pulse repetition frequency in ADCs for 8-, 10-, 12-, and 14-bit converters.

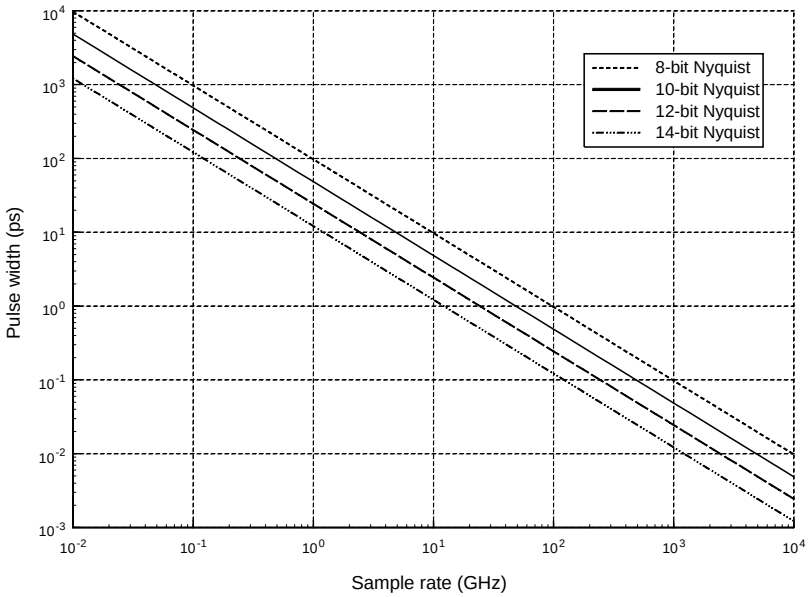

Figure 2: Maximum allowed ΔT (laser pulse width plus optical propagation time in modulator electrodes) vs. pulse repetition frequency for A-to-D converters for 8-, 10-, 12-, and 14-bit convertors.

Our representative 10-GHz, 10-bit ADC would require that $\Delta T_{\max} = 2.4$ ps. Modelocked lasers are available that produce outputs below this duration, so the pulse width is a lesser constraint than the jitter requirement.

Figure 2 shows a plot of the pulse width requirement vs. the sample rate for ADCs with 8-bit, 10-bit, 12-bit, and 14-bit resolution. We note that gigahertz sampling frequencies generally require pulse widths several picoseconds or less.

Modelocked laser technology offers the promise of being able to generate high-frequency pulse trains with small amounts of jitter. We now turn our attention to the technology of modelocked lasers.

2 Modelocking Techniques

Modelocking allows the user to obtain a train of ultrashort pulses from a laser. The concept is to lock the phases of many modes together to produce this pulse train.

- **Passive modelocking:** In passive modelocking the pulse train builds up from the noise (if the laser is self-starting) and the pulse amplitude and width adjust themselves to an equilibrium condition after a startup transient. The laser incorporates an element whose transmissivity (or phase response) is a nonlinear function of the light amplitude passing through it (e.g., a nonlinear optical mirror (NOLM) or a Kerr-effect polarization-rotating element). Both amplitude and phase modelocking can be accomplished. The pulse repetition rate of the pulse train

is determined by the mode spacing of the optical resonator; this implies that the resonator length is inversely proportional to the repetition frequency. One disadvantage of passive modelocking is that high repetition frequencies require an impractically small resonator length for fiber lasers (e.g., a 1 GHz repetition frequency requires approximately a 10-cm fiber resonator length). Hence, high pulse rate lasers use active mode-locking.

- **Active modelocking:** In active modelocking, an amplitude- or phase-modulating element is included within the resonator and the losses (or phase) are modulated at close to the desired repetition rate (which must be a fundamental or harmonic of the resonator frequency). The modulation may be sinusoidal and modest modulation depths will suffice (i.e., modulation depths of 1 are *not* required). Active modelocking, therefore, allows *harmonic modelocking* where there are an integer number of pulses within the resonator, rather than just one as in passive modelocking. This, in turn, allows operation at high repetition rates with resonators of adequate length to achieve the combination of desired properties of gain, dispersion, and pulse compression.

3 Laser Configurations

Several fiber laser configurations work as modelocked lasers. In addition, various diode and solid-state lasers have also been modelocked to produce short pulses with low jitters.

- Figure-eight laser: Figure 3 shows a conceptual diagram of a "figure-eight" laser [2]. This laser couples a fiber ring on the left side with a "nonlinear amplifying loop mirror" (NALM) [3] on the right side. The NALM consists of the 50:50 optical coupler and the erbium-doped fiber amplifier (pumped by an appropriate pump laser, here shown as a 980-nm diode laser). This combination has a nonlinear reflectivity whose reflection coefficient is a function of the incident optical power. The left loop is a conventional fiber with an isolator to make the optical flow unidirectional through the ring and an 80:20 coupler to extract a portion of the light.

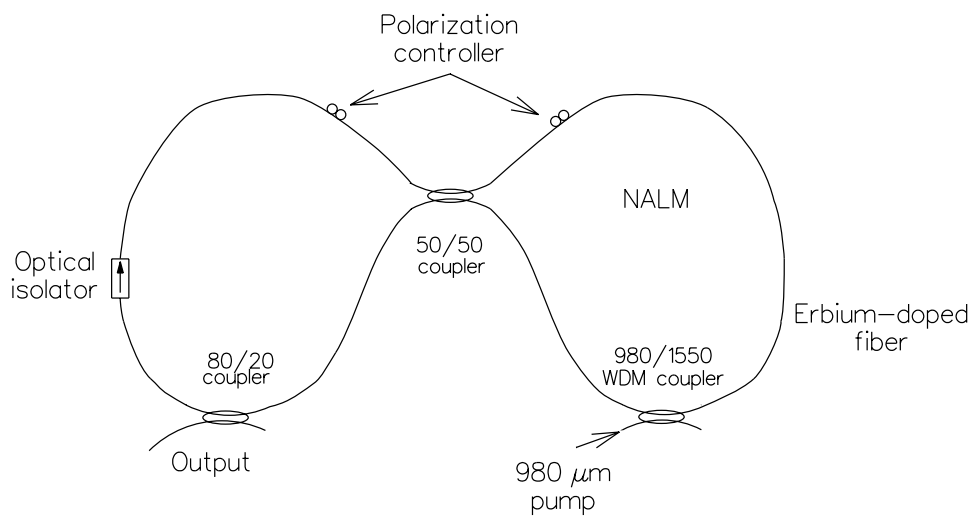

Figure 3: Conceptual layout of a figure-eight laser. (After [2].)

Figure 4 shows a variation of the figure-eight laser that is called a "sigma laser" (or "σ laser") [4–7]. This laser uses a double pass through the amplifying fiber to increase the light intensity. The polarization of the light is controlled and rotated 90° by the Faraday mirror at the end, so that the polarizations of each pass are orthogonal to each other (thereby removing the birefringence effects that would otherwise be present on an unpolarized beam).

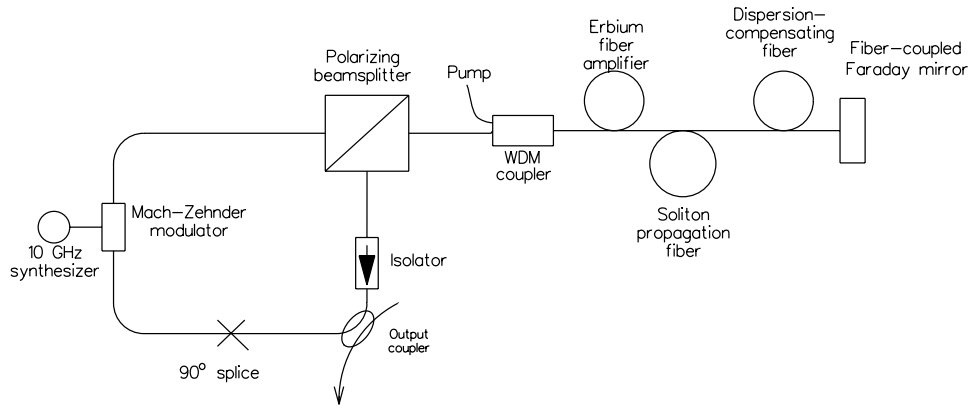

Figure 4: Conceptual layout of the NRL "sigma-laser" (or "σ-laser"). (After [8].)

- Ring laser: Figure 5(a)a illustrates a passively modelocked ring laser that incorporates a section of positive dispersion fiber (this fiber also provides the gain) and a negative dispersion fiber [9–11]. The modelocking is an additive-phase modelock. This laser configuration provides a pulse compression capability. Figure 5(b)b shows the pulses out of the ring laser. Since this laser is passively modelocked is unsuitable for generating the multi-gigahertz pulse train that we desire.

4 Pulse Shortening and Resonator Stabilization in Modelocked Lasers

4.1 Pulse Shortening

A key concept in the production of ultrashort pulses from modelocked lasers was the realization that a section of pulse-compression fiber could further shorten the output pulses from the laser. This pulse-compression fiber is usually a piece of dispersion compensating fiber with a negative dispersion (i.e., a dispersion with the opposite sign of that in the dispersion-shifted fiber and gain fiber). The required minimum amount of dispersion to achieve pulse compression is $D_{\mathrm{n,crit}} = 0.652$ where $D_n = \beta_2 L/D_g$. Here, β_2 is the chromatic dispersion coefficient per unit length, L is the fiber length, D_g is the *gain dispersion* (given by $D_g = g/\Omega_g^2$ with g being the saturated gain of the laser medium [typically $g = 0.1$] and Ω_g being the gain bandwidth) [12]. In the NRL sigma laser, $\beta_2 L \approx 0.5$ ps^2, and the gain dispersion, D_g, is approximately 0.004 ps^2. For these values, D_n ($= \beta_2 L/D_g$) is approximately 100, well in excess of the minimum required value.

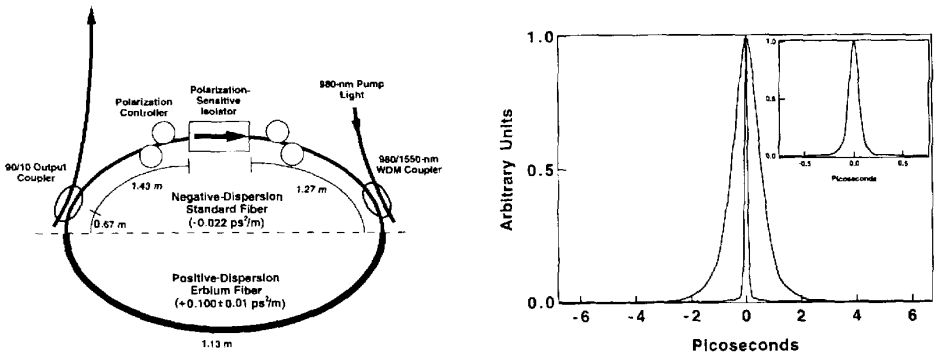

(a) Conceptual layout of a fiber ring laser incorporating pulse compression. (From [9].)

(b) Pulses out of ring laser utilizing pulse compression. The outer pulse is taken after erbium fiber segment and represents the maximum pulse width. The inner pulse is taken after 169 cm of negative-dispersion output coupling fiber and represents the minimum pulse width attained with this laser (77 fs). (From [9].)

Figure 5: Ring laser with both positive and negative pulse dispersion and output pulse autocorrelation measurements. (From Ref. [9].)

Without any pulse compression, the predicted pulse shape is Gaussian with a width, τ_a, of [12,13]

$$\tau_a = \sqrt[4]{\frac{D_g}{M_s}} \tag{4}$$

where M_s is the *modulator strength* (given by $M_s = M\omega_M^2/2$ with M being the modulation depth of the modelocking modulator and ω_M being the modulation frequency). The full-width, half-maximum (FWHM) pulse with is $\tau_{\mathrm{FWHM}} = 1.66\tau_a$.

With the addition of a pulse-compression fiber, the maximum possible reduction in pulse width, $R_{\max}$, is [12]

$$R_{\max} = 0.943 \sqrt[12]{\frac{(9\Phi_0/2)^2}{D_g M_s}} \tag{5}$$

where Φ_0 is the phase shift incurred by the pulse per round trip through the resonator (as given by $\Phi_0 = |D|/\tau^2$ with $|D|$ being the intracavity dispersion per round trip and τ being the pulse width). The typical value of Φ_0 is 0.1 [12] and τ is then found from $\tau = \sqrt{|D|/\Phi_0}$. Equation 5 reduces to

$$R_{\max} \approx 1.37 \sqrt[4]{\frac{D_f}{D_g}} = 1.37 \sqrt[4]{D_n}\,. \tag{6}$$

where D_f is the fiber dispersion ($D_f = \beta_2 L$). For the previous values of $D_f = 0.5$ ps^2 and $D_g = 0.004$ ps^2, we find $R_{\max} = 4.5$.

The minimum pulse width achieved is [12]

$$\tau_{\min} = \sqrt[6]{\frac{2D_g^2}{9\Phi_0 M_s}}\,. \tag{7}$$

The necessary required amount of normalized negative dispersion to achieve this minimum pulse width is [12]

$$D_n = \frac{2}{9}\sqrt[3]{\frac{(9\Phi_0/2)^2}{D_g M_s}}\,. \tag{8}$$

These equations allow us to predict the minimum pulse length that can be achieved and to calculate the required amount of negative dispersion required to achieve this minimum pulse width. Because of the 12th root dependence of the pulse shortening, the shortening depends primarily on the gain bandwidth Ω_g.

4.2 Resonator Stabilization

Changes in cavity length become changes in pulse position. [14] The resultant timing jitter, ∂t, is related to the change in cavity length, ∂l, by

$$\partial t = \frac{\partial l}{2\pi L f_m} \tag{9}$$

where L is the cavity length (or perimeter of a ring laser) and f_m is the modulation frequency. For example, to achieve a 2-ps jitter at a modulation frequency of 1 kHz for a ring laser of 3 m (corresponding to a 100 MHz repetition rate) requires that the optical path be controlled to within 0.2 μm, setting the standard of having a cavity control system with a bandwidth of several kilohertz and a submicron positional accuracy. Most of these control systems are based on a piezoelectric expander driven in an electronic feedback loop. The resonator stabilizer used in the NPS sigma laser is described in more detail in a later section.

5 Laser Performance Measurements

Typical measurements of the output pulse train include:

- temporal pulse characteristics (pulse repetition frequency [PRF] and pulse width)
- the RF spectrum of the pulse train (fundamental and harmonics, phase noise [jitter] and amplitude noise of source)
- optical spectrum of source (wavelength, spectral width, and symmetry of spectrum)

5.1 Pulse Repetition Frequency

The PRF of the laser pulse train is measured by applying the output of a fast photodetector to an electronic spectrum analyzer and measuring the center frequency of the lowest harmonic observed (i.e., the modelocker modulation frequency).

5.2 Autocorrelator Measurement of Pulse Width

Because of the limited speed of modern detectors, amplifiers, and oscilloscopes, it is not possible to measure directly the pulse width. Instead, the pulse width is measured with an autocorrelation measurement. As shown in Fig. 6, the optical pulse is split in to two pulses and the replicas are passed through a nonlinear crystal from opposite ends. In the region where the pulses overlap, second-harmonic generation occurs. The doubled-frequency light is detected with a sensitive, filtered photomultiplier tube and a trace is built up on a sampling oscilloscope as the delay is changed. Since the pulses are replicas of the input pulse, the trace records the autocorrelation of the pulse train. The width (FWHM) of the autocorrelation is recorded and the pulse width of the optical pulse is computed from this measurement, based on either a Gaussian-shaped pulse (little or no pulse compression) or a pulse shape that follows the square of the hyperbolic-secant (maximum pulse compression). The product of the measured width and the spectral linwidth (the *time-bandwidth product*) can be used to determine the pulse shape. A value of 0.44 or longer indicates a Gaussian pulse and a value of 0.32 indicates a sech^2 shape. Values between these extremes indicate a hybrid wave and that more pulse compression could be achieved. Appendix B contains more information about the autocorrelation measurement.

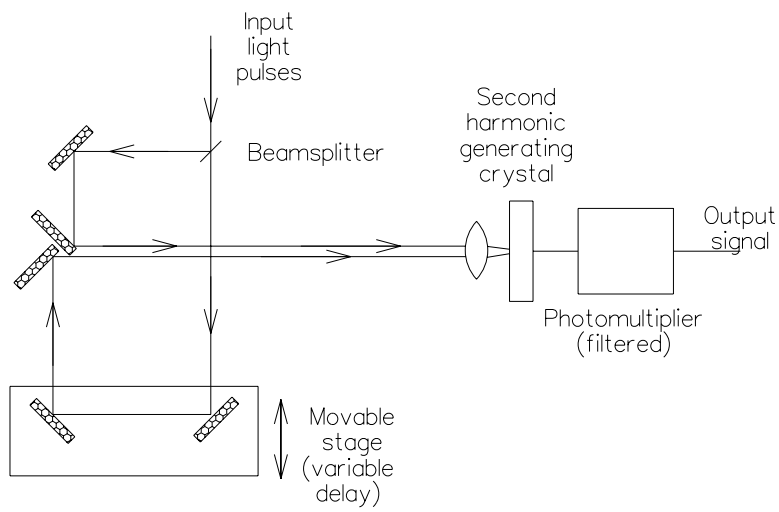

Figure 6: Optical autocorrelator for use in measuring pulse width of short optical pulses.

5.3 Laser Wavelength and Spectral Width

An optical spectrum analyzer is used to measure the laser wavelength and the spectral width of the optical source. It also shows whether unexpected wavelengths are lasing and indicates whether the source spectrum is symmetrical or not.

5.4 Jitter Measurement

The measurement of the laser jitter is difficult in the time domain. Since we are unable to resolve the pulse, it is not possible to resolve its position to the femtosecond accuracy that is required. Con-

sequently, jitter measurements are done by computations based on measurements in the frequency domain [15–18]. The pulse train from the laser is applied to a fast photodiode and the output is applied to an electronic spectrum analyzer. The current from the detector, $I(t)$ is [17]

$$I(t) = PT\left[1 + N(t)\right] \sum_{n=-\infty}^{\infty} \delta\left(t - nT - J(t)\right) , \tag{10}$$

where P is the average power in the pulse train, T is the (ideal) pulse period, $N(t)$ is the normalized laser pulse amplitude fluctuation, $\delta(t)$ is a Dirac delta function, and $J(t)$ is the random fluctuation in the pulse arrival time (or jitter). The spectrum analyzer displays the power spectral density, $S_p(\omega)$, integrated over the analyzer's resolution bandwidth. The power spectral density is the Fourier transform of the statistical autocorrelation function of $I(t)$ [17], or

$$S_p(\omega) = \mathcal{F}\left\{I(t) \star I(t)\right\} , \tag{11}$$

where $\mathcal{F}\left\{\cdot\right\}$ indicates the Fourier transform operation and $\star$ indicates the correlation operator. Using the identity that

$$\sum_{n=-\infty}^{\infty} \delta(t - nT - J(t)) = \frac{1}{T} \sum_{n=-\infty}^{\infty} \exp\left(jn\omega_L(1 - J(t))\right) \tag{12}$$

and expanding to the first order in $J(t)$, we find [17]

$$S_p(\omega) = P^2 \sum_{n=-\infty}^{\infty} 2\pi\delta(\omega - n\omega_L) + S_N(\omega - \omega_L) + n^2\omega_L^2 S_J(\omega - n\omega_L) . \tag{13}$$

Here $S_N(\omega)$ is the amplitude noise spectral density, S_J is the phase noise (jitter) spectral density, and ω_L is the (ideal) pulse repetition rate ($\omega_L = 2\pi/T$). Hence, we see that the spectrum will consist of a set of lines at the PRF of the pulse train, ω_1, and its harmonics. Each line will be accompanied by a series of amplitude noise sidebands, $S_N(n\omega_L)$ and phase noise (i.e., jitter) sidebands, $n^2\omega_1^2 S_J(n\omega_L)$ (where n is value of the harmonic of the PRF). At the fundamental frequency the amplitude noise spectrum will dominate the phase noise and $S_N(\omega)$ can be measured. Figure 7a shows a representative spectrum. The line consists of relatively narrow laser spectrum atop a wider pedestal due to the noise spectrum. At harmonics of the fundamental there are similar, weaker lines centered on the harmonic of the fundamental frequency. As shown in Figure 7b, the noise is a mixture of amplitude and phase noise (jitter). At a high enough harmonic, the phase noise will dominate the amplitude noise due to its multiplier of $n^2\omega_L^2$. (The test for dominant phase noise is to compare the noise profiles of two harmonics to ensure that the there is this $n^2\omega_L^2$ behavior.)

In a parallel approach, Rodwell *et al.* [16, 18] models the pulse train out of the laser as a set of noisy, jittery Gaussian shaped pulses (as would come out of a conventional modelocked laser without any pulse compression), given by

$$P(t) = PT\left[1 + N(t)\right] \sum_{n=-\infty}^{\infty} \frac{1}{\sqrt{2\pi}\sigma_J} \exp\left[\left(t - nT - J(t)\right)^2 / 2\sigma_J^2\right] . \tag{14}$$

The power spectral density, $S_p(\omega)$, of this pulse to the second order of $n\omega_L\sigma_J$ is

$$\begin{aligned} S_p(\omega) \approx P^2 e^{-\omega^2\sigma_J^2} \quad \textstyle\sum_{n=-\infty}^{\infty} \quad & \left[\left(1 - n^2\omega_L^2\sigma_J^2\right) 2\pi\delta(\omega - n\omega_L)\right. \\ & \left. + \left(1 - n^2\omega_L^2\sigma_j^2\right) S_N(\omega - n\omega_L) + n^2\omega_L^2 S_J(\omega)\right] . \end{aligned} \tag{15}$$

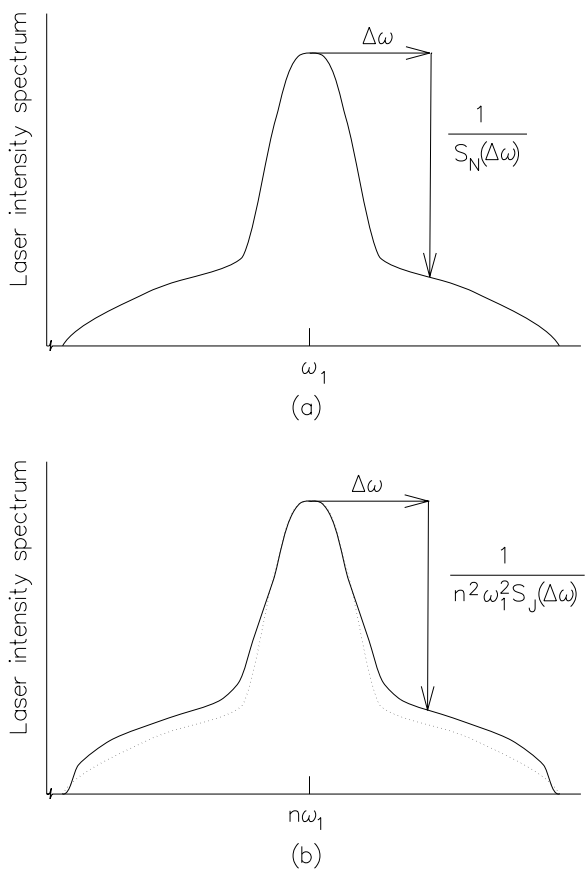

Figure 7: Conceptual spectrum of laser pulse train at (a) the PRF fundamental and (b) the n-th harmonic of the PRF frequency. In part (b) the dotted curve shows the amplitude noise effects without any jitter; the solid curve is the combined effects of amplitude and jitter noise. The jitter noise dominates.

Again, the spectrum is a series of lines at harmonics of ω_L plus a series of amplitude-noise sidebands, $S_N(\omega - n\omega_L)$ and phase-noise sidebands, $n^2\omega_L^2 S_J(\omega - n\omega_L)$. Once again, the low order harmonics are dominated by the amplitude noise sidebands and the higher order harmonics are dominated by the phase-noise sidebands due to their $n^2\omega_L$ weighting factor. Modelocked lasers with pulse compression technology to shorten the pulse produce soliton-shaped waves with a $\text{sech}^2(t)$ power dependence.

The measurement of laser stability is similar to the measurement of microwave stability and has borrowed techniques from that area. The measurement techniques for finding $S_N(\omega)$ and $S_J(\omega)$ are illustrated in the figure. The user sets up the spectrum analyzer to measure the spectrum with a dB vertical scale. For each offset frequency, the sideband is measured in so many dB below the peak value of the spectrum (the units are, thus, "dBc" or "dB relative to the carrier"). To be precise, the measurement bandwidth of the spectrum analyzer should be specified.

Once $S_J(\omega)$ is determined, the root-mean-squared (rms) value of the jitter (over the frequency range extending from ω_{low} to ω_{high} is computed from

$$\sigma_J \equiv \sqrt{< J^2(t) >} = \sqrt{\frac{1}{\pi}\int_{\omega_{\text{low}}}^{\omega_{\text{high}}} S_J(\omega) d\omega}\,. \tag{16}$$

The limit on the lower frequency is linked to the upper limit on the observations duration. [16]. The change in the laser timing over a duration, ΔT, is given by the weighted integral of the timing jitter spectral density,

$$< (J(t+\Delta T) - J(t))^2 >= \frac{2}{\pi}\int_0^\infty S_J(\omega)\,(1-\cos(\omega\,\Delta T))\;d\omega\,. \tag{17}$$

The $(1-\cos(\omega\,\Delta T))$ term in the integral varies as $(\omega\,\Delta T)^2$ for $\omega\,\Delta T \ll 1$ and, so, the jitter components for frequencies less than $\omega_{\text{low}} = 2\pi/2\Delta T$ contribute little to the changes in laser timing jitter over the observation duration, ΔT. Hence, we can use $\pi/2\Delta T$ as the value of ω_{low} in the jitter evaluation integral. For example, integrating from $f_{\text{low}} = 0.25$ Hz is appropriate for evaluating jitter that occurs during an experiment of 1 s duration.

The rms amplitude noise is similarly found as

$$\sigma_N \equiv \sqrt{< N^2(t) >} = \sqrt{\frac{1}{\pi}\int_{\omega_{\text{low}}}^{\omega_{\text{high}}} S_N(\omega)\,d\omega}\,. \tag{18}$$

An alternative notation is also used [17]. The peak power at the harmonic frequency can be called the *carrier power*, P_c. The jitter in the frequency range from f_{low} to f_{high} is

$$\sigma_J[f_{\text{low}}, f_{\text{high}}] = \frac{T}{2\pi n}\sqrt{\frac{P_{sb}}{P_c}}\,, \tag{19}$$

where

$$P_{sb} = 2\int_{nf_L+f_{\text{low}}}^{nf_L+f_{\text{high}}} \frac{P(f)}{B}\,df\,, \tag{20}$$

where B is the resolution bandwidth of the spectrum analyzer measurement, n is the harmonic number of the measured sideband, and f_L is the laser PRF.

Generally, the laser intensity noise is greater than the shot noise power in the detector. This *excess noise*, $S_N(\omega)$, can be stated in terms of dB above the shot noise power at a given photocurrent

(usually assumed to be 1 mA). At the photodetector, the ratio of the shot noise power, P_{shot}, to the carrier power is

$$\frac{P_{\text{shot}}}{P_c} = \frac{2qB}{I_0}, \tag{21}$$

where I_0 is the dc photocurrent from the detector and q is the value of the electron charge.

The National Institute of Standards and Technology has defined the *single-sideband phase noise spectral density* of the source, which is $L_n(\omega) = n^2\omega_1^2 S_J(\omega)$, so measurement of $S(\omega)$ from the n-th harmonic of the PRF allows calculation of $L_n(\omega)$. The parameter $L(f)$ $(= L\omega/2\pi)$ is the ratio of the power in one phase modulation sideband (in a 1 Hz bandwidth located at an offset of f Hertz from the center) to the total spectral power at the center. Following the terminology used in the microwave literature, the values of $L(\omega)$, $S_j(\omega)$ and $S_N(\omega)$ are given in dB. For example, $L(100\text{ Hz}) = L(200\pi \text{ radians/s}) = \times 10^{-10}$ s is the same as $L(100\text{ Hz}) = -100$ dBc(1 Hz), where "dBc" is "dB relative to the carrier" and the 1 Hz value in the parentheses indicates the measurement bandwidth. Frequently $L(f)$ is plotted instead of showing the laser's rf spectrum. Figure 8 shows a representative plot of $L(f)$ for two non-fiber lasers.

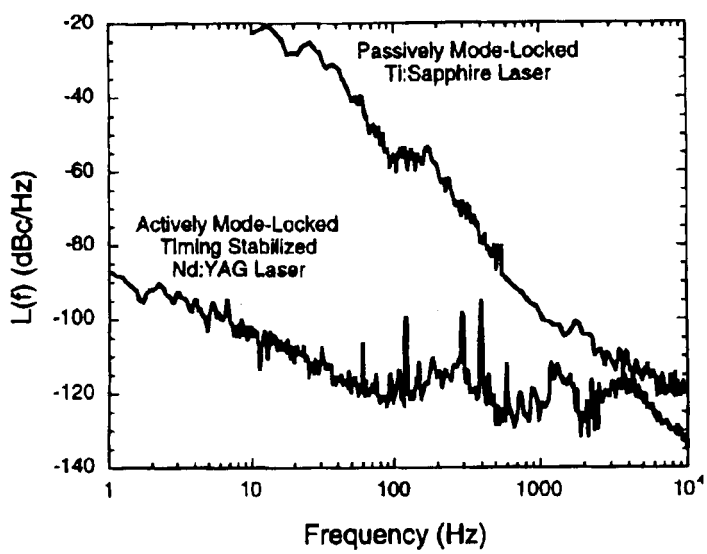

Figure 8: Representative plot of $L(f)$ from two modelocked lasers. The spectra are referenced from the fundamental frequency of the laser pulse train. From Ref. [19].

In cases where the harmonic value, n, is not large enough that the jitter noise totally dominates the amplitude noise, the spectrum of the jitter can be found by subtracting the single-sided power spectral density of the fundamental from that of the n-th harmonic [14],

$$L_J(f) = 10\log\left(\frac{10^{L_n(f)/10} - 10^{L_1(f)/10}}{n^2 - 1}.\right) \tag{22}$$

The rms timing jitter is then found from

$$\sigma_J = \frac{1}{2\pi f_L}\sqrt{2\int_{f_{\text{low}}}^{f_{\text{high}}} 10^{L_j(f)/10}\,df}\,. \tag{23}$$

5.5 Laser Jitter Measurement from Fundamental Spectrum

NRL has used a method that interrelates the measurement of the amplitude fluctuations of the pulse train to the temporal jitter. The amplitude "jitter" can be defined as

$$\sigma_A = \frac{\sqrt{|\delta A|^2}}{A} \tag{24}$$

where $\sqrt{|\delta A|^2}$ is the rms value of the amplitude fluctuations and A is the average amplitude. This jitter is found from [17]

$$\sigma_A = \sqrt{\frac{P_N}{P_C}} \tag{25}$$

where

$$P_N = 2\int_{nf_L+f_{\text{low}}}^{nf_L+f_{\text{high}}} \frac{P(f)}{B}\,df \tag{26}$$

is the power found in the noise "wings" of the fundamental spectrum and P_C is the power in the signal (at the center of the spectrum). The parameter B is the resolution bandwidth of the spectrum analyzer and the frequencies f_{low} and f_{high} are the cutoff frequency values described earlier. The timing jitter σ_J is related to the amplitude jitter by [17]

$$\sigma_J = \frac{T}{2\pi n}\sigma_A = \frac{T}{2\pi n}\sqrt{\frac{P_N}{P_C}} \tag{27}$$

where T is the period of the pulse train (without any jitter) and n is the harmonic where the jitter has been measured. (The timing jitter can also expressed as a fraction of the period by finding $\sigma_J/T = \sigma_A/2\pi n$.) NRL's measurement of their sigma laser found an amplitude jitter of 1.1% (or less) and a resultant timing jitter of 0.16 ps (or less).

6 Measurement Results

6.1 Measured Pulse Width Performance

Figure 9 on the following page shows some measured pulsewidth results from various modelocked lasers. We observe from the figure that there is no problem meeting the pulse width requirements of a sampling system to handle a 10-GHz bandwidth, 10-bit system. Pulse widths on the order of one picosecond to one-tenth of a picosecond are readily available. The pulse width requirement becomes challenging for a 10-bit system at sample rates of about 100 GHz or larger. Table 1 shows the measured pulse width of the several modelocked lasers that were plotted in Fig. 9 on the next page.

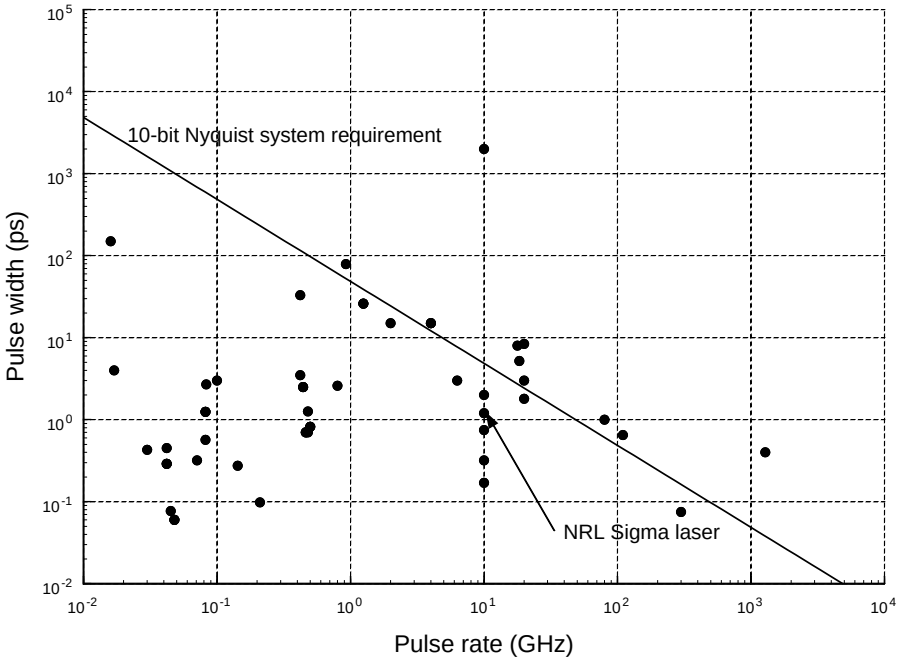

Figure 9: Experimentally measured laser pulse width vs. pulse repetition frequency in modelocked lasers. Also shown (solid line) is the theoretical curve for the maximum pulse width plus transit time of a 10-bit ADC system that is sampled at the Nyquist frequency rate of twice the value of the maximum frequency in the signal.

Table 1: Measured pulse width of modelocked lasers.

PRF (GHz)	Pulse width (fs)	λ (nm)	Ref.	PRF (GHz)	Pulse width (fs)	λ (nm)	Ref.
0.082	1250	1064	[16]	0.082	1250	1064	[16]
0.03	430	1064	[20]	0.42	3500	1560	[21]
0.48	1260	1500	[22]	0.048	60	1064	[23]
0.048	60	1064	[23]	0.016	150000	1550	[24]
10	320	1560	[25]	0.143	275	1563	[26]
300	75	1550	[27]	0.926	79000	1550	[27]
2	15000	1550	[28]	0.042	452	1550	[29]
0.0833	2700	1534	[30]	0.48	700	1500	[31]
0.071	320	1543	[32]	0.8	2600	1550	[33]
0.21	98	1570	[34]	0.1	3000	1550	[35]
20	3000	1550	[36]	0.045	77	1550	[9]
1.25	26000	1500	[37]	1.25	26000	1500	[37]
0.5	820	1500	[5]	0.5	820	1500	[5]
110	650	1500	[38]	17.8	8000		[39]
10	1200	1564	[40]	10	2000	1552	[41]
10	170	1550	[42]	0.42	33000	1300	[43]
20	8400	1540	[44]	0.082	570	1300	[45]
0.017	4000	1555	[46]	0.463	700	1550	[47]
0.463	700	1550	[47]	0.042	290	1550	[48]
0.042	290	1550	[48]	6.3	3000	1550	[49]
1280	400	1550	[50]	20	1800	1550	[51]
0.442	2500	1510	[52]	0.442	2500	1510	[52]
10	750	1550	[53]	10	2000000	1550	[54]
4	15000	1550	[55]	4	15000	1550	[55]
80	1000	1550	[56]	18.4	5200	1550	[7]

6.2 Measured Jitter Performance

Figure 10 shows the experimentally measured jitter for some operational modelocked lasers. Generally, few experimenters have measured the jitter of their lasers, so there are fewer data points than in the previous figure. We note that the jitter requirement for a 10-bit system is met only for pulse rates of approximately 1 GHz and lower. Higher sampling rates present a significant challenge to controlling the jitter in the pulse train, since jitters on the order of 10 femtoseconds or smaller are required. Table 2 shows the measured jitter of the modelocked lasers that were plotted in Fig. 10. (Few of the experiments have measured the jitter.)

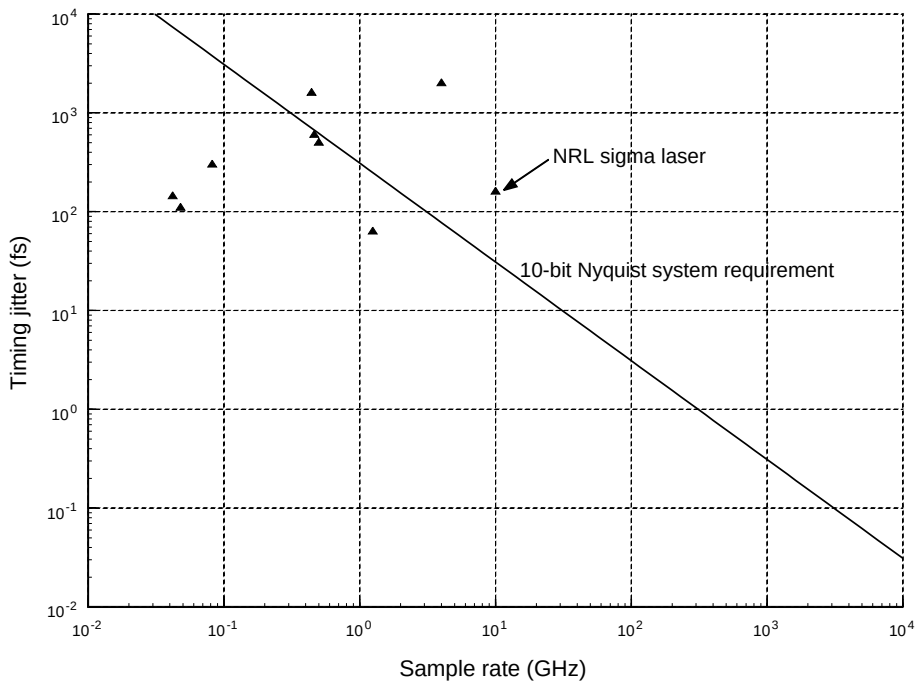

Figure 10: Experimentally measured laser jitter vs. pulse repetition frequency in modelocked lasers. Also shown (solid line) is the theoretical curve for the maximum jitter allowed for a 10-bit ADC system that is sampled at the Nyquist frequency rate of twice the value of the maximum frequency in the signal.

7 NPS Sigma Laser

Based on the performance achieved with the NRL sigma laser, we decided to build a version of this laser. With the aid of the NRL sigma laser team, a conceptual laser was designed as shown in Figure 11. The laser consists of two sections. The polarization-maintaining loop on the left is made of polarization-maintaining fiber components. The active modelocker (a Mach-Zehnder modulator) is in this loop, as is the output coupler. The circulation in the loop is unidirectional (clockwise)

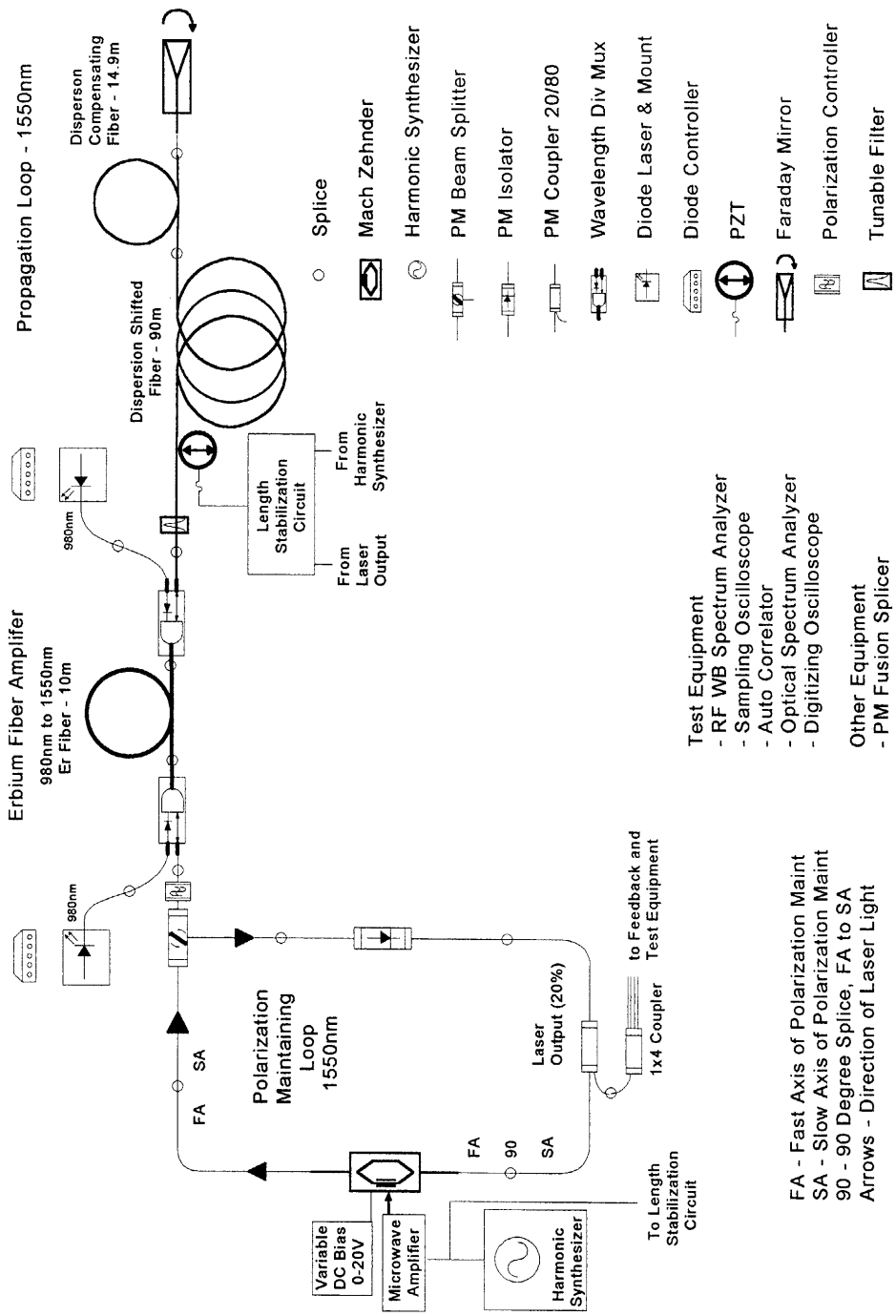

Figure 11: Design concept for NPS sigma laser.

Table 2: Measured jitter performance of modelocked lasers.

Year	PRF (MHz)	Pulse width (s)	λ (nm)	Jitter (fs)	Ref.
1989	82	1.25E-12	1064	3.00E+02	[16]
1991	48	6.00E-14	1064	1.10E+02	[23]
1993	1250	2.60E-11	1500	6.30E+01	[37]
1994	500	8.20E-13	1500	5.00E+02	[5]
1995	463	7.00E-13	1550	6.00E+02	[47]
1995	42	2.90E-13	1550	1.44E+02	[48]
1995	442	2.50E-12	1510	1.60E+03	[52]
1996	4000	1.50E-11	1550	2.00E+03	[55]

as determined by the isolator that is incorporated in the loop. One of the splices (just below the modulator) is a 90° splice that aligns the fast axis of the fiber on one side with the slow axis of the fiber on the other side; the other splices are 0° splices. A polarization-maintaining beamsplitter interconnects the polarization-maintaining loop with the gain section of the laser. The gain section of the laser consists of an erbium-doped fiber gain section (pumped with two 980-nm diode pump lasers), an isolation filter to remove the pump wavelengths, the length-stabilization element that reduces jitter (described later), a section of dispersion-shifted fiber to provide the required nonlinear interaction, a length of dispersion-compensating fiber to perform pulse compression, and a Faraday mirror to rotate the linear polarization of the reflected beam by 90° from the incident beam.

Components for the laser were selected from commercial vendors. The laser has been built and initial lasing has recently been achieved. Preliminary measurements of the laser's operating characteristics are currently being performed.

7.1 Resonator Stabilization

As described earlier, the primary cause of jitter is fluctuations in the length of the laser resonator due to environmental effects. Electronic feedback techniques have been developed to cancel these fluctuations [14, 16, 18]. As shown in Figure 12, the laser output is detected with a fast photodiode; the resulting voltage is amplitude limited, and applied to a double-balanced mixer acting as a phase detector. The phase of the laser signal is compared with a high-stability electronic reference and an error signal is generated. Integration of the error signal converts the phase-error to a frequency-error signal that is amplified and applied to a piezoelectric ring. This ring has about 60 meters of the dispersion-shifted fiber wrapped around it. As the ring expands and contracts in response to the error signal, the optical resonator length changes, causing a corresponding frequency shift in the laser output. The expansion and contraction of the ring will cancel any contraction or expansion of the resonator, thereby keeping the laser PRF constant.

8 Summary of Laser Sampling Performance Measures

In this part of the report, we have presented information about the use of modelocked laser to provide the sampling source for optical sampling of high frequency signals. We have shown that these lasers are capable of achieving the pulse width requirements for a sampling system and are close to achieving the jitter requirements. These lasers incorporate an active mode locker with

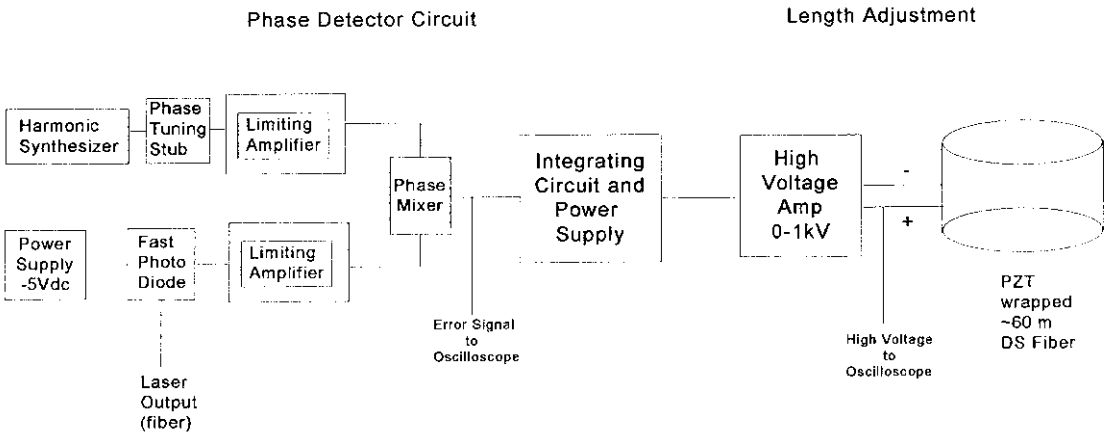

Figure 12: Resonator stability circuit for NPS sigma laser.

devices that induce a soliton-like wave within the laser. With the addition of pulse-compression devices, the pulse width is narrowed to the picosecond and subpicosecond regime. The jitter of the wave is controlled through the incorporation of resonator stabilization circuitry to control the laser resonator length to counter the environmental effects. The combination of low jitter and high pulsing frequency has best been achieved by the sigma laser designed at NRL for high data-rate optical communications. With the aid of the NRL team, we have designed and built a sigma laser in order to measure its performance and to serve as a testbed to explore techniques for lowering the measured jitter. We have also identified and described techniques for measuring the optical performance of these short-pulse, low-jitter pulse trains.

Part II
Optical Signal Processing

9 Design of Optical Oversampling Architectures

9.1 Introduction

9.1.1 Advantages of Oversampling Microwave Signals

Optical sampling of a microwave signal at the Nyquist rate (sampling rate equal to twice the bandwidth of interest) has the advantage of a low sampling rate. Disadvantages, however, include the need for high-accuracy analog anti-aliasing circuits to filter the signal before sampling. The filter circuits serve to attenuate the high frequency noise and out-of-band components that alias into the signal (anti-aliasing filter). These anti-aliasing filters are vulnerable to noise and interference which corrupt the signal-of-interest (SOI). Also, fine-line VLSI technology is better suited to fast digital architectures rather than precise analog architectures making the filter fabrication process difficult.

When a signal is oversampled (sampling rate greater than twice the bandwidth of interest), the resolvable bandwidth is traded off for a higher precision representation of the signal in the digital domain. Oversampling is attractive for many systems in that the analog anti-alias filtering requirements are relaxed. Oversampling architectures are especially tolerant of circuit non-idealities and component mismatch and as such do not require high precision circuits. Also, with the low operating voltage requirements of the post-detection digital processors (e.g., 3 V), analyzing the signal in discrete quantization levels is becoming more difficult, making oversampling an attractive alternative. Specifically, an oversampling architecture (or "sigma-delta" modulator [or $\Sigma\Delta$M], as it is commonly referred to) consists of an analog filter in a feedback loop. Together with the filter, the feedback loop acts to attenuate the quantization noise at low frequencies while amplifying the high frequency noise. Since the signal is sampled at many times the Nyquist rate, a digital filter can be used to remove the high-frequency quantization/modulation noise without affecting the signal band. The concepts of oversampling have grown from pulse code modulation theory and an excellent history of this development is given in Ref. [57].

9.1.2 Integrated Optical Processing

Integrated optical components offer a number of advantages over their electronic counterparts. These advantages include large bandwidth, use of optical sources for high-speed sampling, low power consumption, improved reliability, and insensitivity to vibration and electromagnetic interference. Since all-electronic $\Sigma\Delta$ modulators require oversampling, their applicability is mainly limited to low and moderate signal frequencies. The use of optical integrated components in conjunction with high-speed laser pulse sampling methods provide an attractive solution to the otherwise bandlimited all-electronic $\Sigma\Delta$ architecture.

In Part II, Section 9.2 of this report, the advantages of oversampling are reviewed and the performance of both first-order and second-order $\Sigma\Delta$Ms are presented. Two important optical oversampling schemes are then presented in Section 9.3. The first is based on using integrated optical Mach-Zehnder interferometers, fiber lattice structures and mode-locked laser sampling methods. The second approach described uses free-space bulk optic components and employs multiple quantum well and self electro-optic components. Both of these approaches have shown good promise of extending the $\Sigma\Delta$ modulation into the very high frequency (VHF) region and beyond.

9.2 ΣΔM Design

9.2.1 Signal-to-Noise Relationships

To understand the consequences of oversampling, we start with the development in [57] and address the basic properties of quantization. Figure 13 shows an example of a uniform multi-level quantization characteristic and a two-level quantization of an input signal x. The quantized signal

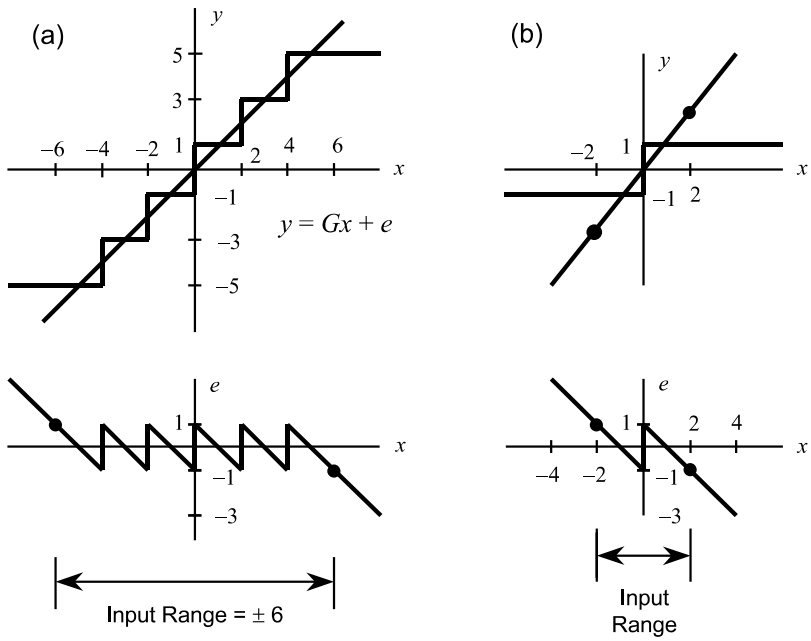

Figure 13: a) An example of a uniform multilevel quantization characteristic that is represented by linear gain G and error e, b) For two-level quantization the gain is arbitrary. (Adapted from [57]).

is $y = Gx + e$, where G is the gain, x is the input signal, and e is the quantization error. In the two-level quantizer the gain G is arbitrary. If the quantization error has equal probability of lying anywhere in the range $\pm q_s/2$, the mean square quantization noise power is

$$e_{qns}^2 = \frac{1}{q_s}\int_{-q_s/2}^{q_s/2} e^2\, de = \frac{q_s^2}{12}\,. \tag{28}$$

If a one-sided representation of frequencies is employed where all power lies $0 \le f < \infty$, and the quantized signal is sampled at $f_s = 1/T$, all the quantization noise folds into $0 < f < f_s/2$. The spectral density of the sampled noise is then

$$e_{qns}(f) = e_{qns}\left(\frac{2}{f_s}\right)^{1/2} = e_{qns}\sqrt{2T} \tag{29}$$

and quantization noise power density is

$$e_{qns}^2(f) = \frac{2e_{qns}^2}{f_s}\,. \tag{30}$$

If an oversampling ratio (OSR) is defined as

$$OSR = \frac{f_s}{2f_0} = \frac{1}{2f_0T} = \frac{\text{Sampling Frequency}}{\text{Nyquist Rate}} \tag{31}$$

where f_0 is the highest frequency component of interest ($0 \leq f < f_0$), the noise power falling into the signal band

$$n_0^2 = \int_0^{f_0} e^2(f)\,df = e_{qns}^2 \left(\frac{2f_0}{f_s}\right) = \frac{e_{qns}^2}{OSR}\,. \tag{32}$$

Therefore, oversampling reduces the in-band rms quantization noise voltage n_0 by the square root of the oversampling ratio. That is, each doubling of the sampling frequency decreases the in-band noise by 3 dB (increasing the resolution by 1/2 LSB).

Figure 14 on the next page shows the spectrum for e_{qns}^2 (flat) and illustrates what happens to the inband quantization noise power when the signal is oversampled. Figure 14a shows the normalized inband quantization noise power for $0 < f < f_s/2$ ($e_{qns}^2 = 1$) where the signal is sampled at the Nyquist rate. In Fig. 14b the signal is oversampled by a factor of 4 reducing the inband quantization noise power to $e_{qns}^2 = 1/4$. [1] Putting the oversampled signal through a LPF with a 3 dB bandwidth of $f_s/2$, the quantization noise density within the signal band is reduced by a factor of 4.

The signal-to-noise ratio (SNR) for an n-bit system with bandwidth f_{sig} can be expressed as [58]

$$SNR = 2^{n-1}\sqrt{3}\,\sqrt{\frac{f_s}{f_{sig}}} \tag{33}$$

where f_s is the sampling frequency. In dB, we have

$$SNR = 6.02n - 1.25 + 10\log\left(\frac{f_s}{f_{sig}}\right)\ \text{dB}\,. \tag{34}$$

If, for example, a four-times oversampled system is considered, then $f_s/f_{sig} = 8$ and

$$SNR = (n+1)6.02 + 1.76\ \text{dB}\,. \tag{35}$$

That is, the SNR increases by 6 dB or 1-bit as expected.

9.2.2 First-order ΣΔ Modulator

The efficiency of the oversampling operation can be increased by including an analog noise shaping filter $H(s)$ in a single feedback loop. A block diagram of a general first-order ΣΔ configuration is shown in Figure 15 on page 27. The output of the analog noise shaping filter $H(s)$ is quantized by an analog-to-digital (A/D) converter with $n \geq 1$ bits. The quantized output from the A/D is fed back to a n-bit digital-to-analog (D/A) converter to be subtracted off from the input signal. This feedback loop forces the average value of the quantized signal y_i to track the input signal.

The response of a first-order ΣΔ that uses a multi-level A/D is shown in Fig. 16 on page 27 [57]. Also shown is the input signal ramp. The square waves, with their various duty cycles (limit cycles) are representative of the quantized output. Note that the width of the top and bottom portions of the square wave (duty cycle) indicate where the input signal lies. For example, when the input lies at the center of the limit cycles, the width of the square wave at the top and bottom are equal (50% duty cycle).

[1] Note the sampling operation introduces replicas of the frequency spectra at multiples of the sampling frequency.

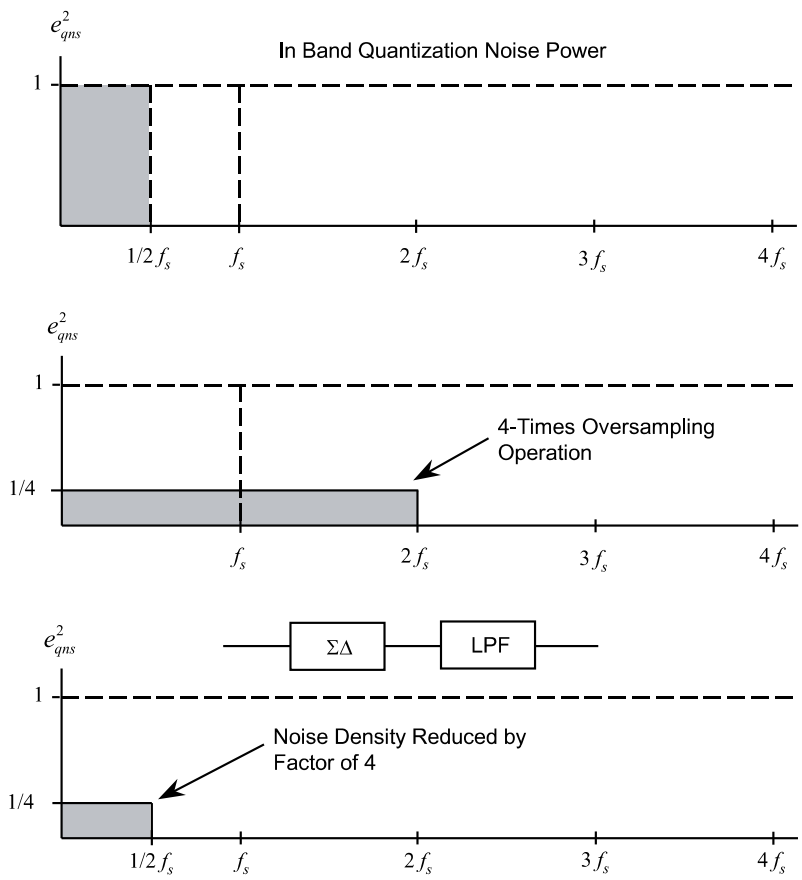

Figure 14: In-band quantization noise power density with a) Nyquist sampling, b) oversampling factor of 4, and c) output of a LPF with 3 dB bandwidth of $f_s/2$.

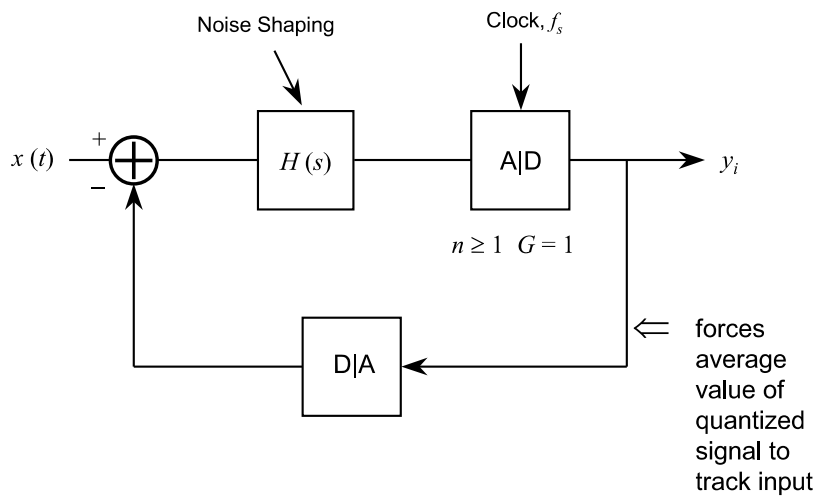

Figure 15: Block diagram of a general first-order ΣM configuration.

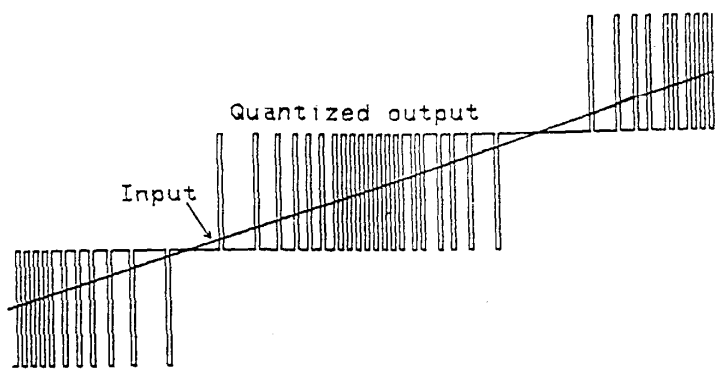

Figure 16: Response of a first-order multilevel ΣΔ [57].

The first-order $\Sigma\Delta$ configuration in Fig. 15 is difficult to analyze due to the nonlinear A/D component. With a *sampled data noise model*, the A/D component is removed and is replaced by the addition of the corresponding quantization error. The noise shaping filter is also replaced by the sampled data equivalent $H(z)$. The corresponding first-order sampled data noise model is shown in Fig. 17. The signal transfer function (x_i to y_i) is [59]

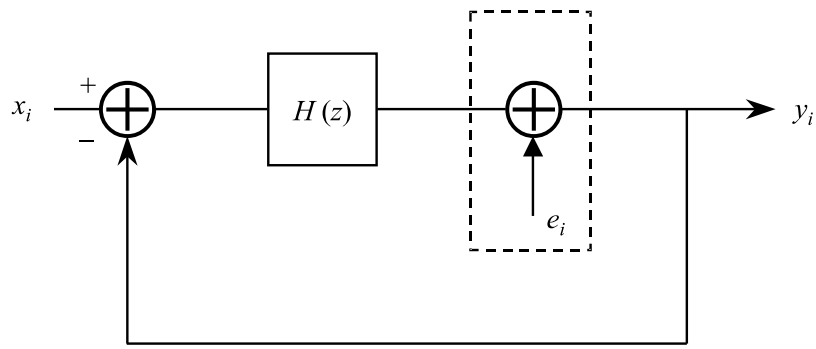

Figure 17: First-order sampled data noise model.

$$STF = \frac{H(z)}{1 + H(z)} \,. \tag{36}$$

The STF is designed to have a flat response in the signal band. The noise transfer function (e_i, to y_i) is

$$NTF = \frac{1}{1 + H(z)} \,. \tag{37}$$

The NTF is designed to have a high attenuation in the signal band. The Z transform of the quantized output signal is then

$$Y(z) = \left(\frac{H(z)}{1 + H(z)}\right) X(z) + \left(\frac{1}{1 + H(z)}\right) E(z) \tag{38}$$

or

$$Y(z) = STF(z)X(z) + NTF(z)E(z) \,. \tag{39}$$

The power spectrum of the white quantization noise e_i is [59]

$$X_{nn}(f) = R_{nn}\,(z)|_{z=e^{j2\pi f_0/f_s}} \tag{40}$$

where $R_{nn}(z)$ is the z-transform $\mathcal{Z}\left\{r_{ee}(k)\right\}$ where $r_{ee}(k)$ is the autocorrelation of the noise e_i. From linear systems theory

$$R_{nn}(z) = e_{qns}^2 NTF(z)NTF(z^{-1}) \,. \tag{41}$$

As an example, a first-order sampled data $\Sigma\Delta$ modulator using a single delay accumulator for $H(z)$ is shown in Fig. 18 on the facing page. The accumulator output is

$$w_i = x_{i-1} - e_{i-1} \tag{42}$$

and the quantized signal is then

$$y_i = x_{i-1} + (e_i - e_{i-1}) \,. \tag{43}$$

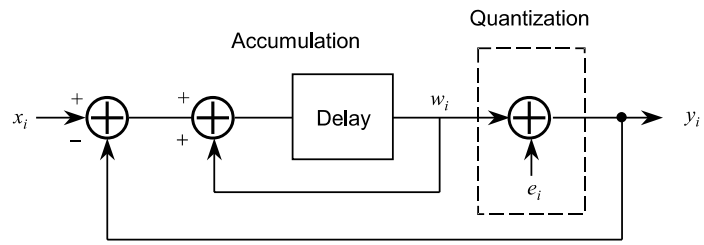

Figure 18: Sampled data first-order $\Delta\Sigma$ modulator using a single delay accumulator.

Note that this architecture differentiates the quantization error (modulation noise) while the input signal x_{i-1} is unchanged. The signal and noise transfer functions for the first-order $\Sigma\Delta$ shown in Fig. 18 are

$$STF(z) = z^{-1} \tag{44}$$

and

$$NTF(z) = (1 - z^{-1})\,. \tag{45}$$

The power spectrum of the output quantization noise is then

$$X_{nn}(f) = e_{qns}^2\,(1 - z^{-1})(1 - z)\big|_{z=e^{j2\pi f/f_s}} \tag{46}$$

or

$$X_{nn}(f) = 4e_{qns}^2 \sin^2\left(\frac{\pi f}{f_s}\right)\,. \tag{47}$$

The quantization noise power in the signal band ($-f_0$ to f_0) can then be calculated as

$$n_0^2 = \frac{2}{f_s}\int_0^{f_0} X_{nn}(f)\,df\,. \tag{48}$$

Substituting (46) gives

$$n_0^2 = \frac{2}{f_s}\int_0^{f_0} 4e_{qns}^2 \sin^2\left(\frac{\pi f}{f_s}\right)\,df \tag{49}$$

or

$$n_0^2 = \frac{8}{3}\pi^2 e_{qns}^2\left(\frac{f_0}{f_s}\right)^3 = \frac{\pi^2}{3}e_{qns}^2\left(\frac{2f_0}{f_s}\right)^3\,. \tag{50}$$

In terms of the oversampling ratio

$$n_0^2 = \frac{\pi^2}{3}e_{qns}^2(OSR)^{-3}\,. \tag{51}$$

The RMS value of noise voltage in the signal band is

$$n_0 = e_{qns}\frac{\pi}{\sqrt{3}}(2f_0T)^{3/2} \tag{52}$$

or

$$n_0 = e_{qns}\frac{\pi}{\sqrt{3}}(OSR)^{-3/2}\,. \tag{53}$$

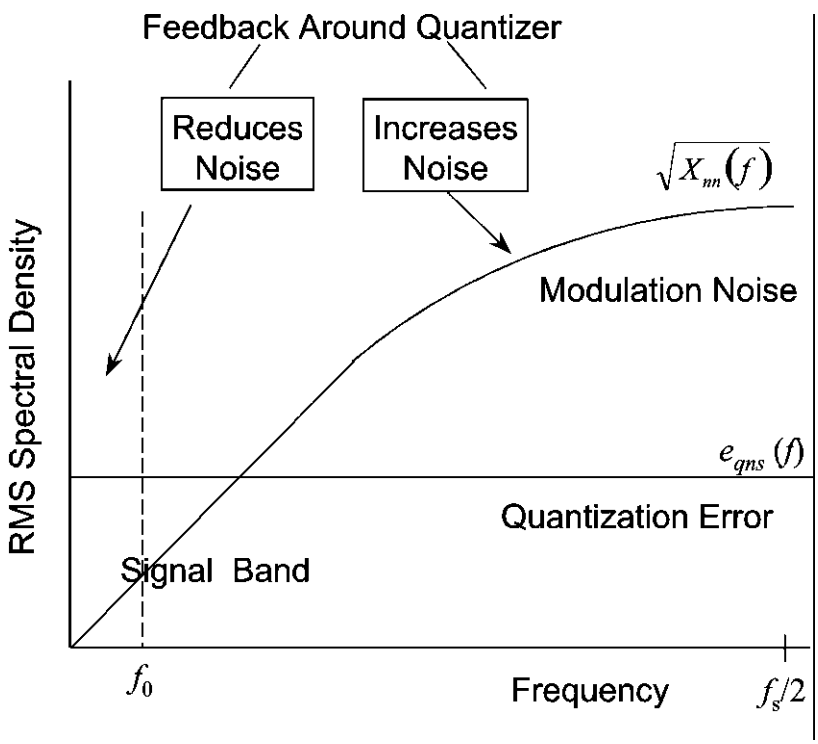

Figure 19: RMS spectral density. (Adapted from Ref. [57]).

This result indicates that each doubling of the OSR reduces the noise by 9 dB (+1.5 bits extra resolution). The RMS spectral density shown in Fig. 19 on the facing page shows the behavior of the STF and the NTF filter functions. Note the quantization error remains flat up to $f_s/2$.

Figure 20 on the next page shows a first-order single-bit ΣM. A block diagram is shown in Fig. 20a. In this configuration, the A/D is replaced by a single comparator with matching threshold voltage V_T. A quantizer with only two levels $\pm q_s/2$ is employed so as to avoid the harmonic distortion generated by step-size mismatch in multi-bit quantizers [60]. Figure 20b shows the comparator output and the sampled input. Figure 20c shows the output of the accumulator stage [61] output,

9.2.3 Second Order ΔΣ Modulator

The block diagram of a second-order sampled data ΣΔM is shown in Fig. 21. In this configuration two accumulators are used. The second accumulator (before the quantizer) must have the delay in the feedforward path for stability. The output of this architecture is

$$y_i = x_{i-1} + (e_i - 2e_{i-1} + e_{i-2}) \tag{54}$$

and the noise transfer function is

$$NTF = \left(1 - z^{-1}\right)^2 . \tag{55}$$

The power spectrum of the output quantization noise is

$$X_{nn}(f) = e_{qns}^2 \left(1 - e^{-j\omega T}\right)^2 \left(1 - e^{j\omega T}\right)^2 \tag{56}$$

or

$$X_{nn}(f) = 16 e_{qns}^2 \sin^4\left(\frac{\pi f}{f_s}\right) . \tag{57}$$

The in-band quantization noise power $(-f_0, f_0)$ is then

$$n_0^2 = \frac{2}{f_s}\int_0^{f_0} X_{nn}(f)\, df = 6 \cdot 4\pi^4 e_{qns}^2 \left(\frac{f_0}{f_s}\right)^5 . \tag{58}$$

The RMS value of noise voltage in the signal band is

$$n_0 = e_{qns}\frac{\pi^2}{\sqrt{5}}(2f_0T)^{5/2} \tag{59}$$

or

$$n_0 = e_{qns}\frac{\pi^2}{\sqrt{5}}(OSR)^{-5/2} . \tag{60}$$

That is, the noise falls 15 dB for every doubling of the sampling frequency (+2.5 extra bits).

In Fig. 22a a single bit second order architecture is shown and in Fig. 22b the comparator output for this system are shown along with the input signal [61]. The accumulator outputs are shown in Fig. 22c. Note how the limit cycles are much better behaved compared to the first-order system.

9.2.4 L Stable Loops

In general, for L stable loops

$$n_0 = e_{qns}\frac{\pi^L}{\sqrt{2L+1}}(2f_0T)^{L+1/2} \tag{61}$$

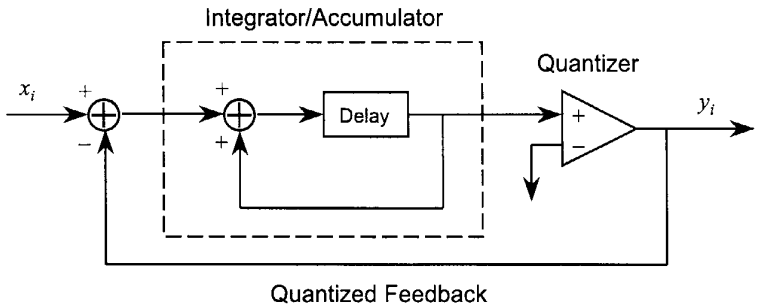

(a)

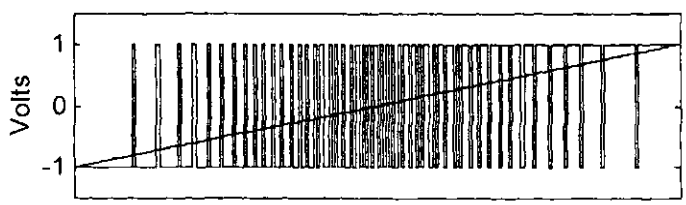

(b)

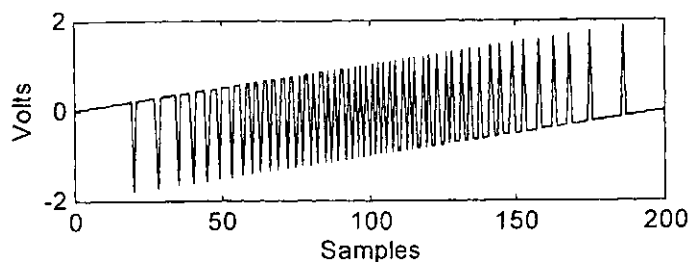

(c)

Figure 20: First-order single-bit $\Sigma\Delta$ showing (a) block diagram, (b) comparator output, and (c) accumulator output.

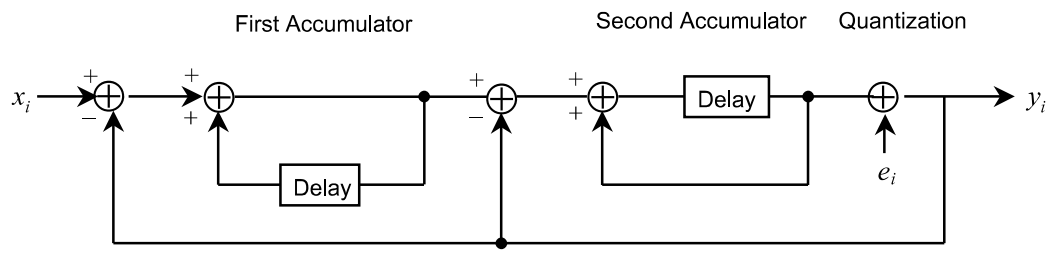

Figure 21: Block diagram of a second-order all-electronic ΣΔM.

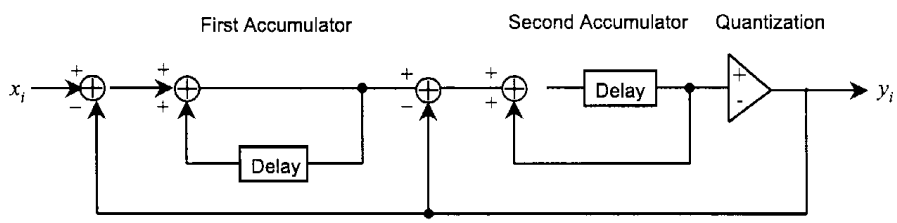

(a)

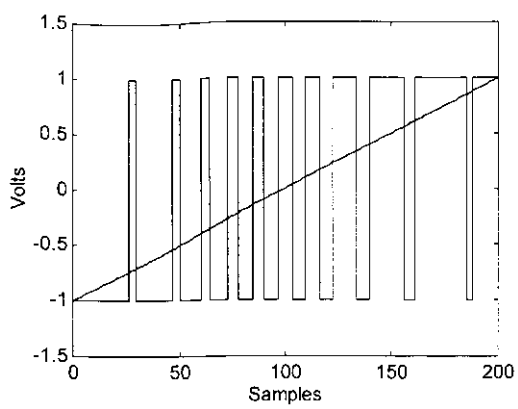

(b)

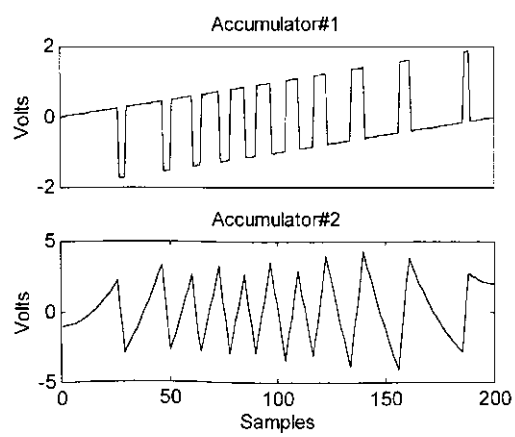

(c)

Figure 22: Second-order single-bit ΣΔ showing (a) block diagram, (b) comparator output, and (c) accumulator output.

Table 3: ΣΔ Resolution Summary for OSR = 2.

OSR = 2	**SNR Increased By:**	**Added Resolution**
Oversampling	3 dB	0.5 LSB
First-order	9 dB	1.5 LSB
Second-order	15 dB	2.5 LSB
L-order	$3(2L+1)$	L + 0.5 LSB

and the noise falls $3(2L+1)$ dB for every doubling of the sampling rate ($L+1/2$ extra bits) [57]. The circuits for these higher-order modulators, however, are difficult to stabilize.

A summary of these results is shown in Table 3. In Fig. 23, the RMS noise as a function of the oversampling ratio for $L = 0, 1, 2$ and 3 is shown. Note that when $1 < OSR < 2$, the SNR for the $L = 0$ case is better.

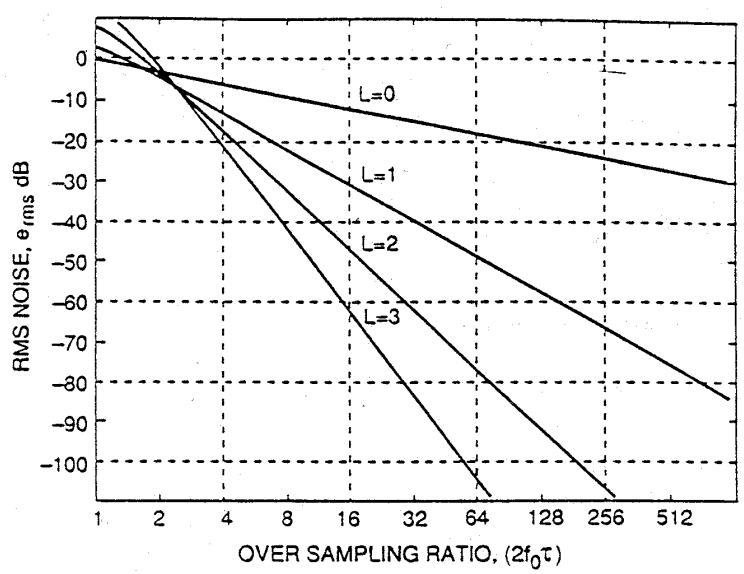

Figure 23: RMS noise that enters the signal band [57].

Before introducing the integrated optical ΣΔ modulator designs, a more general block diagram of a second-order single-bit ΣΔ is shown in Fig. 24 on the facing page. Here the accumulators H_1 and H_2 contain gain variables A and C and leakage variables B and D. Small deviations (from unity) in the gain variables A and B have little effect on the overall performance of the ΣΔMs. The DC gain of the second accumulator is $H_2(0) = 1/1-D$. If the DC gain of the accumulator is at least equal to the OSR the increase in the baseband noise is less than 0.3 dB [57]. The corresponding

transfer functions are

$$H_1(z) = \frac{A}{1 - Bz^{-1}} \qquad H_2(z) = \frac{Cz^{-1}}{1 - Dz^{-1}} \tag{62}$$

This general form will be useful when discussing the optical ΣΔM designs in the next section.

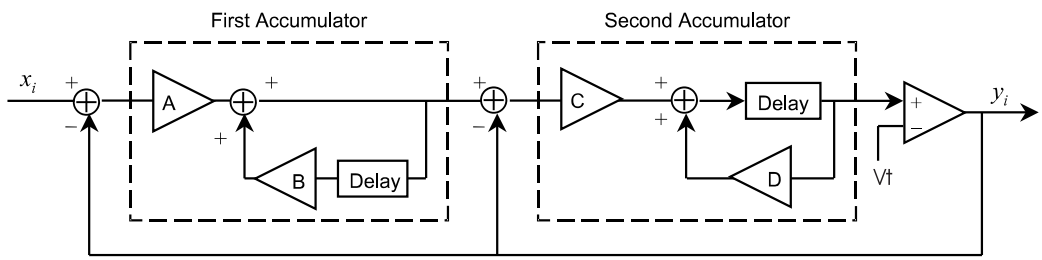

Figure 24: Block diagram of a second-order ΣΔ modulator with variable gain accumulators.

9.3 Integrated Optical ΣΔM Design

9.3.1 First-Order Integrated Optical ΣΔM

A block diagram of a first-order integrated optical ΣΔ modulator is shown in Fig. 25(a). In the integrated optical design, laser pulses from a high-speed mode-locked laser (See Part I) are used to oversample the rf signal. To gain a better understanding of the design, the integrated optical components are described below and their functionality within the modulator is detailed.

Mach-Zehnder Interferometer

The Mach-Zehnder interferometers (MZIs) are used to efficiently couple the wideband rf signal into the optical domain. They also serves to subtract the electrical feedback signal from the input antenna signal. Figure 26 on the next page shows a schematic diagram of an MZI. The input pulse is split into equal components, each of which propagates over one arm of the interferometer. If the optical paths of the two arms are equal and if no phase shift is introduced between the interferometer arms, the two components combine in phase at the output and continue to propagate undiminished. For the current design, a three-electrode configuration is used to achieve a push-pull phase change. The push-pull effect increases the phase change efficiency of the device [62]. This configuration is utilized to subtract the comparator feedback signal from the applied rf input voltage. To take advantage of this push-pull configuration, the feedback voltage polarity from the comparator must be reversed. The transfer function of the MZI can be expressed as [62]

$$I_{\text{out}} = I_{\text{in}} \left\{ \frac{1}{2} + \frac{1}{2} \cos\left[\Delta\phi(\nu) + \theta\right] \right\} \tag{63}$$

where I_{in} and I_{out} are the input and output light intensity, respectively, and

$$\Delta\phi(\nu) = \frac{2\pi n_e^2 r \Gamma L_i \nu}{G\lambda} \tag{64}$$

is the voltage-dependent phase shift and is a function of the effective index of the optical guide n_e, the pertinent electro-optic coefficient r, the inter electrode gap G, the electrical-optical overlap

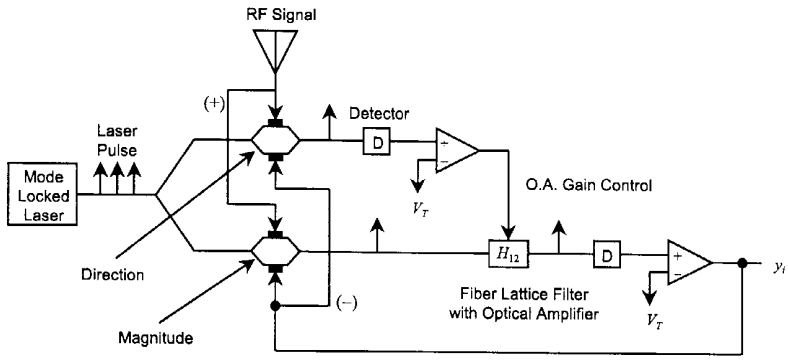

(a)

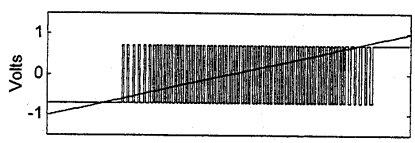

(b)

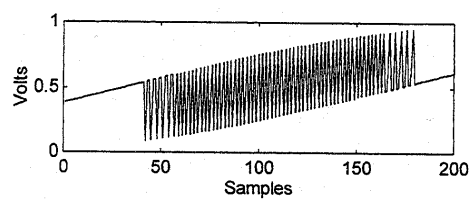

(c)

Figure 25: First-order integrated optical ΣΔM, (a) Block diagram,(b) the comparator output, and (c) the comparator input using ideal H_{12}.

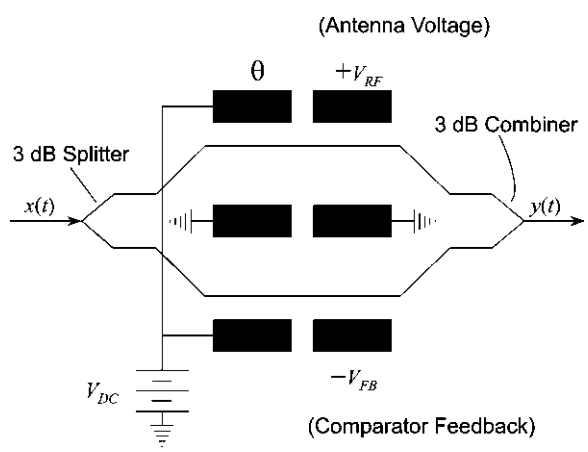

Figure 26: Schematic diagram of a MZI in a push-pull configuration.

parameter Γ, and the free-space optical wavelength λ. The modulation voltage, $\nu = V_{\rm rf} - V_{\rm FB}$, serves to subtract the feedback voltage V_{FB} from the antenna rf voltage V_{rf}.

In the first-order $\Sigma\Delta$M, two interferometers are used to couple the rf signal. One interferometer provides the *magnitude* to be accumulated. The other interferometer is used to determine the *direction* of accumulation (accumulate up or accumulate down). Figure 27 plots the transfer functions for both interferometers. Both MZIs map the input signal to a normalized output intensity between 0 and 1 (light intensity cannot be negative). The transfer functions are the same except for the dc bias voltage resulting in the phase shift θ. For the MZI generating the magnitude of the signal, $\theta = \pi$. For the MZI controlling the direction of accumulation, $\theta = -\pi/2$.

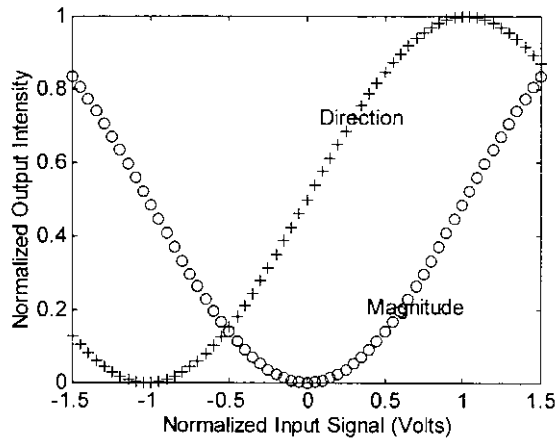

Figure 27: Transfer functions for the MZIs.

From the transfer functions, the output values from the *magnitude* MZI range from 0 to 0.5 for input signal between +1 volts and −1 volts and are symmetric about the input value of zero. The normalized comparator threshold voltage for the direction circuit is normalized at $V_T = 0.5$ V. The detected intensity from the *direction* MZI is compared to the normalized threshold to determine whether the intensity from the magnitude MZI should accumulate up or down. The accumulator comparator voltage polarity is used to direct the fiber lattice direction of accumulation. The recirculating fiber lattice structure accumulates downward if the output of the direction interferometer is less than 0.5 and upward for values greater than 0.5. Thus the direction interferometer, detector, comparator, and optical fiber lattice filter structure serve to function as an accumulator.

In applying optical integrated components to a $\Sigma\Delta$ architecture the first-order model is simulated. A computer simulation of the transfer function is shown in Fig. 25(b) using the interferometer model [63]. The accumulator H_{12} is modeled as an ideal accumulator. The simulation demonstrates the difference in the accumulator inputs when using a Mach-Zehnder interferometer is used to couple the antenna voltage and the feedback signals.

9.3.2 Second-Order $\Sigma\Delta M$

The block diagram for a second-order integrated optical $\Sigma\Delta$M is shown in Fig. 28 on the next page. Again, the two accumulators are modeled as ideal [63]. Simulation results for the second-order integrated optical $\Sigma\Delta M$ are plotted in Fig. 28b for 200 sampled-data values. The average value of

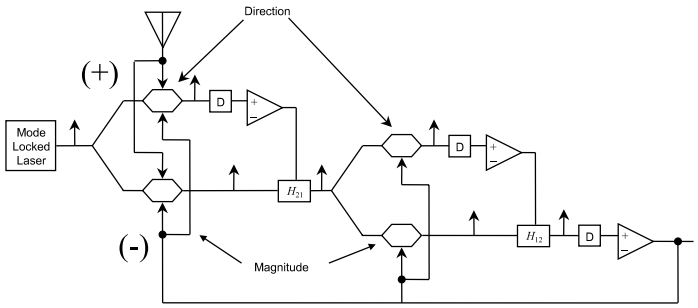

(a)

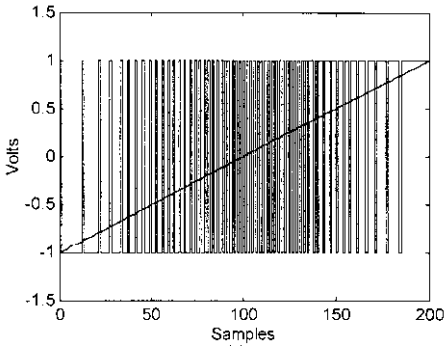

(b)

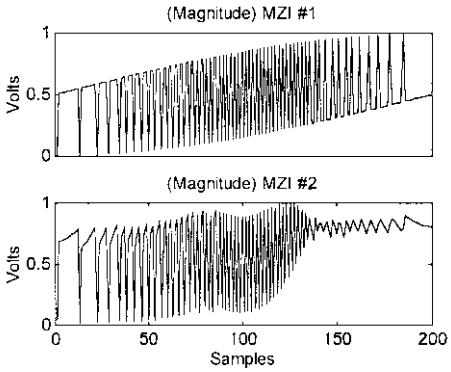

(c)

Figure 28: Second-order integrated optical ΣΔM. (a) Block diagram, (b) simulation results with ideal H_{12} and H_{21} and (c) intermediate signals at inputs to Magnitude MZIs.

the quantizer output can be seen to track the average value of the ramped input, similar to that shown in Fig. 21 on page 33. The output of the interferometer can be seen to oscillate about the ramped input. Figure 28c plots the intermediate signal values at the input of the magnitude MZIs in the accumulator stages. These results compare favorably to those of the all-electronic design and demonstrate the feasibility of using the Mach-Zehnder interferometer to subtract the feedback signal from the antenna voltage. In the next section, an investigation into using fiber lattice filter structures to function as accumulators within the integrated optical $\Sigma\Delta M$ is described.

9.4 Fiber Lattice Structures

In this section, the optical fiber lattice accumulators that are used in the integrated optical ΣΔM are examined in more detail. Models are designed and tested. The accumulator models are then used within the optical ΣΔM to investigate the performance. [64]

9.4.1 Transfer Functions

Fiber optic signal processing devices can be constructed to perform various functions, including convolution, correlation, matrix operations, frequency filtering, pulse train generation, and matched filtering. Fiber lattice structures described and used in this report depend on the time-domain matrix multiplication capability. A fiber lattice structure can be constructed with a pair of voltage-controlled directional couplers, and intra-coupler single-mode optical fiber. A two-state optical amplifier is added in the feedback to enable the accumulation. The use of optical amplifiers in fiber delay line filters provides an enhanced flexibility and have recently gained considerable attention [65, 66].

The general form of the fiber lattice structure is shown in Fig. 29. The inputs are X_1 and X_2, the outputs are Y_1 and Y_2. The blocks a_1 and a_0 are the directional couplers. The lines connecting the input and output to the directional couplers are optical fiber. The gain block G represents an optical fiber amplifier. A feedback delay is represented by the z^{-1} block. Although both X_1 and X_2 are inputs, they are not used simultaneously. Likewise, only one output is used for a particular input. The transfer functions from either input port to either output port are known. The transfer functions of interest here are those from the input X_1 to output Y_2 and from input X_2 to output Y_1.

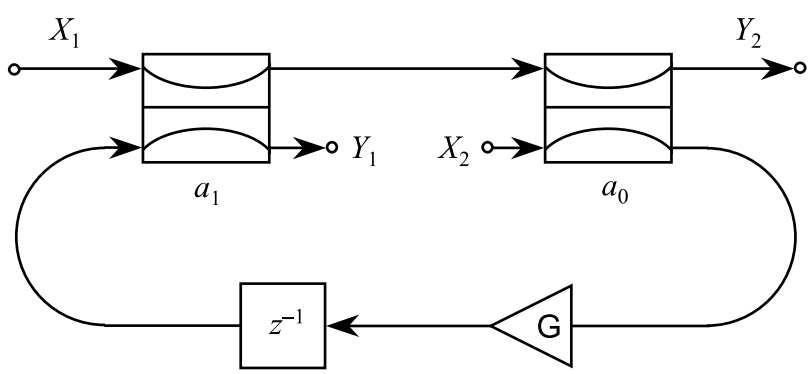

Figure 29: General fiber lattice structure.

The transfer function from X_1 to Y_2 is designated $H_{21}(z)$ [67, 68]. The specific fiber lattice structure for $H_{21}(z)$ is shown in Fig. 30. The input signal, X_1, is inserted into A of directional coupler a_1. The energy entering the directional coupler either couples to the adjacent waveguide (D), remains in the original waveguide (C), or combines with the energy from the feedback as determined by the coupling ratio of directional coupler a_1. Energy is inevitably lost to D with the $H_{21}(Z)$ fiber lattice structure. An example will illustrate this fact. If a coupling ratio of 0 (a bar-state) is used in order to avoid any energy from A transferring to D, the same coupling ratio will apply to energy arriving at B. Consequently, all energy at B will transfer to D.

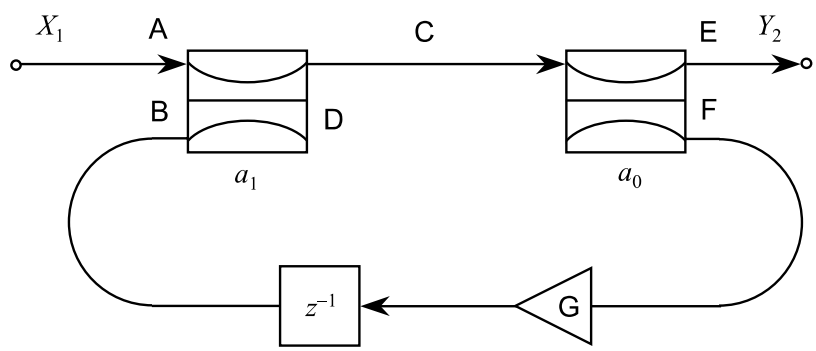

Figure 30: $H_{21}(z)$ fiber lattice structure.

Energy from B (cross-state) and A (bar-state) add coherently before arriving at C. Upon entering C of directional coupler a_0, energy will be divided according to the coupling ratio of that directional coupler. Energy that is in bar-state will arrive at the output (E). Cross-state energy will couple to the adjacent waveguide and arrive at F. This energy will undergo both optical gain and delay. The optical gain is performed with either a doped fiber with an optical pump or a semiconductor laser amplifier. The delay is dependent on the period of the pulsed laser used for sampling. A one-period delay was used in the testing section (as the sampling frequency increases, the length of fiber necessary for a one period delay is shorter). Finally, this energy returns to B.

Mason's gain rule and block diagram simplification generates the transfer function $H_{21}(z)$ and is depicted in Fig. 31 on the next page (the input and output are double blocked in this figure). The $1 - a_1$ and $1 - a_0$ blocks represent the bar-states, while the a_1 and the a_0 blocks represent the cross-state or coupling ratio. The energy lost to D is not shown to avoid clutter. The transfer function is

$$H_{21}(z) = \frac{(1 - a_0)(1 - a_1)}{1 - a_0 a_1 G z^{-1}} \,. \tag{65}$$

That is, the $H_{21}(z)$ fiber lattice structure is a first-order all-pole system and has one zero at the origin and one pole at $z = a_0 a_1 G$. This fiber lattice structure is stable as long as the pole remains inside the unit circle. This is assured when $a_0 a_1 G < 1$. Since both a_0 and a_1 are ratios and therefore are less than 1, the pole will remain inside the unit circle when $G < 1/a_0 a_1$. Additionally, the gain of the optical amplifier $G > 1$. These two limits serve as a check of the results obtained in the testing section. One observation supported later by testing results is that the coupling coefficients are interchangeable in H_{21}.

The transfer function from X_2 to Y_1 is designated $H_{12}(z)$ and has the delay and the amplifier in the feedforward path (see Fig. vreff7). The specific fiber lattice structure for $H_{12}(z)$ is shown in

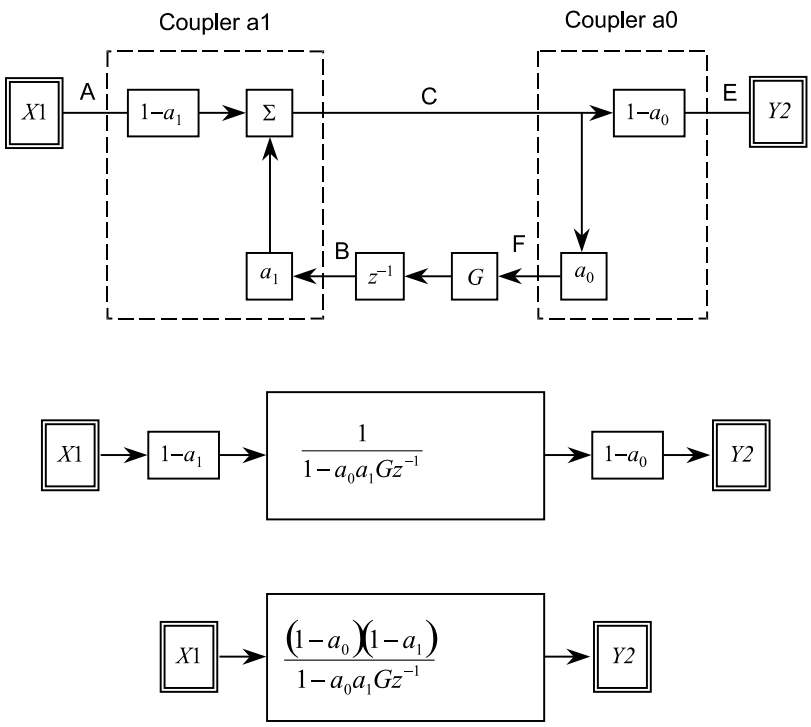

Figure 31: Generation of $H_{21}(z)$ fiber lattice structure.

Fig. 32. The input signal is inserted into directional coupler a_0 at A. Cross-state energy is lost to B (similar to that lost to D of Fig. 30 on page 40 $H_{21}(z)$). Bar-state energy is summed with cross-state energy from F and arrives at C before undergoing the amplification and delay. Energy arriving at D is divided according to the coupling ratio of directional coupler a_1. Bar-state energy will arrive at the output (E). Cross-state energy will couple to the adjacent waveguide, arrive at F and continue on to directional coupler a_0.

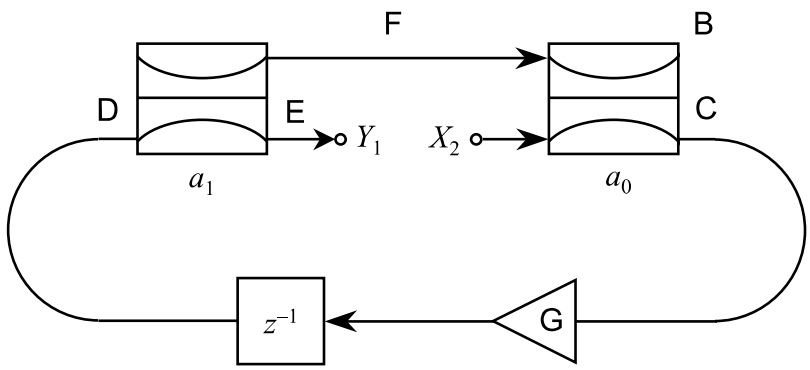

Figure 32: $H_{12}(Z)$ fiber lattice structure.

Similar to before, the $H_{12}(z)$ transfer function is generated using Mason's gain rule and block diagram simplification. The result is shown in Fig. 33 on the facing page. The energy lost to B is not shown to avoid clutter. The transfer function is

$$H_{12}(z) = \frac{(1-a_0)(1-a_1)Gz^{-1}}{1-a_0a_1Gz^{-1}}\,. \tag{66}$$

The $H_{12}(z)$ fiber lattice structure is a first-order pole-zero system and has the same pole as the $H_{21}(z)$ fiber lattice structure but has no zeros. Another difference is the optical gain in the feed-forward path. This results in a more rapid accumulation and is discussed further in the testing section. The limitations on the optical gain, hence the pole location, are the same as before and can be summarized as $1 < G < 1/a_0a_1$. Again, the coupling coefficients can be interchanged without affecting the transfer function.

9.4.2 Testing of Fiber Lattice Models

Both fiber lattice models were developed with MATLAB Simulink software [64]. The model for the $H_{21}(z)$ fiber lattice structure is shown in Fig. 34 on the next page. A modified Simulink model of the $H_{12}(z)$ fiber lattice structure is shown later. The directional coupler blocks include the cross and bar-states shown in Fig. 31 on the preceding page. The X_1 block continually repeats a programmed sequence. For example, a pulse train input is simulated with a constant value repeated at a 1 sample per second rate. The feedback delay block is variable, but was fixed at 1 sample per second rate. The feedback delay block is variable, but was fixed at 1 second for the tests performed.

The first test determines the required optical gain in order for Y_2 to increase monotonically across a range of coupling ratios. If the optical gain is too low, the fiber lattice structure saturates and settles at a fixed value after the typical overshoot and settling typically associated with damped control systems. If the optical gain is too high, the fiber lattice structure experiences exponential

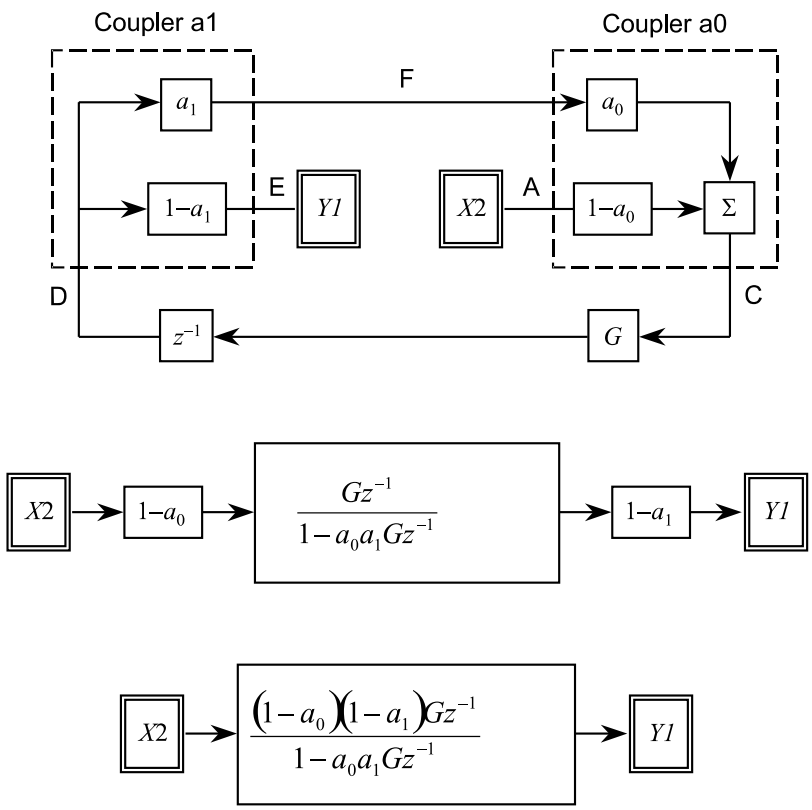

Figure 33: Generation of $H_{12}(z)$ fiber lattice structure.

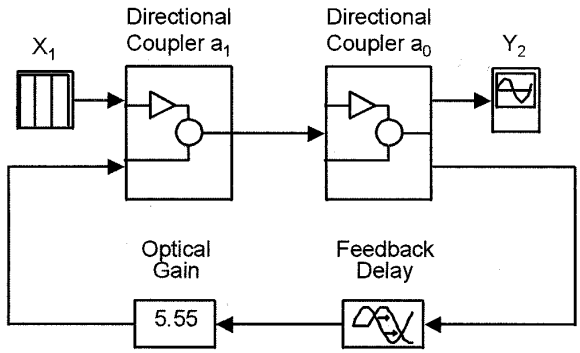

Figure 34: $H_{21}(z)$ Simulink model. (From [64].)

gain because the pole is outside of the unit circle. An optical gain that results in a monotonically increasing response is in between these two extremes. An example of all three values of G is shown in Fig. 35. In Fig. 35, the directional coupler a_1 was programmed for a 0.6 coupling ratio, while directional coupler a_0 had a 0.3 coupling ratio. At these coupling ratios, the G necessary for a monotonically increasing response is 5.555.

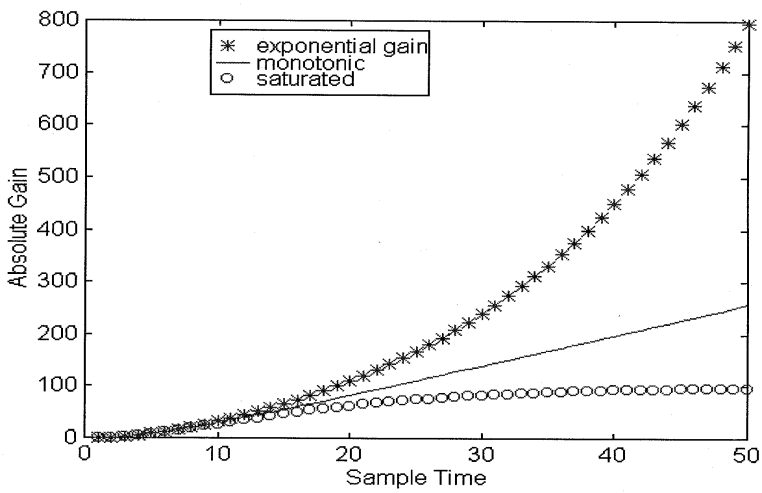

Figure 35: Tuning for monotonically increasing response. (From [64].)

The pole location corresponding to this gain and these coupling ratios is $a_0 a_1 G = 1$. Although a pole at $z = 1$ is stable, an increase in either coupling ratio or in G will quickly result in instability. Conversely, a decrease in either coupling ratio or G will quickly result in saturation and settling. The sensitivity of the $H_{21}(z)$ fiber lattice structure is demonstrated by the small difference in G used in Fig. 35 for the exponentially increasing response and the saturated response. The value of G is 5.72 and 5.4 for the exponentially increasing response and the saturated response, respectively. Similarly, the poles for these responses are at 1.03 and 0.972, respectively. These characteristics hold for all values of coupling ratios and G when the product $a_0 a_1 G \sim 1$. Table 4 on the next page lists the G necessary for a range of a_1 versus a_0 coupling ratios in order to get a monotonically increasing response. This table is a Toeplitz matrix. This means that, for a fixed G, the combination of $a_0 = X$ and $a_1 = Y$ ($0 < X < 1$ and $0 < Y < 1$) results in the same accumulation rate as $a_0 = Y$ and $a_1 = X$. This fact reinforces the earlier observation that the coupling coefficients in the transfer function are interchangeable. Table 4 and the characteristics discussed above apply to the $H_{12}(z)$ fiber lattice structure also.

Although the optical gain necessary to drive either fiber lattice structure to a monotonically increasing response is the same, the accumulation rate is different. The $H_{12}(z)$ fiber lattice structure accumulates faster because of the optical gain in the feed-forward path. To characterize the accumulation rates of each fiber lattice structure, the sample time necessary to reach an absolute gain of 100 was measured. The $H_{12}(z)$ and $H_{21}(z)$ fiber lattice structures testing results are contained in Tables 5 and 6, respectively. Both tables are again Toeplitz matrices. Data from Tables 4, 5, and 6 were used to generate Figs. 36(a), 36(b), and 36(c), respectively.

Table 4: Optical Gain: Monotonically Increasing Response. (From [64].)

		Coupling Ratio, a_0								
		0.1	**0.2**	**0.3**	**0.4**	**0.5**	**0.6**	**0.7**	**0.8**	**0.9**
	0.1	100	50	33.33	25	20	16.66	14.28	12.5	11.1
	0.2	50	25	16.65	12.5	10	8.33	7.15	6.25	5.55
Coupling	**0.3**	33.33	16.68	11.11	8.33	6.67	5.55	4.76	4.166	3.703
Ratio	**0.4**	25	12.5	8.34	6.25	5	4.166	3.57	3.125	2.78
a_1	**0.5**	20	10	6.68	5	4	3.333	2.85	2.5	2.22
	0.6	16.66	8.33	5.55	4.17	3.33	2.78	2.38	2.08	1.85
	0.7	14.28	7.14	4.76	3.57	2.86	2.38	2.04	1.785	1.587
	0.8	12.5	6.25	4.16	3.125	2.5	2.08	1.785	1.563	1.388
	0.9	11.1	5.56	3.7	2.78	2.22	1.852	1.588	1.389	1.234

Table 5: $H_{12}(z)$ Accumulation Rate: Monotonically Increasing Response. (From [64].)

		Coupling Ratio, a_0								
		0.1	**0.2**	**0.3**	**0.4**	**0.5**	**0.6**	**0.7**	**0.8**	**0.9**
	0.1	4.76	3.45	2.70	2.22	1.82	1.49	1.17	0.88	0.54
	0.2	3.45	2.38	1.85	1.49	1.20	0.96	0.75	0.54	0.31
Coupling	**0.3**	2.70	1.85	1.41	1.11	0.89	0.70	0.53	0.38	0.21
Ratio	**0.4**	2.22	1.49	1.12	0.88	0.69	0.54	0.40	0.27	0.12
a_1	**0.5**	1.82	1.20	0.89	0.69	0.54	0.41	0.29	0.20	0.097
	0.6	1.47	0.96	0.71	0.54	0.40	0.32	0.21	0.14	0.072
	0.7	1.17	0.75	0.53	0.40	0.32	0.21	0.14	0.086	0.036
	0.8	0.88	0.54	0.37	0.27	0.20	0.12	0.10	0.07	0.03
	0.9	0.53	0.32	0.18	0.16	0.09	0.07	0.036	0.03	0.025

Table 6: $H_{21}(z)$ Accumulation Rate: Monotonically Increasing Response. (From [64].)

		Coupling Ratio, a_0								
		0.1	**0.2**	**0.3**	**0.4**	**0.5**	**0.6**	**0.7**	**0.8**	**0.9**
	0.1	0.471	0.437	0.397	0.358	0.314	0.270	0.204	0.153	0.079
	0.2	0.437	0.403	0.370	0.330	0.289	0.243	0.195	0.138	0.077
Coupling	**0.3**	0.397	0.370	0.333	0.298	0.262	0.221	0.175	0.125	0.068
Ratio	**0.4**	0.358	0.330	0.298	0.266	0.232	0.196	0.149	0.107	0.059
a_1	**0.5**	0.314	0.289	0.262	0.232	0.201	0.165	0.129	0.091	0.043
	0.6	0.270	0.243	0.221	0.196	0.165	0.140	0.108	0.068	0.042
	0.7	0.204	0.195	0.175	0.149	0.129	0.108	0.086	0.063	0.031
	0.8	0.153	0.138	0.125	0.107	0.091	0.068	0.063	0.051	0.023
	0.9	0.079	0.077	0.068	0.059	0.053	0.042	0.031	0.023	0.020

Table 7: $H_{12}(z)$ Optical and In-Line Gain Necessary for Steady State Response. (From [64].)

		Coupling Ratio, a_0								
		0.1	**0.2**	**0.3**	**0.4**	**0.5**	**0.6**	**0.7**	**0.8**	**0.9**
Coupling Ratio a_1	**0.1**	1.1	1.16	1.235	1.325	1.436	1.587	1.8	2.145	2.873
	0.2	1.16	1.22	1.285	1.36	1.462	1.59	1.772	2.05	2.585
	0.3	1.235	1.285	1.338	1.407	1.49	1.597	1.74	1.95	2.315
	0.4	1.325	1.36	1.407	1.46	1.523	1.603	1.705	1.847	2.067
	0.5	1.436	1.462	1.49	1.523	1.562	1.609	1.667	1.742	1.844
	0.6	1.587	1.59	1.597	1.603	1.609	1.617	1.626	1.637	1.65
	0.7	1.8	1.772	1.74	1.705	1.667	1.626	1.582	1.534	1.483
	0.8	2.145	2.05	1.95	1.847	1.742	1.637	1.534	1.434	1.339
	0.9	2.873	2.585	2.315	2.067	1.844	1.65	1.483	1.339	1.216

Table 8: $H_{12}(z)$ Optical Gain Necessary for Steady Accumulation Down. (From [64].)

		Coupling Ratio, a_0								
		0.1	**0.2**	**0.3**	**0.4**	**0.5**	**0.6**	**0.7**	**0.8**	**0.9**
Coupling Ratio a_1	**0.1**	1.0	1.0	1.219	1.2	1.3	1.4	1.55	1.85	2.5
	0.2	1.0	1.06	1.2	1.2	1.35	1.4	1.5	1.8	2.3
	0.3	1.219	1.2	1.2	1.25	1.35	1.45	1.5	1.8	2.15
	0.4	1.2	1.2	1.25	1.3	1.35	1.45	1.5	1.7	1.95
	0.5	1.3	1.35	1.35	1.35	1.4	1.5	1.55	1.65	1.78
	0.6	1.4	1.4	1.45	1.45	1.5	1.5	1.55	1.57	1.6
	0.7	1.55	1.5	1.5	1.5	1.55	1.55	1.5	1.48	1.47
	0.8	1.85	1.8	1.8	1.7	1.65	1.57	1.48	1.42	1.33
	0.9	2.5	2.3	2.15	1.95	1.78	1.6	1.47	1.33	1.21

As shown in Fig. 36, the accumulation rates for both fiber lattice structures decrease as either coupling ratio increases. The reason for this is again related to the pole located at $a_0 a_1 G$. If either a_0 or a_1 increase, there is a proportional decrease in G for this test. Since G is lower each time through the feedback, the energy arriving back at directional coupler a_1 will be proportionally lower. From there, the bar-state energy will go to the output for the $H_{12}(z)$ fiber lattice structure. For the $H_{21}(z)$ fiber lattice structure, the decreased energy enters cross-state while combining with the bar-state input energy. This energy arrives at directional coupler a_0 before entering bar-state to the output. Either way, the energy at the output decreases with a lower G.

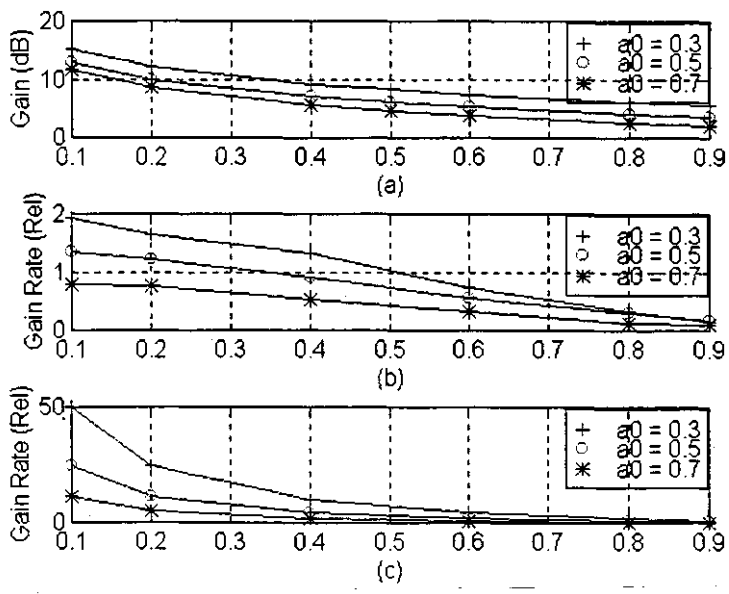

Figure 36: (a) Optical gain vs. a_1, (b) $H_{21}(z)$ accumulation rate vs. a_1, (c) $H_{12}(z)$ accumulation rate vs. a_1. (From [64].)

At the higher coupling ratios neither fiber lattice structure accumulates rapidly. The reason for the fall-off is that, as the coupling ratio increases, either the energy is permanently lost (i.e., D in Fig. 30 on page 40 or B in Fig. 32 on page 42) or the energy avoids the output (i.e., path CF in Fig. 30 or path DF in Fig. 32). Conversely, the accumulation rates are highest at the lower coupling ratios. At the lower coupling ratios, less energy is lost at the outset of accumulation (i.e., D in Fig. 30 is avoided) and more energy is directed toward the output (i.e., path CE in Fig. 30 or DE in Fig. 32). However, for the $H_{21}(z)$ accumulator a perfect bar-state will experience no accumulation at all because no energy will be crossed into the feedback loop to be increased by the optical amplifier. In fact, the output will be identical to the input.

To show "real-time" results and characteristics of a fiber lattice structure accumulating $H_{12}(z)$ fiber lattice structure was modified as shown in Fig. 37 on the next page. It was modified with the addition of a front-end optical amplifier, labeled "In-Line Gain (ILG)", and a comparator to drive the accumulation up or down. The comparator is modeled by a relay and a switch. When the control signal, simulated by the driver block, is greater than the threshold, the relay latches. The latches cause the switch to flip between the two optical gains. The greater G, labeled "Accum Up",

is for accumulating up and will be selected when driver is greater than the threshold. The other G is for accumulating down. The ILG is incorporated now because it is easier to tune the fiber lattice structures without the rest of the circuitry included in the $\Sigma\Delta$ modulators.

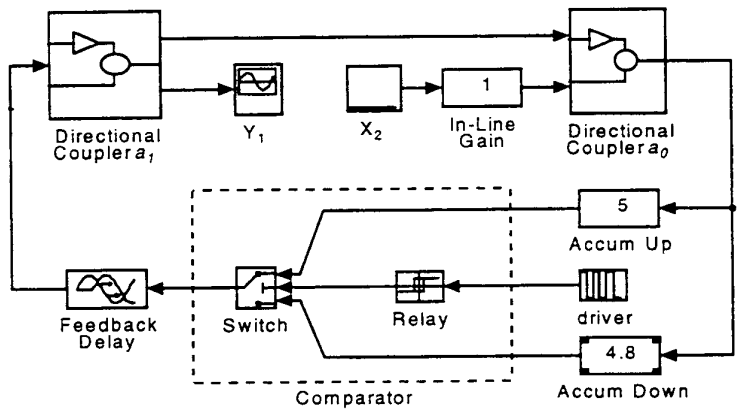

Figure 37: Modified Simulink model of $H_{12}(z)$ fiber lattice structure. (From [64].)

The ILG plays a critical role in the $H_{12}(z)$ fiber lattice structure accumulation rate because it is in the feed-forward path. Input X_2 is amplified before any coupling ratio divides the intensity among different ports. The sensitivity of the $H_{12}(z)$ fiber lattice structure to changes in ILG and the accumulation dependence on the comparator signal are shown in Fig. 38 on the facing page. The three curves were generated by fixing everything in Fig. 37 except the ILG. The coupling ratios used were $a_0 = 0.4$ and $a_1 = 0.5$. The Accum Up G used was that for a monotonically increasing response in Table 4 on page 45. The Accum Down G was chosen to generate a smooth curve when accumulating down. Choosing an Accum Down G a few tenths less than the Accum Up G generally gives good results.

As expected, the accumulation rate is proportional to ILG. This is evident not only in the initial rise from 0, but also in the rise and fall of the oscillating accumulation when the comparator is systematically switching between Accum Up G and Accum Down G. The relationship between the accumulation direction and the value of the comparator can be seen by comparing the pulses on the bottom of the plot with the peaks and valleys of the oscillations. Also, the value about which the three accumulations oscillate is proportional to ILG. For example, with ILG = 2 the accumulation oscillates about a relative gain of 175. The accumulation with ILG = 3 oscillates at approximately 265, or 3/2 greater than the accumulation with ILG = 2.

When the accumulation first begins, it appears that the first comparator transition from 1 to 0 is ignored because the accumulation continues up. Had Accum Up G been set to Accum Down G at the onset, the accumulation would have increased to a level above the level achieved when the comparator switched. Consequently, the accumulation continues up. When the second comparator transition occurs, the value is greater than the Accum Down G could support; therefore the fiber lattice structure accumulates down as desired. This apparent error is eventually corrected in time.

To show the $H_{12}(z)$ fiber lattice structure dependence on the Accum Down G, the ILG was left at 3 and everything else was fixed. A test run with Accum Up $G = 4.8$ (instead of 5) results in

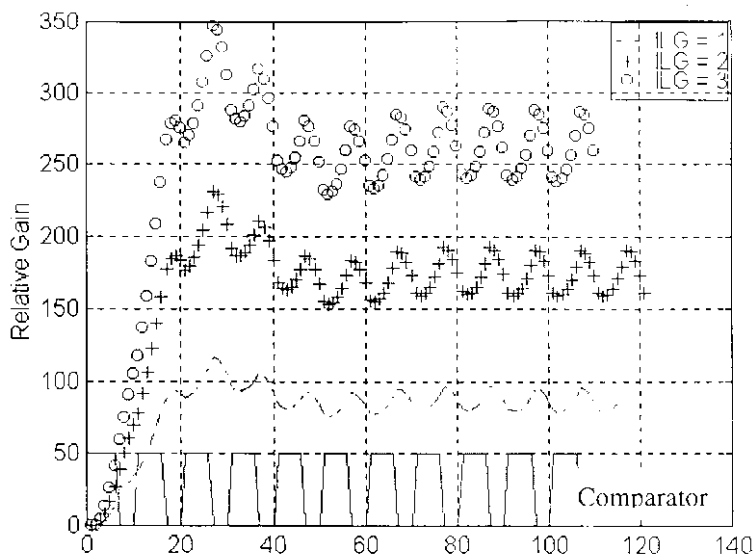

Figure 38: Effect of in-line gain on accumulation rate. (From [64].)

the fiber lattice structure saturating. Lower values result in a lower saturation value; therefore, the accumulator oscillates at lower values as seen in Fig. 39 on the next page. The Accum Down G was set to the Accum Up G for reference only. As the Accum G decreases, the $H_{12}(z)$ fiber lattice structure settles at a lower value. Although the change in Accum Down drastically affects the magnitude of the steady-state response, the oscillations about the plateau are roughly the same magnitude. One difference between varying the ILG and the Accum Down G is that the relative gain rate decreases proportionally to the ILG (see Fig. 38). The relative gain rate between peaks and valleys of Fig. 39 on the next page are approximately the same.

The final test generates the coupling coefficients, ILG, and Gs required in order for the $H_{12}(z)$ fiber lattice structure to follow a signal. In other words, if Z_2 is a step input, Y_1 is the steady-state response that settles at the input value. The ILG, Accum Up G, and Accum Down G versus coupling ratios a_0 and a_1 data are in Tables 8 and 7 on page 46. To simplify the implementation, the $H_{12}(z)$ fiber lattice structure was tuned with ILG equal to the Accum Up G. As mentioned before, good results can be generated with Accum Down G a few tenths less than the Accum Up G.

In summary, the fiber lattice structures discussed have one distinguishing characteristic and many common characteristics. The single difference between them is the accumulation rates as shown in Fig. 36 on page 47 and Tables 4, 5, and 6. The $H_{12}(z)$ fiber lattice structure accumulates more rapidly than the $H_{21}(z)$ fiber lattice structure for a given set of coupling ratios and Gs. The type of accumulation can be determined simply by knowing the pole position given by $a_0 a_1 G$. If $a_0 a_1 G < 1$, the fiber lattice structure will saturate; conversely, if $a_0 a_1 G > 1$, the output from the fiber lattice structure will grow exponentially. Monotonically increasing response will occur when the single pole is between the two extremes, which occurs when $a_0 a_1 G = 1$.

The resiliency of the fiber lattice structure is further demonstrated by the fact that the coupling ratios are interchangeable between both directional couplers. This characteristic is shown by the

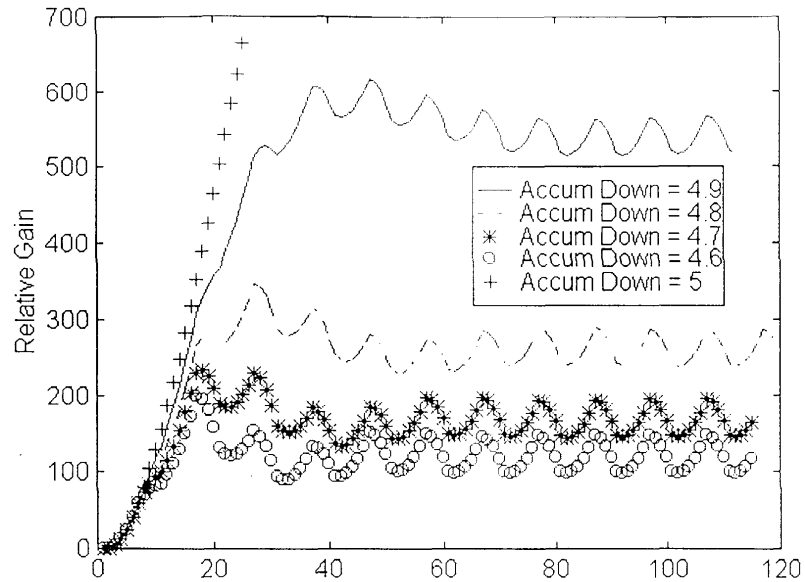

Figure 39: Effect of reducing Accumulate Down G. (From [64].)

tables. All of the tables are Toeplitz matrices. Tracking a signal with varying amplitude or frequency is as simple as controlling the optical gains and/or the voltage-controlled coupling ratios.

In the next section the fiber lattice structures are inserted into the sigma-delta modulators. Although a first-order sigma-delta modulator is inherently unstable and unreliable, replacing the ideal transfer function with a fiber lattice structure will serve as a proof of concept for optical accumulation. The $H_{12}(z)$ fiber lattice structure is used because it inherently has a wider range of accumulation rates available. Inserting both fiber lattice structures into the second-order sigma delta modulators results in more reliable and stable output.

9.4.3 First-Order Optical ΣΔM Using Fiber Lattice Accumulator Model

The optical amplifier preceding the fiber lattice structure plays the same role as the ILG discussed in Fig. 29 on page 39. The laser pulses that are input to both MZIs sample the signal due to the voltage difference between the antenna RF and the electrical feedback signals.

The $H_{12}(z)$ fiber lattice structure inherently has a wider range of accumulation rates; therefore, it is the more appropriate choice for the first-order sigma-delta modulator. Any particular combination of values of coupling ratios, ILG, and G can be pulled from Table 7 on page 46 and Table 8 on page 46 to demonstrate the validity of the ideal results. The ideal case did not account for either the effect of the optical amplifier in the feedforward path or the influence of the magnitude MZI. Instead of the magnitude MZI, the normalized directional MZI output was manipulated to closely follow the expected characteristics. The lack of an optical amplifier in the feedforward path was compensated by a front-end amplifier of 50. Regardless of these differences, the expected results closely follow those presented here for the same coupling ratios.

A ramp signal from -1 V to $+1$ V is input to both MZIs (see Fig. 40a). The output of the $H_{12}(z)$ fiber lattice structure and the output of the sigma-delta modulator are shown in Figs. 40b

and 40c, respectively. These results can be compared to similar results from the ideal case in Fig. 41 on the next page. In part (a) of both Figs. 40 and 41 is the identical ramp input. In Fig. 40b, the $H_{12}(z)$ fiber lattice structure accumulates until the comparator threshold of 0.5 V is exceeded. Sometimes there appears to be a lag between penetrating the threshold and the threshold value being subtracted from the MZIs, thereby reducing the $H_{12}(z)$ fiber lattice structure output. This is more a shortfall of the discrete nature of the simulation and the rapid rate of accumulation than a lagging modulator. Once the comparator threshold is breached, the threshold value is subtracted from the next sampled data input at the MZIs before propagating through the modulator again. The accumulation is more rapid between sample times of 70 and 180 than at other times. This is a function of the difference between the input and feedback signals. As the difference approximates the 0 value, the threshold is approached and exceeded more often. In Fig. 41b, the ideal case, the magnitude of the $H_{12}(z)$ transfer function output is greater than that generated in Fig. 40b. This is a direct result of the extreme front-end gain of 50 combined with the lack of accounting for the optical amplifier in the feedforward path of the $H_{12}(z)$ fiber lattice structure. The patterns are similar due to the dependence on the frequency of threshold crossings not the magnitude between the crossings.

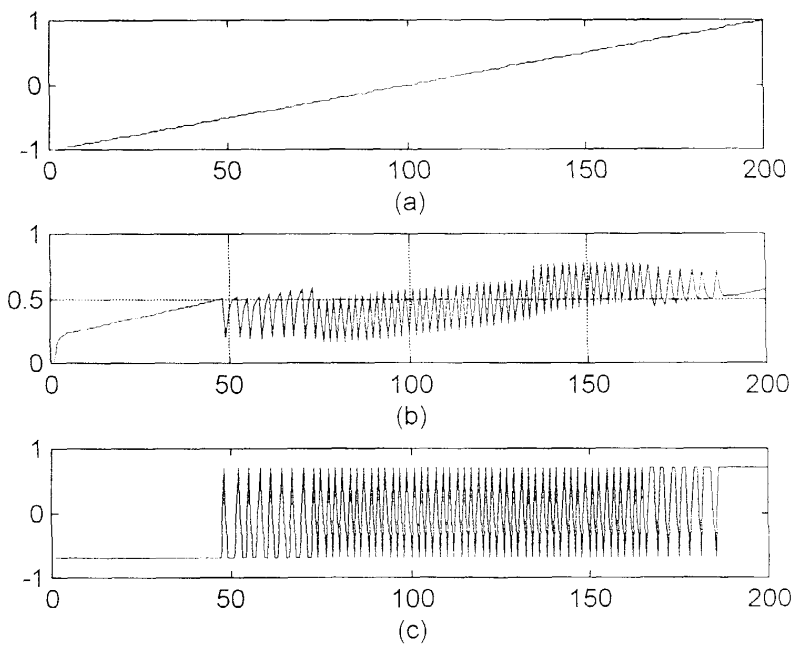

Figure 40: Optical first-order sigma-delta (a) ramp input, (b) $H_{12}(z)$ fiber lattice structure output, and (c) first-order sigma-delta modulator output. (From [64].)

The first-order sigma-delta modulator output shown in Figs. 40c and 41c is generated with a quantizer level of 0.7 volts. This means that when the comparator threshold is penetrated, a 0.7 V or a -0.7 V signal is generated. When the signal input to the comparator is between the quantizer values, the value of the output signal can be approximated by the weighting of the output. For example, if the discrete output in a given period is high 10% of the time, the magnitude of the signal

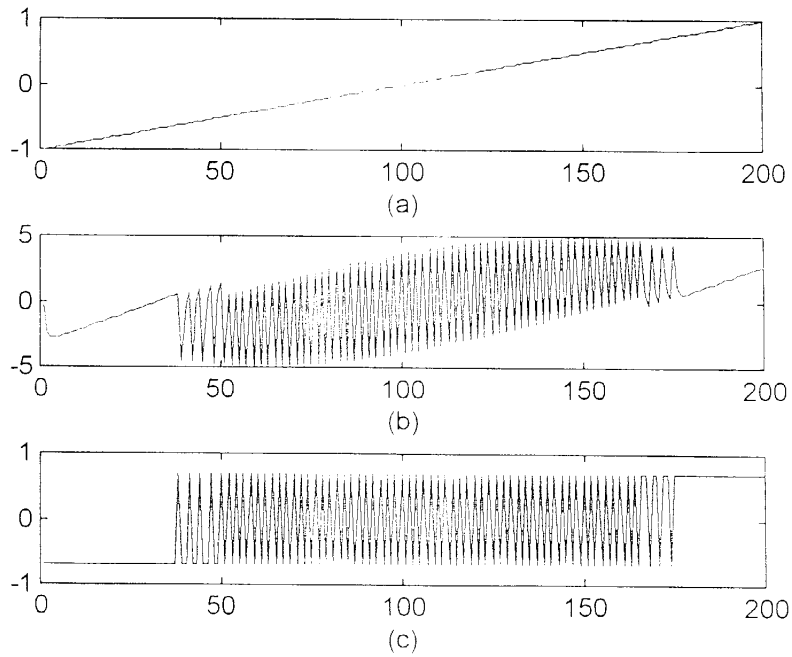

Figure 41: Ideal first-order sigma-delta (a) ramp input, (b) $H_{12}(z)$ transfer function output, and (c) first-order sigma-delta modulator output. (From [64].)

being quantized is the lower quantizer level (−0.7 V here) plus 10% of the difference between the values, or 1.4 V. The value of the signal at the end of this period of time is approximately −0.56 V.

The accumulation in Fig. 40 on page 51 is not as symmetric as Fig. 41. This is due to the influence of the G used for accumulating down, Accum Down G, shown in Fig. 42. Figure 42b is the same as Fig. 40c and is a result of Accum Up G and ILG equal to 1.74 and Accum Down G equal to 1.5. Figures 42a–d were generated by fixing everything except the Accum Down G. As the Accum Down G decreases, the accumulation rate slows down. This is shown by both the delay before the signal is discretized and the weighting of the discrete signal. For instance, in Figure 42(d) when the input signal is equal to 1, which occurs at the 200th sample, the discrete output is idling about 0. This corresponds to a value of 0. Conversely, with the other three Accum Down Gs the discrete output is latched to the resolution of the comparator. This means that the signal is at least 0.7 V. Since the input signal is symmetric, it appears that an Accum Down G of 1.62 gives the most accurate results.

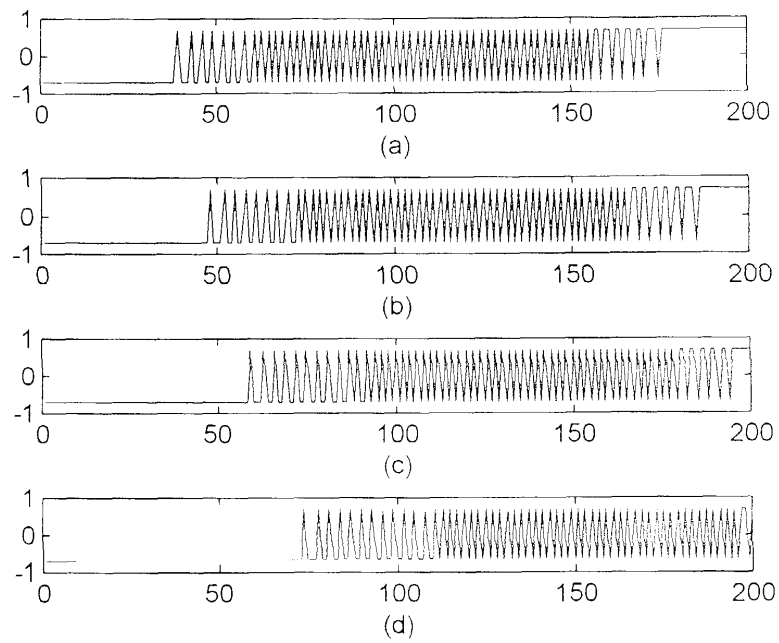

Figure 42: Effect of Accum Down G on first-order sigma-delta modulator output (a) Accum Down $G = 1.62$, (b) Accum Down $G = 1.5$, (c) Accum Down $G = 1.38$, and (d) Accum Down $G = 1.26$. (From [64].)

Since the accumulation improves as the Accum Down G approaches that of the Accum Up G, it appears that the situation when Accum Down G equals the Accum Up G might generate better results. As shown in Fig. 43 on the following page, the $H_{12}(z)$ fiber lattice structure and the discrete output appear to closely follow the ideal results presented by Ying [63] in Fig. 41 on the preceding page. For a constantly increasing signal like the ramp signal used, removing the Accum Down G seems to be a valid answer. Although that is true, real-world signals vary in frequency and magnitude, thus the need to have two different optical amplifications, Accum Up G and Accum Down G.

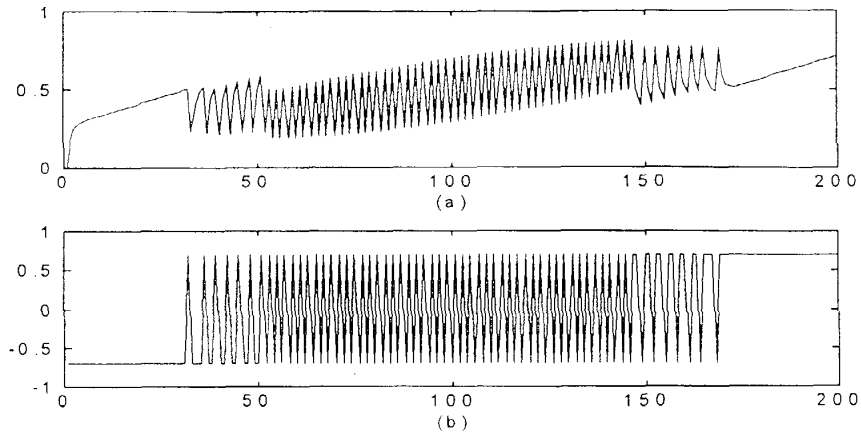

Figure 43: Accumulation with Accum Up equal Accum Down (a) $H_{12}(z)$ output, (b) discrete output. (From [64].)

Another input signal of interest is a dc signal. An accumulation should result in a discrete output known as pattern noise [69]. An input of 0.43 V was inserted in place of the ramp signal used before. The same coupling ratios, Accum Up G and Accum Down G, as used in Fig. 40 on page 51 were used to generate Fig. 44. A change in the ILG was necessary because the accumulation rate of the fiber lattice structure was 0.53 for $a_0 = 0.3$ and $a_i = 0.7$ (see Table 5 on page 45). The ILG was increased by the inverse of the accumulation rate, thus making it equal to $(0.53)^{-1}$ or 1.887.

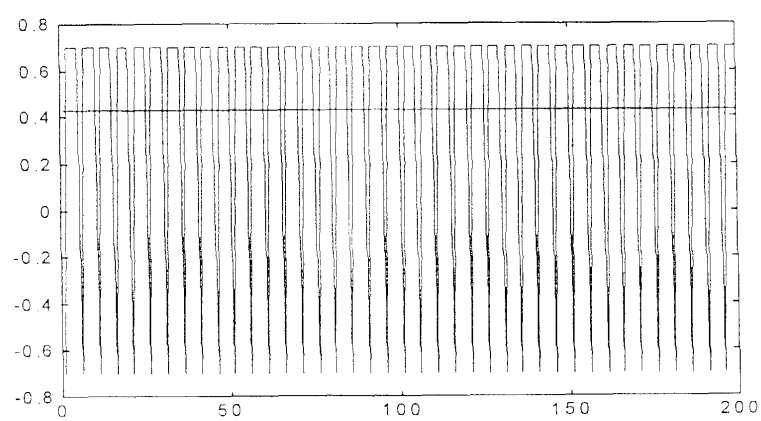

Figure 44: First-order sigma-delta discrete output with 0.43 V input. (From [64].)

As shown in Fig. 44, the discrete output is weighted towards the higher resolution, 0.7 V. The mean of the discrete output is 0.42 which approximately equals the input. The input is shown as a straight line near 0.42.

9.4.4 Second-Order Sigma-Delta Modulator with Fiber Lattice Accumulator Model

The $H_{21}(z)$ fiber lattice structure is placed in the first stage; the $H_{12}(z)$ fiber lattice structure is inserted into the second stage. Besides this, the difference between the first-order and the second-order is subtle. The first-order output comparator is removed and placed at the output of the second-order modulator. The feedback is compared to a signal in two places, one being the input into the second-order sigma-delta modulator and the other being the output of the first stage. The combination of the two fiber lattice structures should be a damped and more stable modulator when compared to the first-order sigma-delta modulator.

Preliminary results are shown in Fig. 45. These results were obtained by setting all coupling coefficients to 0.5, and the front-end gain of the second accumulator to 2. The Accum Up G of the $H_{21}(z)$ fiber lattice structure is that for a monotonically increasing response in Table 6 on page 45. For these coupling coefficients this value is 4. The Accum Down G was set at a few tenths less at 3.8. For the $H_{12}(z)$ fiber lattice structure, the Accum Up G and Accum Down G used are found in Tables 7 and 8. The front-end gain was not set to that in the table because the accumulation was too rapid but was instead set to a lower value of 2.

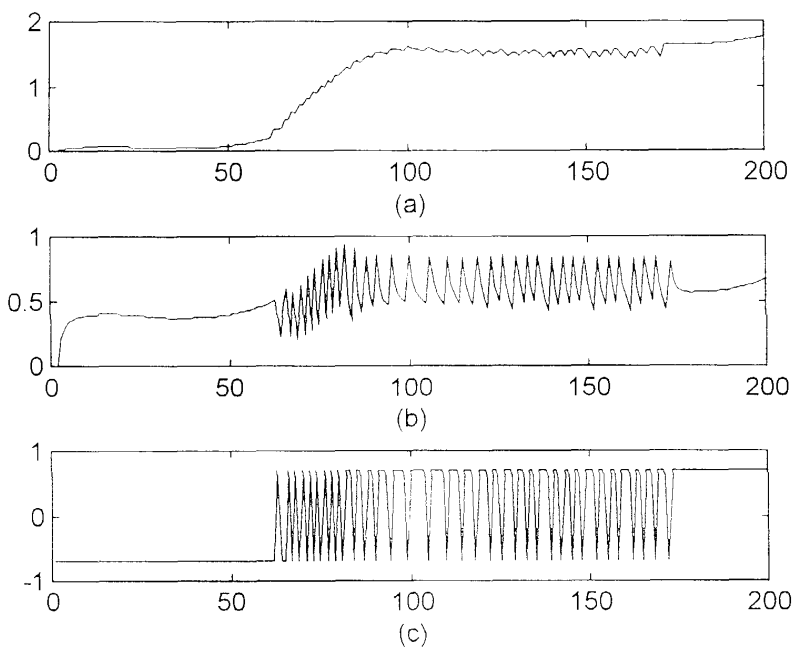

Figure 45: Second-order sigma-delta accumulation (a) $H_{21}(z)$ output, (b) $H_{12}(z)$ output, and (c) modulator output. (From [64].)

The damping effect of the $H_{21}(z)$ fiber lattice structure on the modulator can be seen in Fig. 45a. Once the first stage, $H_{21}(z)$, begins accumulating the second stage, $H_{12}(z)$, follows suit. The second stage and output quickly achieve a 50% duty cycle, meaning every other sample results in an accumulation that penetrates the threshold. The rest of the time oscillations continue with the mean of the idling pattern weighted toward the higher resolution of the output comparator.

Further fine tuning of the second-order sigma-delta modulation is necessary. The accumulation in this example is too rapid, but the outputs shown are symmetrical and convergent. Slower accumulation can be achieved with higher coupling ratios and lower optical gains. This example simply demonstrated that the second-order optical implementation of the second-order sigma-delta modulator is complete and accumulation characteristics are at least comparable to first-order results at this time.

In summary, the first-order results presented closely resemble the ideal results known *a priori*. One negligible difference between the ideal and the first-order sigma-delta with the fiber lattice accumulator was in the amplitude of the $H_{12}(z)$ accumulator output. This was due to a large front-end gain in the ideal case, but proved to be of little concern because the comparator only checks for threshold crossings, not the magnitude reached between crossings.

The lower optical amplifier value, Accum Down G, in the feedback determines when accumulation begins. When Accum Down G equals Accum Up G, the discrete output is symmetrical and looks like an attenuated ideal case. However, this holds only for the particular ramp input signal used. A difference of a few tenths between the Accum Up G and Accum Down G generally gives good results. A minor change in the optical gain is all that is necessary for the mean of the discrete output to equal a dc input.

Finally, the optical model of the second-order sigma-delta was shown, and preliminary results shown. Further study is necessary to understand how to fine tune the second-order sigma-delta modulator.

9.5 Free-Space S-SEED ΣΔM Designs

Two additional implementations of optical oversampling being researched (interferometric and non-interferometric) are based on error diffusion and interpolation coding and use symmetric self-electro-optic effect devices (S-SEED). [70–72] In error diffusion coding the large error that is associated with a single sample is diffused over many subsequent samples. The error to be diffused is usually generated by a binary quantizer (single-bit) with a linear filter in a feedback structure. Figure 46 on the facing page shows the block diagram of a generalized recursive error diffusion modulator. Here, $H(z)$ represents the z transform of a causal, unity gain filter that ensures complete diffusion of the error signal ϵ_n and z^{-1} is a unit sample delay. In the simplest case of first-order error diffusion, $H(z) = 1$ and the architecture of Figure 46 can be equivalently represented as the traditional single-loop ΣΔ modulator as discussed in the Section 9.2.

The input to the modulator, $x(n)$ is generated by oversampling the analog input signal $x(t)$. The difference between the modulator input and a delayed version of the quantizer error ϵ_{n-1} is quantized by the binary quantizer, where the quantizer error is defined as the difference between the output and the input to the quantizer, $\epsilon_n = q(u_n) - u_n$. For $H(z) = 1$ the nonlinear difference equation describing this modulator is [70]

$$u_n = x_n - \varepsilon_{n-1} = x_n + u_{n-1} - q(u_{n-1}) \tag{67}$$

for $n = 1, 2, \cdots,$. Since $u_n = x_n - \epsilon_n$ the above equation can be written as

$$q(u_n) = x_n + \epsilon_n - \epsilon_{n-1} \tag{68}$$

which shows the discrete time derivative of the error signal as discussed in the previous section.

A first-order bulk-optic implementation is shown in Fig. 47 on the next page [70]. In this bulk-optic implementation, the quantities are optical signals represented as complex field amplitudes. The coherent reference, lens, and slit arrangement provide for interferometric phase detection which

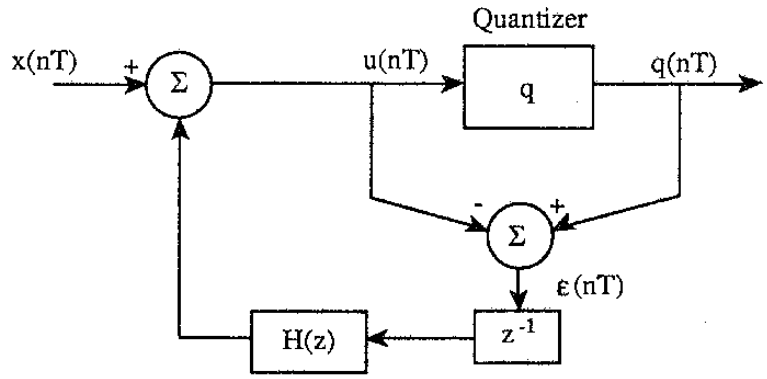

Figure 46: Block diagram of recursive error diffusion modulator. (From Ref. [70].)

is required for the zero threshold detection in the binary quantizer. The binary quantizer is implemented by a multiple-quantum well symmetric self-electro-optic effect device (S-SEED). The two slits in the phase detector are positioned to select the 0 and π maxima of the interference pattern. The S-SEED provides the binary quantization function as well as the optical gain necessary to overcome system losses. The photon energy is selected such that $dS/dV < 0$ and the operating point is unstable, thereby providing bistability. Here S is the responsivity and V is the applied voltage. The threshold is set by the external voltage V_0 and the ratio of the two input power levels P_{IN1} and P_{IN2} (integration of the optical pulse amplitude). Further details on this interferometric approach can be found in [70].

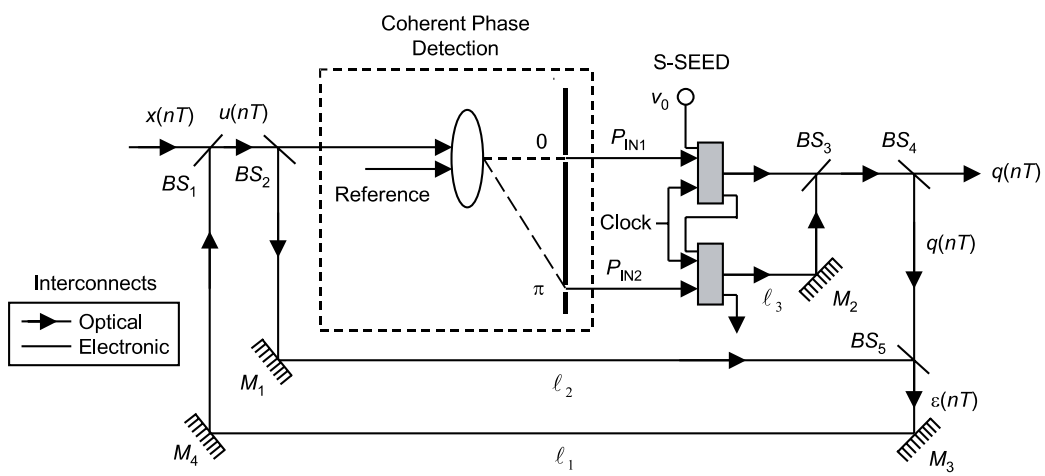

Figure 47: First-order interferometric error diffusion modulator. (From Ref. [70].)

The non-interferometric optical modulator is shown in Fig. 48 on the following page [**70**]. In this implementation x'_n is the unipolar modulator input that is generated by sampling $x(t)$ and then biasing x_n by $3q_s/2$ to insure that $x'_n \geq 0$ (non-negative signal operation within the modulator). In

this approach, two SEED devices are used to implement a non-interferometric optical subtraction. These two SEEDs are operated at a photon energy such that $dS/dV > 0$ and the operating point is stable. In this mode, the optical absorption of the SEED can be shown to be directly proportional to the current in the electronic bias circuit. The S-SEED is again used to provide binary quantization and optical gain but, in this configuration, the threshold is set by the external voltage V_0 and the *ratio* of u'_n and the optical reference.

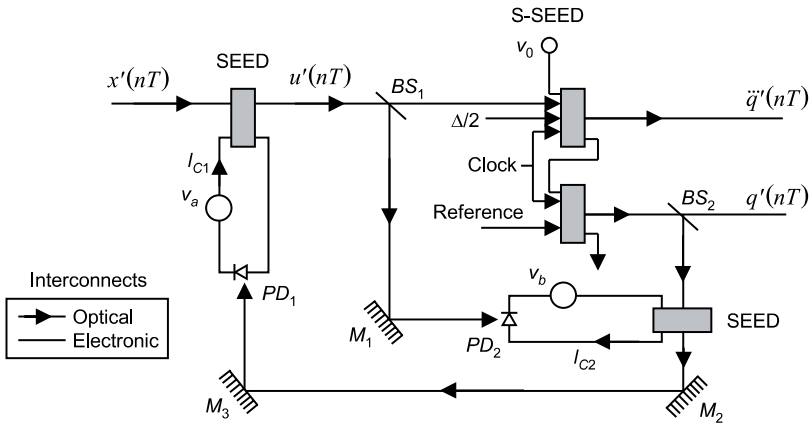

Figure 48: First-order non-interferometric error diffusion modulator. (From Ref. [70].)

The above techniques have the advantage of requiring only optical threshold and arithmetic operators and common optical components. Secondly, these architectures are also conveniently operated in conjunction with high speed optical sampling techniques using mode-locked laser sources (see Part I). S-SEED switching speeds are as fast as 3 ps and require low operating energy. Finally, these architectures may also be extendable to higher order designs but may still suffer from vibrations, etc., due to bulk-optic design.

10 Optical Undersampling DFT Receivers

10.1 Introduction

For wideband considerations where oversampling the signal is not an option, the pulse repetition frequency of the mode locked laser is usually governed by the Nyquist criteria. The Nyquist criteria assumes that the input signal is bandlimited ($0 \leq f \leq f_s/2$) before being sampled. The Nyquist theorem, however, only places a limitation on the information that can be derived from a single set of sampled data. That is, a single set of digitized data limits subsequent analysis to an $f_s/2$ bandwidth unless there is additional information available. With additional information, the frequency components $f > f_s/2$, which appear ambiguously due to undersampling, may be resolved.

There are several advantages to an optical undersampling receiver. Among these is the reduction in sampling speed necessary from the detectors. The receiver design presented in this section uses a CW laser eliminating the requirement for high-bandwidth pulsed-lasers. The main problem in an undersampled system is identifying the frequencies present (resolution of the ambiguities). One particular approach exploits the relationship between the discrete Fourier transform (DFT) and the symmetrical number system (SNS) to resolve all the ambiguities exactly [73]. The DFT naturally

encodes the frequency information of a signal in a format that is in the same form as the SNS. Consequently, aliases that result from undersampling a signal can be resolved exactly using $r \geq 2$ channels. Using the SNS properties of the DFT, the undersampling aliases can be easily resolved to a much greater extent than previously possible. In Section 10.2 we detail the relationship between the DFT and the SNS. We then present in Section 10.3 an optical undersampling DFT receiver concept for identifying a single (wideband) frequency.

10.2 The DFT and SNS Relationship

Consider a single-frequency signal sampled at two different sampling frequencies. Digital uniform sampling of an analog waveform with frequency f produces a discrete spectrum that is symmetrical about the sampling frequency $f_s/2$. Assume for this system that the two sampling frequencies are $f_{s1} = 10$ and $f_{s2} = 11$. After sampling, an analog input signal $x(t)$ becomes a discrete sequence $x(nT)$. This periodic sequence has a digital frequency given by $\omega = 2\pi(f/f_s)$. A signal with digital frequency $0 \leq \omega \leq \pi$ is indistinguishable from a signal with digital frequency $n\pi \leq \omega \leq (n+1)\pi$, $n = 1, 2, 3, \cdots$, which is an effect known as *aliasing*.

The digital frequency of a sampled sinusoid can be mapped into the z-domain as shown in Fig. 49a. For simplicity, assume as sinusoid $x(t) = 2\cos 2\pi f t$, and after sampling

$$x(n) = 2\cos\omega n = e^{j\omega n} + e^{-j\omega n}\,. \tag{69}$$

If $f = f_s/4$, this corresponds to $\omega = \pi/2$. If $f = f_s/2$, $\omega = \pi$. Since the signal is real, the signal poles appear in complex conjugate pairs on the z-plane. For frequencies between $f_s/2$ and f_s, the frequencies map back to their conjugate on the upper half of the complex plane. If the frequency is increased beyond f_s, a full trip is made around the unit circle, and the mapping repeats. Figure 49b illustrates the mapping with each triangle representing a full rotation around the unit circle in the z-plane. The abscissa represents the input analog frequency, whereas the ordinate represents the digital frequency mapping. Note that an infinite number of analog frequencies will map into each digital frequency $0 \leq \omega \leq \pi$.

Recall that the DFT is given by

$$X(k) = \sum_{n=0}^{N-1} x(n) e^{-j(2\pi nk/N)} \qquad k = 0, \cdots, N-1\,. \tag{70}$$

Application of the DFT to $x(n)$ yields a discrete spectrum, where $|X(k)|^2$ is the energy contained in the signal at each digital frequency $\omega = 2\pi k/N$. The discrete spectrum $X(k)$ has N indices with the digital frequency of each index given by

$$\left[0, 2\pi\frac{1}{N}, \cdots, 2\pi\frac{(N/2)}{N}, 2\pi\frac{(N/2+1)}{N}, \cdots, 2\pi\frac{(N-2)}{N}, 2\pi\frac{(N-1)}{N}\right] \quad \text{for } N \text{ even} \tag{71}$$

and

$$\left[0, 2\pi\frac{1}{N}, \cdots, 2\pi\frac{(N-1)/2}{N}, 2\pi\frac{(N+1)/2}{N}, \cdots, 2\pi\frac{(N-2)}{N}, 2\pi\frac{(N-1)}{N}\right] \quad \text{for } N \text{ odd} \tag{72}$$

The analog frequency corresponding to each index is obtained by multiplying each value by f_s. Since signals with digital frequencies in the range $\pi < \omega < 2\pi$ are indistinguishable from signal with digital frequencies $0 \leq \omega \leq \pi$, the digital frequency of each index can also be written as

$$\left[0, 2\pi\frac{1}{N}, \cdots, 2\pi\frac{(N/2)}{N}, 2\pi\frac{(N/2-2)}{N}, \cdots, 2\pi\frac{2}{N}, 2\pi\frac{1}{N}\right] \qquad \text{for } N \text{ even} \tag{73}$$

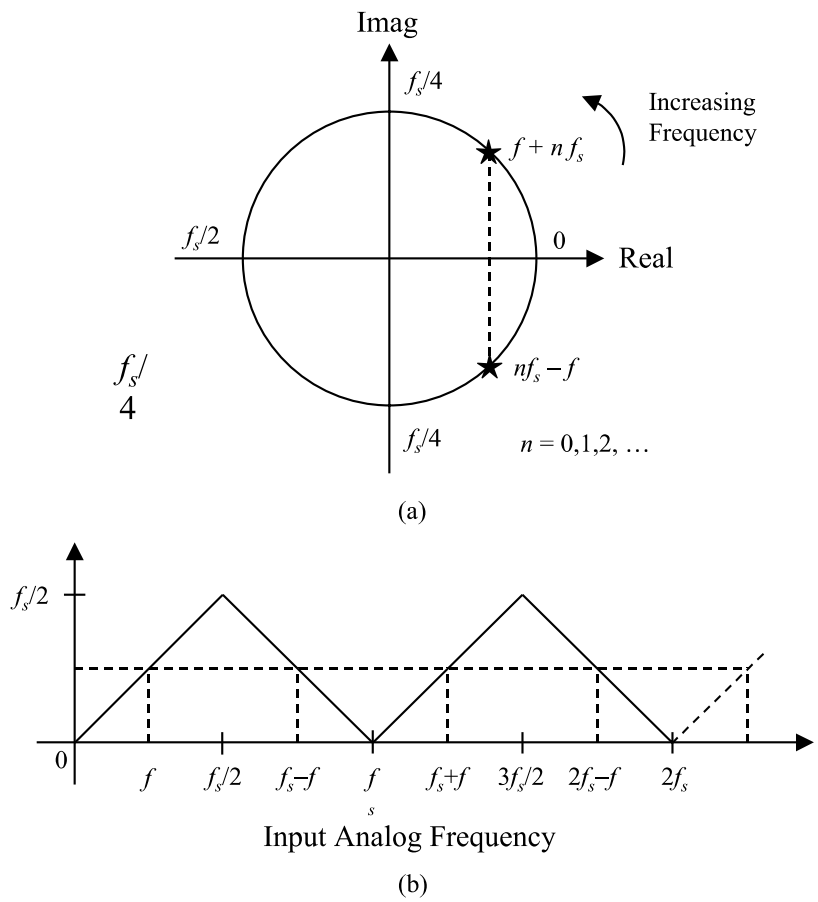

Figure 49: (a) z-plane mapping of an input analog signal, (b) sampled frequency output.

and

$$\left[0, 2\pi\frac{1}{N}, \cdots, 2\pi\frac{\lfloor N/2\rfloor}{N}, 2\pi\frac{\lfloor N/2\rfloor}{N}, \cdots, 2\pi\frac{2}{N}, 2\pi\frac{1}{N}\right] \qquad \text{for } N \text{ odd} \tag{74}$$

where $\lfloor x\rfloor$ represents the greatest integer less than or equal to x. More simply, the spectrum $X(k)$ resolves into N integer indices, and incoming signals will map into unique

$$\left[0, 1, \cdots, \frac{N}{2}, \frac{N}{2}-1, \cdots, 2, 1\right] \qquad \text{for } N \text{ even} \tag{75}$$

and

$$\left[0, 1, \cdots, \lfloor\frac{N}{2}\rfloor, \lfloor\frac{N}{2}\rfloor, \cdots, 2, 1\right] \qquad \text{for } N \text{ odd}. \tag{76}$$

That is, since frequency indices greater than $N/2$ are redundant for real signals, the highest unaliased frequency that can be observed corresponds to the $N/2$ index. From the above discussion, it is clear that the DFT maps real signals naturally into the symmetrical number system [74]. In this case, the modulus described in Ref. [74] is the sampling frequency f_s. The number of indices N is given by $N = f_2 T_L$, where T_L is the total sampling time.

Figure 50 on the next page illustrates the DFT mapping for two channels, where $f_{s1} = 10$ and $f_{s2} = 11$ for input frequencies $f = 0$ to 23. In this case, $T_L = 1$ so that $N_1 = 10$ and $N_2 = 11$. In the figure, the abscissa corresponds to the incoming frequency, whereas the ordinate corresponds to the bin into which the signal is resolved. Table 9 on page 63 displays the input frequency and the resulting DFT bin for each sampling frequency. Note that frequencies resolve as described in Eqs. 75 and 76. By considering both channels, it is possible to unambiguously resolve signal frequencies in the dynamic range determined by the SNS ($0 \le f \le 15$). The dynamic range of the receiver is determined by the collection of pairwise relatively prime moduli.

Theorem 1: Let $m_1, \cdots, m_r$ be pairwise relatively prime moduli, and let $A_0, A_1, A_2, \cdots$ be vectors formed by the symmetrical number system given by Eqs. 75 and 76.

a) If one of the moduli (m_1) is even, then the dynamic range of the system is

$$\hat{M} = \min\left\{\frac{m_1}{2}\prod_{\ell=2}^{j} m_{i_\ell} + \prod_{\ell=j+1}^{r} m_{i_\ell}\right\} \tag{77}$$

where j ranges from 2 to $r-1$, and $m_{i_2}, m_{i_3}, \cdots, m_i$, range over all permutations of $\{2, 3, \cdots, r\}$.

b) If all of the moduli are odd, then the dynamic range of the system is

$$\hat{M} = \min\left\{\frac{1}{2}\prod_{\ell=1}^{j} m_{i_\ell} + \frac{1}{2}\prod_{\ell=j+1}^{r} m_{i_\ell}\right\} \tag{78}$$

where j ranges from 1 to $r-1$, and $m_{i_1}, m_{i_2}, \cdots, m_i$, range over all permutations of $\{1, 2, \cdots, r\}$. As an example, let $m_1 = 4$, $m_2 = 3$, and $m_3 = 5$. We must minimize the set of values

$$\left\{\frac{m_1}{2} + m_2 \cdot m_3,\ \frac{m_1}{2}m_2 + m_3,\ \frac{m_1}{2}m_3 + m_2\right\} = \{17, 11, 13\}. \tag{79}$$

The dynamic range is the minimum value of this set (i.e., 11), as we verify from Table 10.

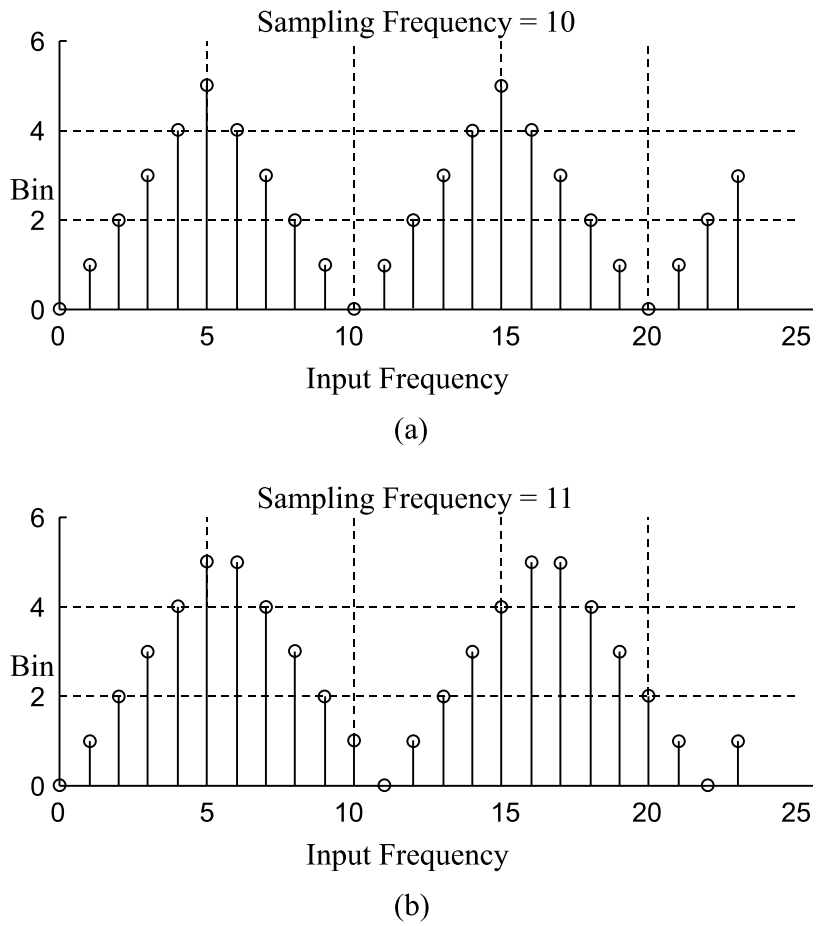

Figure 50: DFT mapping for input frequencies $f = 0$ to 23 for (a) $f_{s1} = 10$ and (b) $f_{s2} = 11$.

Table 9: Input Frequency and Resulting DFT Bins for Two Channel Example

Input Frequency f	**DFT Bins** $f_s = 10$	$f_s = 11$
0	0	0
1	1	1
2	2	2
3	3	3
4	4	4
5	5	5
6	4	5
7	3	4
8	2	3
9	1	2
10	0	1
11	1	0
12	2	1
13	3	2
14	4	3
15	5	4
16	4	5
17	3	5
18	2	4
19	1	3
20	0	2
21	1	1
22	2	0
23	3	1

Table 10: Integer Values for the $m_1 = 4$, $m_2 = 3$, and $m_3 = 5$ Example

	0	1	2	3	4	5	6	7	8	9	10	11	12	$\cdots$	
$m_1 = 4$	0	1	2	1	0	1	2	1	0	1	2	1	0	1	$\cdots$
$m_2 = 3$	0	1	1	0	1	1	0	1	1	0	1	1	0	1	$\cdots$
$m_3 = 5$	0	1	2	2	1	0	1	2	2	1	0	1	2	2	$\cdots$

10.3 Optical DFT Receiver

It is well known that optical devices exist that can compute a two dimensional (2-D) Fourier transform or its inverse in unit time. Optical-computing technology offers new challenges to algorithm designers since it can perform an n-point discrete Fourier transform (DFT) operation. A one-dimensional (1-D) n-point DFT operation (or its inverse) can be computed efficiently using a series of n 2-D DFTs. The assumption that the 2-D DFT can be computed in unit time is appropriate for many thin (linear) optical filters. The spherical lens generates the Fourier transform of an image in analog form. A DFT gate can be implemented with such a lens-based optical device. The resulting analog image only needs to be discretized in both space and amplitude to interpret it as an n-point DFT. Further details on the optical DFT are given in Ref. [75], [76].

Figure 51 shows the block diagram of a two-channel undersampling optical DFT/SNS receiver concept with channel moduli m_1 and m_2. The antenna signal is efficiently coupled into the optical domain using a guided-wave wideband interferometer. The antenna signal is used to frequency modulate the CW laser light. The light is split into two channels by a polarizing beam splitter. To translate the frequency information into the spatial domain the polarized light is sent to two separate diffraction gratings. The diffraction grating is an optical component that serves to periodically modulate the phase or the amplitude of the incident wave and is usually made of a transparent plate with periodically varying thickness or a periodically graded refractive index. Considering a diffraction grating whose thickness varies periodically with period Λ, the incident light ($\lambda \ll \Lambda$) traveling at an angle θ_i with respect to the direction of propagation is diffracted into several plane waves at small angles given by

$$\theta_q = \theta_i + q\frac{\lambda}{\Lambda} \tag{80}$$

$q \in \{0, \pm 1, \pm 2, \cdots, \}$ where q is called the *diffraction order*.

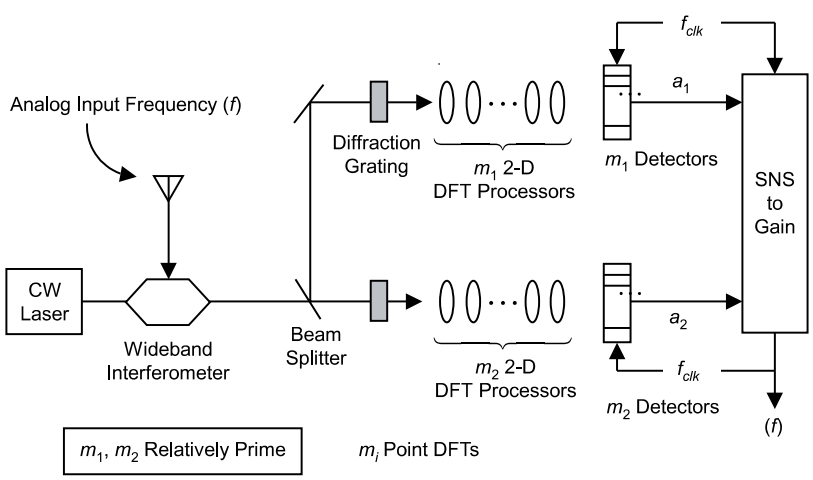

Figure 51: Block diagram of a two-channel optical undersampling DFT/SNS receiver.

The diffraction grating shown in Fig. 52 on the facing page translates the frequency information into the spatial domain. This spatial distribution is then collimated into the Fourier transform processor that computes an m_i-point DFT. The r moduli m_i must be pairwise relatively prime. After

computation of the m_1-point DFT and the m_2-point DFT, the light impinges on a corresponding number of 1-D spatially distributed detector-threshold gates. Each detector-threshold gate within the array has a zero output voltage unless the light intensity crosses a threshold. The positive output detector number (a_1 channel 1 and a_2 channel 2) corresponds to the DFT bin of the analog frequency. These bin numbers are then used to resolve the incoming frequency. A major advantage

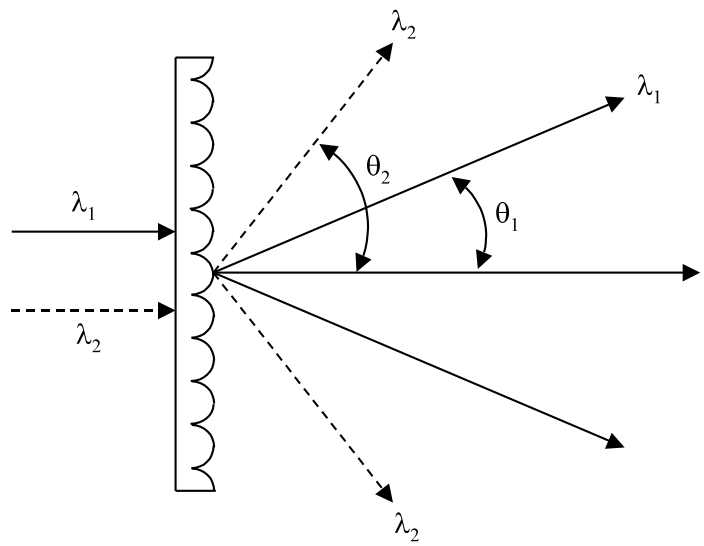

Figure 52: A diffraction grating directs two wavelengths λ_1 and λ_2 into two directions θ_1, θ_2 (spectrum analyzer).

of this optical DFT receiver is that only a few DFT coefficients (detector-thresholds) are required to resolve the ambiguous spatial frequencies. Resolution of the undersampled frequency is achieved by recombining the results of these low precision suboperations (detector-threshold gates a_1 and a_2) using an SNS-to-decimal algorithm [73]. Further investigation into the feasibility of an optical SNS DFT receiver is currently underway.

11 Non-Uniform Sampling Jitter

11.1 Spectrum Representations of Non-Uniformly Sampled Signals

Non-uniform sampling theory can be used to describe several important characteristics of jitter. By using asynchronous spectral averaging, this section develops expressions for the signal-to-noise ratio along with the expected noise floor. To start, let

$$g(t) \overset{F\{\cdot\}}{\Longleftrightarrow} G_a(\omega) \tag{81}$$

be the Fourier transform of a time domain analog signal $g(t)$ where the subscript a represents the analog transform of a signal that is bandlimited $(-1/2T,\ 1/2T)$ [77]. The analog signal $g(t)$ is *non-uniformly* sampled with overall period MT as shown in Fig. 53 on the next page. The sampled data sequence is treated as if it were obtained by sampling another function $\bar{g}(t)$ (also band limited)

at a *uniform* rate $(1/T)$. The goal is to find the digital spectrum of $\bar{g}(t)$ in terms of $G_a(\omega)$. Let the original sampled data sequence be represented by [78]

$$S = [g(t_0), g(t_1), \cdots, g(t_m) \cdots g(t_M), g(t_{M+1}), \cdots] \ . \tag{82}$$

Decomposing S into M subsequences we have

$$\begin{aligned} S_0 &= [g(t_0), g(t_M), g(t_{2M}), \cdots] \\ &\vdots \\ S_m &= [g(t_m), g(t_{M+m}), g(t_{2M+m}), \cdots] \\ &\vdots \\ S_{M-1} &= [g(t_{M-1}), g(t_{2M-1}), g(t_{3M-1}), \cdots] \end{aligned} \tag{83}$$

obtained by uniform sampling $g(t + t_m)$ at a rate of $1/MT$.

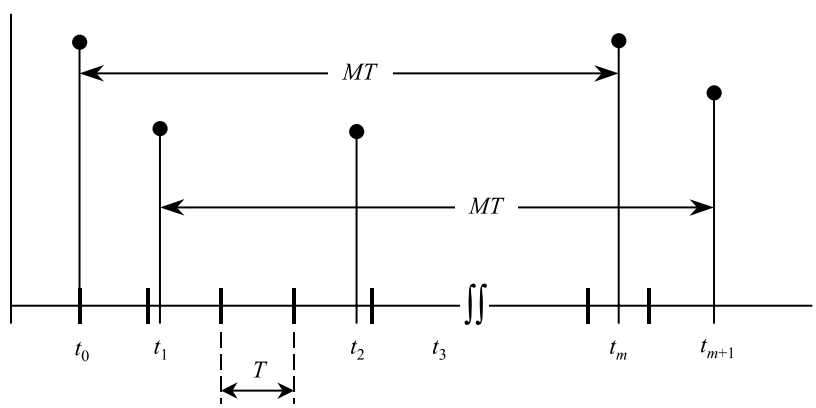

Figure 53: Non-uniformly sampled data sequence.

To reconstruct S, $M-1$ zeros are inserted between the samples in all sub-sequences S_m for $m = 0$ to $M-1$. That is,

$$\bar{S}_m = [g(t_m), 0, \cdots, (M-1 \text{ zeros}), g(t_{M+m}), 0, 0, \cdots] \ . \tag{84}$$

Second, $\bar{S}_m$ is shifted m positions to the right for $m = 0$ to $M-1$, i.e.,

$$\bar{S}_m z^{-m} = [(m \text{ zeros}), g(t_m), (M-1 \text{ zeros}), g(t_{M+m}), 0, 0, \cdots] \ . \tag{85}$$

Third, all of the sub-sequences are summed up to obtain the original sequence S

$$S = \sum_{m=0}^{M-1} \bar{S}_m z^{-m} \ . \tag{86}$$

The digital spectrum of S can be represented by the summation of those spectrums of $\bar{S}_m z^{-m}$ for $m = 0$ to $M-1$. That is,

$$G_1(\omega) = \left(\frac{1}{MT}\right) \sum_{m=0}^{M-1} \left[\sum_{k=-\infty}^{\infty} G_a \left[\omega - k\left(\frac{2\pi}{MT}\right)\right] e^{j[\omega - k(2\pi/MT)]t_m} \right] e^{-jm\omega T} \ . \tag{87}$$

Now we let

$$r_m = \frac{mT - t_m}{T}\,. \tag{88}$$

Solving for t_m we have

$$t_m = mT - r_m T \tag{89}$$

where $r_m T$ is the sampling time offset encountered at the mth sample (r_m means that the mth sample is delayed). Now we can rewrite $G_1(\omega)$ as

$$G_2(\omega) = \left(\frac{1}{T}\right) \sum_{k=-\infty}^{\infty} \left(\frac{1}{M} \sum_{m=0}^{M-1} e^{-j[\omega - k(2\pi/MT)]r_m T} e^{-jkm(2\pi/M)}\right) G_a\left[\omega - k\left(\frac{2\pi}{MT}\right)\right] \tag{90}$$

where G_1, G_2 are now general representations of the digital spectrum of a non-uniformly sampled signal.

These expressions can also be used to describe the behavior of *uniformly* sampled signals, $g(mT)$ [78]. That is, $\nu_m = 0$ and $t_m = mT$. If we substitute mT for t_m in $G_1(\omega)$ or $r_m = 0$ in G_2 we have

$$G(\omega) = \frac{1}{T} \sum_{k=-\infty}^{\infty} \left(\frac{1}{M} \sum_{m=0}^{M-1} e^{-jkm(2\pi/M)}\right) G_a\left[\omega - k\left(\frac{2\pi}{MT}\right)\right]\,. \tag{91}$$

Note in above

$$\sum_{m=0}^{M-1} e^{-jkm(2\pi/M)} = \begin{cases} M\ ; & \text{for } k = 0, M, 2M \\ 0\ ; & \text{otherwise} \end{cases} \tag{92}$$

and therefore

$$G(\omega) = \left(\frac{1}{T}\right) \sum_{k=-\infty}^{\infty} G_a\left[\omega - k\left(\frac{2\pi}{T}\right)\right] \tag{93}$$

which is the well known digital spectrum representation of a uniformly sampled signal.

11.1.1 Specific Case

As a specific case, the digital spectrum of non-uniformly sampled sinusoid is examined. Consider a sinusoid $e^{j\omega_0 t}$ with frequency f_0. The spectrum is

$$G_a(\omega) = 2\pi\delta(\omega - \omega_0)\,. \tag{94}$$

Substitution into $G_2(\omega)$ gives

$$G(\omega) = \left(\frac{1}{MT}\right) \sum_{m=0}^{M-1} \sum_{k=-\infty}^{\infty} 2\pi\delta\left[\omega - \omega_0 - k\left(\frac{2\pi}{MT}\right)\right] e^{-jr_m 2\pi f_0/f_s} e^{-jkm(2\pi/M)}\,. \tag{95}$$

If we now define a sequence $A(k)$ $k = 0, 1, 2, \cdots, M-1, M, \cdots$ by

$$A(k) = \sum_{m=0}^{M-1} \left[\frac{1}{M} e^{-jr_m 2\pi f_0/f_s}\right] e^{-jkm(2\pi/M)}\,, \tag{96}$$

(periodic on k with period M) then we can rewrite $G(\omega)$ above as

$$G(\omega) = \frac{1}{T} \sum_{k=-\infty}^{\infty} A(k) 2\pi \delta \left[\omega - \omega_0 - k \left(\frac{2\pi}{MT} \right) \right] \tag{97}$$

(periodic on ω with period $2\pi/T = 2\pi f_s$). In summary, $G(\omega)$ and $A(k)$ are the complete spectral representations of a non-uniformly sampled sinusoid.

11.1.2 Properties

1) One period of the spectrum comprises M line spectra uniformly spaced with neighboring s separated by f_s/M as shown in Fig. 54.

2) For r_m small $|A(k)| \approx |A(M-k)|$.

3) $A(k) = 0, 1, \cdots, M-1$ is the DFT of the sequence

$$\frac{1}{M} e^{-j r_m 2\pi f_0 / f_s}, \quad m = 0, 1, \cdots, M-1 \,. \tag{98}$$

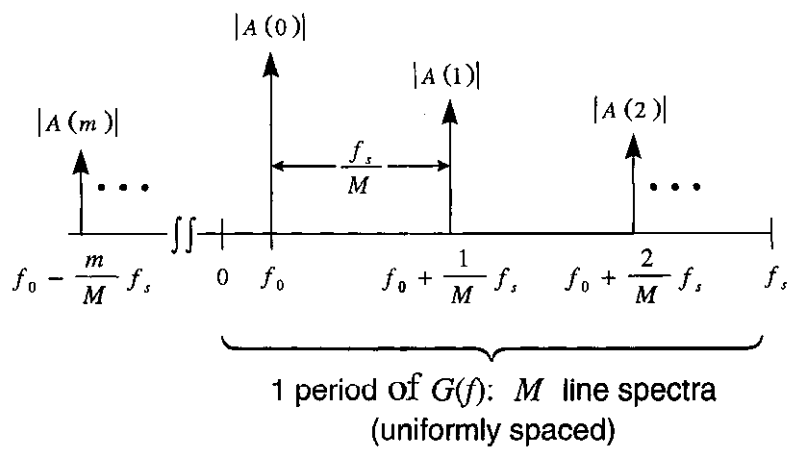

Figure 54: Line spectra at integer multiples of the sampling frequency.

11.1.3 Signal-to-Noise Ratio

To develop the expression for the SNR we show Parseval's relationship for the DFT given as

$$\sum_{n=0}^{M-1} |x(n)|^2 = \frac{1}{M} \sum_{k=0}^{M-1} |X(k)|^2 \,. \tag{99}$$

By Parseval's theorem, the sum of the square of $|A(k)|$ is equal to M times the sum of the square of

$$\left| \frac{1}{M} e^{-j r_m 2\pi f_0 / f_s} \right| \tag{100}$$

which is 1. That is,

$$\sum_{k=0}^{M-1} |A(k)|^2 = 1\,. \tag{101}$$

This gives the S/N as

$$\frac{S}{N} = 10\log\left(\frac{|A(0)|^2}{1-|A(0)|^2}\right)\ \text{dB}\,. \tag{102}$$

11.1.4 Independent Random Sampling

The jitter is now considered to be the result of independent random sampling. For independent random sampling r_m, $m = 0, 1, \cdots, M-1$ are $M-1$ independent identically distributed random variables (iid R.V.). The relationships

$$\sum_{k=0}^{M-1} |A(k)|^2 = 1 \tag{103}$$

and

$$\frac{S}{N} = 10\log\left(\frac{|A(0)|^2}{1-|A(0)|^2}\right)\ \text{dB} \tag{104}$$

still hold for each realization of the random sequence r_m. Hence, for expected S/N we need only to replace $|A(0)|^2$ by $E\{A(0)A^*(0)\}$. Assume $\alpha_m = r_m f_0/f_s$, $m = 0, 1, 2, \cdots, M-1$ be M iid R.V. with probability density function $p(\alpha)$, and characteristic function $\Phi(\omega) = E\{e^{j\omega\alpha}\}$.[2] From

$$A(k) = \sum_{m=0}^{M-1}\left[\frac{1}{M}e^{-jr_m 2\pi f_0/f_s}\right]e^{-jkm(2\pi/M)} \tag{105}$$

the signal power is [78]

$$\begin{aligned} E\{A(0)A^*(0)\} &= \left(\frac{1}{M}\right)^2 \sum_{m=0}^{M-1}\sum_{n=0}^{M-1} E\left\{e^{-j2\pi(\alpha_m-\alpha_n)}\right\} \\ &= \frac{1}{M} + \frac{1}{M^2}(M^2-M)\left(|\Phi(2\pi)|^2\right) \\ &= |\Phi(2\pi)|^2 + \frac{1}{M}\left[1-|\Phi(2\pi)|^2\right]\,. \end{aligned} \tag{106}$$

The S/N is then

$$\begin{aligned} \frac{S}{N} &= 10\log\left(\frac{E\{A(0)A^*(0)\}}{1-E\{A(0)A^*(0)\}}\right)\ \text{dB} \\ &= 10\log\left(\frac{(M-1)\,|\Phi(2\pi)|^2+1}{(M-1)\left[1-|\Phi(2\pi)|^2\right]}\right)\ \text{dB}\,. \end{aligned} \tag{107}$$

[2] For a brief review of characteristic functions see Appendix C.

If we assume α_m is *uniformly distributed* between $-a/2$ to $a/2$ (uniform sampling),

$$p(\alpha) = \frac{1}{a} \tag{108}$$

and

$$\Phi(2\pi) = \frac{\sin(\pi a)}{\pi a}\,. \tag{109}$$

If α_m is *normally distributed* $(\mu = 0, \sigma)$,

$$p(\alpha) = e^{-\alpha^2/2\sigma^2} \tag{110}$$

and

$$\Phi(2\pi) = e^{-2\pi^2\sigma^2}\,. \tag{111}$$

The question we would like to answer is how does the S/N behave near the origin if α_m, $m = 0, 1, 2, \cdots, M-1$ has a normal distribution? This normal approximation is a good noise model for sampling jitter. First we substitute $e^{2\pi^2\sigma^2}$ for $|\Phi(2\pi)|$ in the above expression where σ is the standard deviation (s.t.d.) of $\alpha_m = (r_m f_0)/f_s$. Then a Taylor series expansion of the log function argument is constructed retaining only the first significant term [79]

$$\frac{S}{N} = 20\log\left[\frac{1}{\sqrt{12}\sigma}\right] - 10\log\left(\frac{(M-1)\pi^2}{3M}\right)\ \text{dB}\,. \tag{112}$$

To investigate the noise floor, we take a sinusoidal waveform of record length N and an FFT of size N. Then we measure the S/N. We can use the result above to derive the s.t.d. σ_r of the clock jitter r_m as

$$\frac{S}{N} = 20\log\left(\frac{1}{\sigma_r}\right) + 20\log\left(\frac{f_s}{f_0}\right) - 10\log\left[4\pi^2\frac{(N-1)}{N}\right]\ \text{dB}\,. \tag{113}$$

where we have substituted $\sigma = \sigma_r f_0/f_s$ and brought the $\sqrt{12}$ to the last term. In a practical environment, other factors such as harmonic distortion, DC offset, and the stochastic nature of clock jitter may shift the SNR and obscure the measurement result. The solution here is to use asynchronous spectral averaging as shown in Fig. 55. Since we measure the S/N floor ratio, we need to adjust the above equation as follows

$$\frac{S}{N}(\text{floor}) = 20\log\left(\frac{1}{2\pi\sigma_r}\right) + 20\log\left(\frac{f_s}{f_0}\right) + 10\log\left(\frac{N}{2E_B}\right)\ \text{dB}\,. \tag{114}$$

Note that the $(N-1)/N$ term is dropped (≈ 1). Also, the factor of N accounts for the fact that the noise power of the jitter is uniformly distributed among all N frequency bins. The factor of 2 is the adjustment for the conversion between the sinusoid and the complex exponential $e^{j\omega_0 t}$. E_B is the adjustment for the window function used in the FFT.

11.1.5 Simulation Results

In order to verify the expressions above a simulation was used [79]. A four-term Blackman-Harris window ($E_B = 2$) with sampling frequency $f_s = 20$ MHz, and signal frequency $f_0 = 9,135,780$ Hz is used with $N = 256$ and where $\sigma_r = 0.001$ (0.1%). The results are shown in Fig. 56 on the next page. From Eq. 114, the $S/N(\text{floor ratio}) = 69$ dB which agrees closely the simulation results. Using the same degree of sampling uncertainty, the simulation results are now run with $N = 512$,

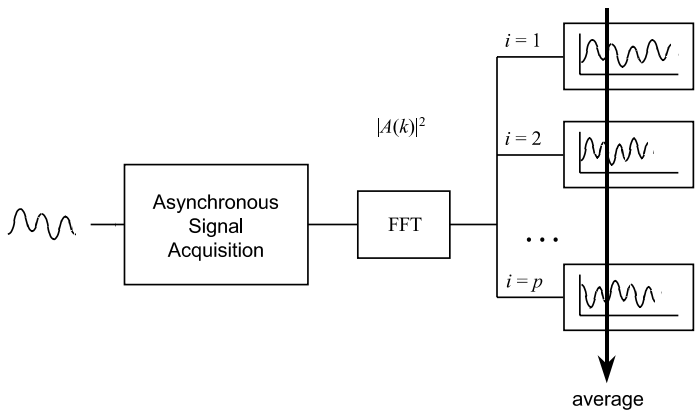

Figure 55: Asynchronous spectral averaging.

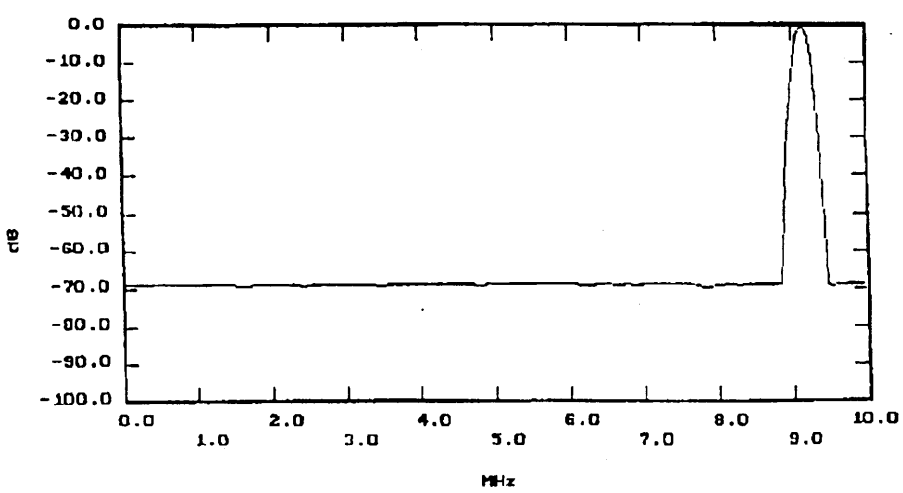

Figure 56: Simulation results using a four-term Blackman-Harris window ($E_B = 2$), a sampling frequency of 20 MHz, N=256, f_0=9,135,780 Hz and σ_r =0.001. (From [79].)

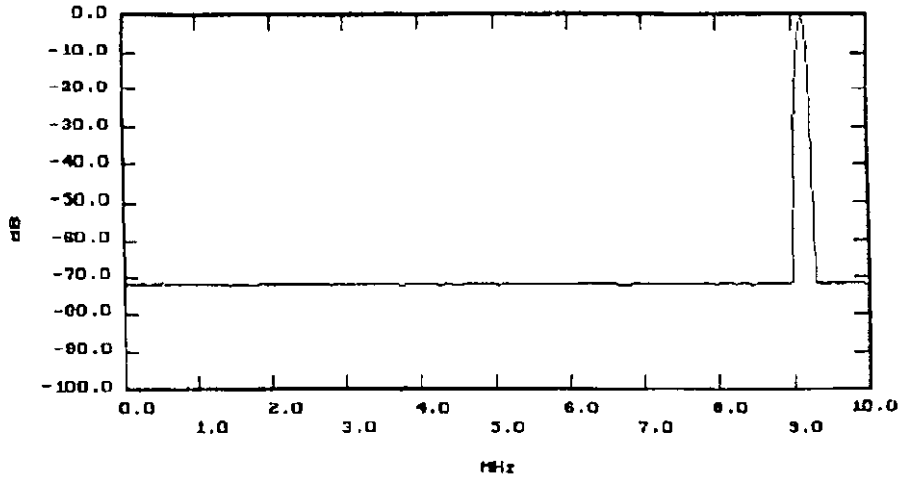

Figure 57: Simulation results using a four-term Blackman-Harris window ($E_B = 2$), a sampling frequency of 20 MHz, N=512, f_0=9,135,780 Hz and σ_r =0.001. (From [79].)

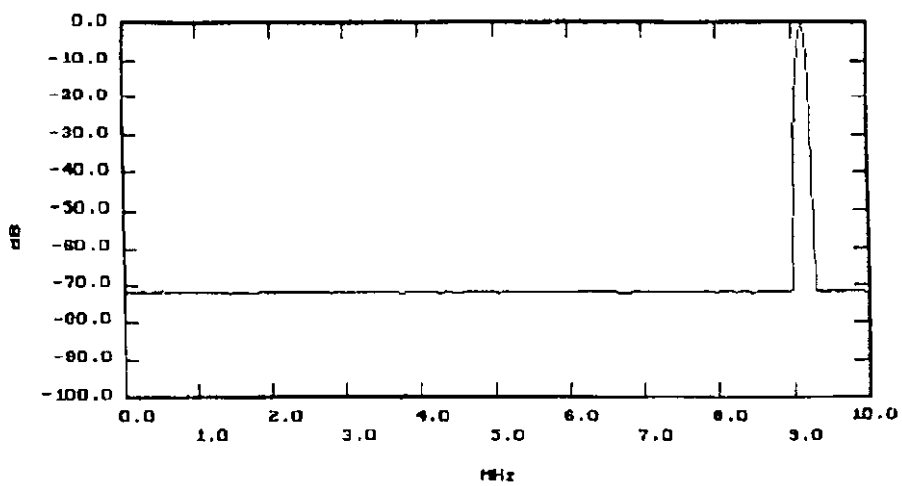

Figure 58: Simulation results using a four term Blackman-Harris window ($E_B = 2$), a sampling frequency of 20 MHz, N=1024, f_0=9,135,780 Hz and σ_r =0.001. (From [79].)

and $N = 1024$. The predicted noise floors are -72 dB and -75 dB, respectively. Simulation results are shown in Fig. 57 on the preceding page and Fig. 58 on the facing page, respectively, and show close agreement with the predicted values. Using the simulation with $f_0 = 4,567,890$ Hz, the noise floor is predicted to be -81 dB (as verified in Fig. 59). Changing the jitter component with $\sigma_r = 1.0\%$, the noise floor is predicted to be -55 dB. Figure 60 show the simulation results for this case and, again, shows good agreement with the predicted results.

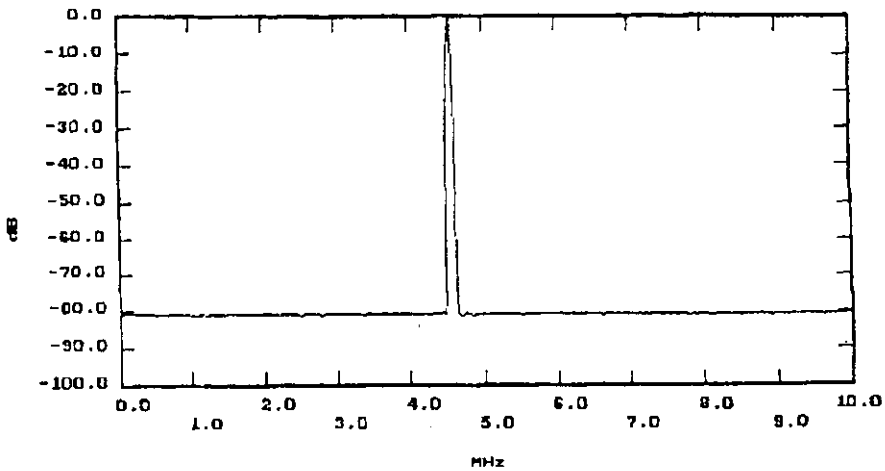

Figure 59: Simulation results using a four-term Blackman-Harris window ($E_B = 2$), a sampling frequency of 20 MHz, N=1024, f_0=4,567,890 Hz and σ_r =0.001. (From [79].)

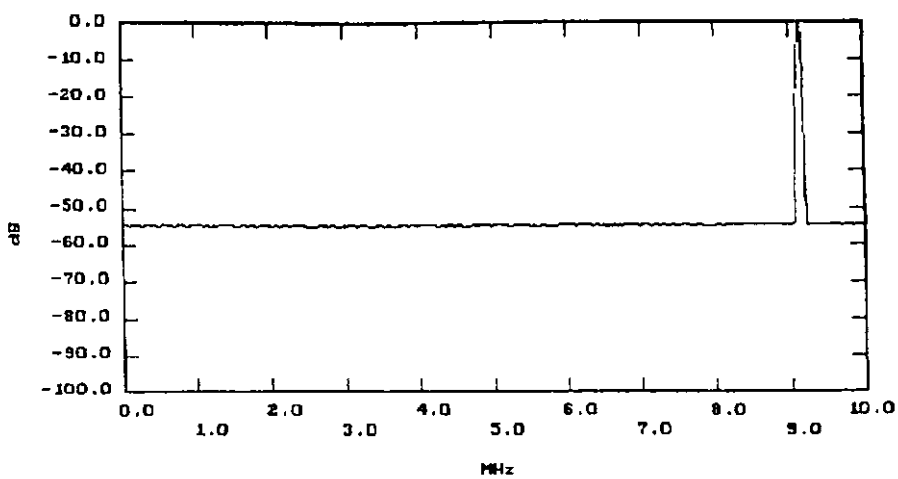

Figure 60: Simulation results using a four term Blackman-Harris window ($E_B = 2$), a sampling frequency of 20 MHz, N=1024, f_0=4,567,890 Hz and σ_r =0.01. (From [79].)

The question is: with so many noise sources present, how does one utilize these results? To determine if clock jitter is the dominant source, two input frequencies are used where one is half of the other and perform spectral averaging. If the noise floor drops by 3 dB when the input frequency is reduced by one-half, then the jitter is dominant. If the noise floor does not move at all, then other noise sources (thermal, quantization) are far more significant.

11.1.6 Other Jitter Models

Other models for estimation of jitter have been proposed. The model described in Ref. [80] assumes the total jitter is composed of sampling circuit jitter, analog input signal jitter, and sampling clock jitter. Using this model, the jitter is broken up into three components. To evaluate the model a precise method for measuring jitter is devised. The method does not require precise delay adjustments between the analog input signal and the sampling clock, because it is based on sampled sine-wave SNR calculations. The accuracy and speed limitations of converters are also discussed and it is shown that the jitter suppression bandwidth is important for the design of high-precision, high-speed converters. Further work by [81] has shown that measuring the SNR of jittered sinusoids agrees more accurately with simulations when the sinusoid is described by two complex exponentials rather than by one complex exponential. This work also shows that the amplitude statistics are very sensitive to the Taylor series approximation used.

Due to the interest in higher order spectra, investigation of the effect of sampling jitter on the discrete higher-than-order-two spectra has also been reported [82, 83]. In this work results concerning the bispectrum (third order spectrum) are reported. Expressions for the bispectrum of sampled data under the assumption that the timing errors are independently identically distributed random variables. It is shown that, while the discrete bispectrum of a uniformly sampled third order stationary signal is zero in a triangle that is a proper subset of the principal domain, it differs from zero in the presence of jitter. Exploiting this effect, a test for the detection of sampling jitter and estimating it variance is presented. Also the application of the Dirichlet transform has been used in the analysis of nonuniformly sampled signals [84]. The Dirichlet transform is well suited to the analysis of nonuniform samples since the spectrum preserves information about sampling instants because a nonuniformly sampled signal is not treated as a sequence of samples but as a function of the sampling instants (unlike the Z-transform). This work presents the basic properties of the Dirichlet transform and the inverse Dirichlet transform in the analysis of nonuniformly sampled signals.

11.2 Reconstruction of Signals from Nonuniform Samples

The ability to recover the original signal from the nonuniform optical samples can help relax the requirements on the mode-locked laser sampling jitter. Reconstruction of a lowpass signal from the samples containing jitter (nonuniform samples) can be accomplished using iterative techniques [85–88]. Given the nonuniform samples $x_s(t) = \sum_I x(t_I)\delta(t - t_I)$ where $\{t_k\}$ is a stable sampling set, the following iterative method will recover the band-limited finite energy signal $x(t)$ from $x_s(t)$, i.e.,

$$x_{k+1}(t) = \lambda PSx(t) + (P - \lambda PS)x_k(t) \tag{115}$$

where $\lambda, x(t)$ and $x_k(t)$ are a convergence constant, the original finite energy signal and the kth iteration, respectively. P and S are respectively, the band limiting and ideal nonuniform sampling operators. $PSx(t)$ is the lowpass filtered version of the ideal nonuniform samples which is known. This process will converge to a stable point which is equal to the desired signal x. The iterative method can also be implemented in a feedback system as discussed in [87]. Recovery of a bandpass

signal from a set of nonuniform samples is discussed in [88]. If the nonuniform sampling set $\{t_k\}$ satisfies certain conditions, then the nonuniform samples of the complex extension of a bandpass signal $x^c(t) = A(t)e^{j[\omega_c t+\phi(t)]}$ where $A(t)$ is the envelope and $\omega_c = 2\pi f_c$ is the central frequency of the bandpass signal uniquely determines the bandpass signal. The Lagrange interpolation formula is

$$x^c(t) = \sum_k x^c(t_k)e^{j\omega_c(t-t_k)}\psi_k(t) \tag{116}$$

where $\psi_k(t)$ is the Lagrange interpolation function [85]. These methods are currently being studied for direct application to the optical sampling methods described.

11.3 Summary of Optical Signal Processing

When sampling wideband signals with optical pulses, a number of constraints are placed on the laser performance such as the pulse repetition frequency (PRF), the optical pulse width and the variation in sampling time (or jitter). The hardest specification to meet with these types of sampling lasers is the jitter requirement. To amplitude analyze the amplitude modulated laser pulse into a number of quantization levels, extremely small jitter times must be achieved (e.g., 50 fs). In Part II, several algorithms and optical signal processing concepts have been described that attempt to relax this stringent jitter requirement. Both integrated and bulk optic oversampling architectures have been investigated. Oversampling architectures integrate out the errors resulting from sampling jitter and take advantage of the availability of high PRF lasers. To investigate the detection of frequencies that are above the Nyquist rate $f_s/2$, an optical DFT 2-channel receiver has been investigated. This optical receiver concept explores the relationship of the optical DFT and the symmetrical number system in resolving the frequency ambiguities that arise due to undersampling a wideband signal. Finally, non-uniform sampling theory has been investigated in order to estimate the jitter component present in the spectrum of a sampled signal. Relationships are given for estimating the jitter from both the magnitude and magnitude squared spectrum. An investigation into a set of iterative algorithms to remove the jitter from the samples has also been initiated.

Part III
Appendices

A Review of Derivations

The following derivation is taken from Ref. [1].

A.1 System Jitter

We want to find the error due to a mislocation of the sampling time. Suppose that a sampling pulse is expected at time $t_{i+1} = t_i + \Delta t$, but, instead, it arrives at $t_{i+1} = t_i + \Delta t' = t_i + \Delta t + \delta t$. Suppose, also, that we are trying to sample a sine-wave signal of the form $V = A\sin(2\pi f_m t)$. (The frequency f_m is going to be the maximum frequency in the signal.) An error voltage will result, given by

$$\delta V = A\{\sin\left[(2\pi f_m(t_i + \Delta t')\right] - \sin\left[(2\pi f_m(t_i + \Delta t')\right]\} \ . \tag{117}$$

For small values of δt, this reduces to

$$\delta V = 2\pi f_m A\,\delta t \cos\left[2\pi f_m(t_i + \Delta t)\right] \ . \tag{118}$$

The maximum magnitude for this error voltage is

$$|\delta V_{\max}| = 2\pi f_m A\,\delta t_{\max} \ . \tag{119}$$

We note that $\delta t_{\max}$ is the maximum timing error that is expected.

We require that the voltage error in the ADC be less than one half of the voltage corresponding to the least significant bit of the convertor, i.e.,

$$|\delta V_{\max}| \leq \frac{\Delta V}{2} = \frac{1}{2}\left(\frac{2A}{2^N}\right) = \frac{A}{2^N} \ . \tag{120}$$

Hence, we want to ensure that the timing error is

$$\delta t_{\max} \leq \frac{1}{2^{N+1}\pi f_m} \ . \tag{121}$$

This is Eq. 2 in this report.

A.2 System pulse width

The maximum error due to the finite pulse width of the sampling pulse, ΔT, is also obtained by considering a voltage signal of the form $V = Asin(2\pi f_m t)$. The error in the voltage at a sampling time t_i is

$$\delta V = \int_{t_i-(\Delta T/2)}^{t_i+(\Delta T/2)} \frac{A\sin(2\pi f_m t)}{\Delta T} dt - A\sin(2\pi f_m t_i) \ , \tag{122}$$

where ΔT is the duration of the interaction (i.e., the duration of the optical pulse plus the optical transit time of the modulator's electrodes). A Taylor expansion for the sine wave about t_i is

$$\sin 2\pi f_m t) = \sin(2\pi f_m t_i) + 2\pi f_m \cos(2\pi f_m t_i)\,(t - t_i) + \frac{(2\pi f_m)^2 \cos(2\pi f_m t_i)\,(t - t_i)^2}{2} + \ldots \tag{123}$$

Inserting the expansion into Eq. 122 and evaluation of the integral gives (to the lowest order of ΔT),

$$\delta V = \frac{(2\pi f_m \Delta T)^2 A \sin(2\pi f_m t_i)}{6}\,. \tag{124}$$

The maximum value of this error is

$$\delta V_{\max} = \frac{(2\pi f_m \Delta T)^2 A}{6}\,. \tag{125}$$

requiring that the maximum error be less than one-half of $\Delta V/2$ gives

$$\Delta T \leq \frac{\sqrt{3}}{\pi f_m \sqrt{2^{N-1}}}\,. \tag{126}$$

This was introduced as Eq. 3 earlier in this report. For example, if $N = 6$ and $f_m = 300$ MHz, then $\delta T \leq 325$ ps. For a lithium-niobate modulator ($n = 2.18$) and the transit time is 73 ps per cm of modulator electrode. If this length were 3.4 cm, the transit time is 247 ps, so the pulse width would be 78 ps ($= 325 - 78$ ps).

B Review of Autocorrelator Measurements

The following section summarizes the use of an optical autocorrelator to estimate the pulse duration of a short pulse. It follows the treatment found in Ref. [89]. Figure 6 show the layout of the correlator. The key is in the generation of the second-harmonic component in the crystal. If an optical pulse of the form

$$e_1(t) = \mathrm{Re}[E_1(t)e^{j\omega t}]\,, \tag{127}$$

is incident on a nonlinear crystal, it generates an output pulse $e_2(t)$ at twice the frequency, given by

$$e_2(t) = \mathrm{Re}[E_2(t)e^{j2\omega t}] \propto \mathrm{Re}[E_1^2(t)e^{j2\omega t}]\,. \tag{128}$$

In our correlator, we will have two pulses present, one original pulse and one pulse that is advanced (or delayed) by τ seconds due to the path length delays of the interferometer. Here,

$$\tau = \frac{n\Delta L}{c}\,, \tag{129}$$

where n is the index of the path difference (frequently air), ΔL is the path difference between the two paths in the interferometer, and c is the vacuum speed of light. Hence, we find the total wave in the crystal, E_{total}, as

$$E_{\mathrm{total}} = \mathrm{Re}\left\{[E_1(t) + E_1(t-\tau)e^{-j\omega\tau}]e^{j\omega t}\right\} = \mathrm{Re}[E_{\mathrm{total}}(t)e^{j\omega t}] \tag{130}$$

and, so, we find that

$$E_{\mathrm{total}}(t) = E_1(t) + E_1(t-\tau)e^{j\omega\tau}\,. \tag{131}$$

According to Eq. 128, the amplitude of the second-harmonic is proportional to the square of the amplitude of the total incident wave, so

$$\begin{aligned} E_2(t) \quad &\propto \quad [E_1(t) + E_1(t-\tau)e^{-j\omega\tau}]^2 \\ &= E_1^2(t) + E_1^2(t-\tau)e^{-j2\omega\tau} + 2E_1(t)E_1(t-\tau)e^{-j\omega\tau} \end{aligned} \tag{132}$$

The output of the crystal, $e_2(t) = \mathrm{Re}[E_2(t)e^{j2\omega t}]$, is incident on a photomultiplier (with an optical filter to block any residue of the incident light). The output current of the detector, $i_d(t)$, is proportional to the intensity of the incident light, or

$$i_d(t) \propto E_2(t)E_2^*(t) = [E_1(t)E_1^*(t)]^2 + [E_1(t-\tau)E_1^*(t-\tau)]^2 + 4E_1(t)E_1^*(t)E_1(t-\tau)E_1^*(t-\tau) + s(t)\,, \tag{133}$$

where the $s(t)$ term contains terms with $\cos\omega t$ and $\cos 2\omega t$ dependencies. Since these terms are oscillating at optical frequencies, the detector is unable to keep up them and they drop out due to the integrating effect of the detector. The temporal (t) scale of the other three terms is on the order of the pulse width (picoseconds at most for our modelocked lasers). The detector will integrate out this time behavior, leaving only the delay time, so

$$i_d(t) \propto < I^2(t) > + < I^2(t-\tau) > +4 < I(t)I(t-\tau) >\,, \tag{134}$$

where the brackets indicate time averaging and the *intensity* of the wave is defined as $I(t) = E_1(t)E_1^*t$. We note that shifting the square of an intensity does not change its average value, so $< I^2(t) >=< I^2(t-\tau >$. Using this and dividing both sides of Eq. 134 by $< I^2(t) >$ gives

$$i_d'(t) = 1 + 2G^{(2)}(\tau)\,, \tag{135}$$

where $G^{(2)}(\tau)$ is the *second-order correlation* of the intensity pulse, defined by

$$G^{(2)}(\tau) \equiv \frac{< I(t)I(t-\tau) >}{< I^2(t) >}\,. \tag{136}$$

If τ is zero, we note that $G^{(2)}(0) = 1$ and $i_d(0) = 3$. If τ is large, we expect $G^{(2)}(\tau)$ to be zero and $i_d(\tau)$ to be 1. Hence, if the input pulse is an ideal square pulse of coherent light, then the ideal autocorrelation would look like Fig. 61a. The autocorrelation peak is 3 and the curve trails off to a pedestal with a value of 1.

It is useful to determine the expected response from a series of partially coherent pulses (e.g., a set of pulses from a laser operating with a large number of independent modes). We still have that, when $\tau = 0$, $G^{(2)}(0) = 1$. When τ exceeds the coherence time of the source, we have

$$G^{(2)}(\tau) = \frac{< I(t)I(t-\tau) >}{< I^2(t) >} = \frac{< I(t) >^2}{< I^2(t) >} \tag{137}$$

since $I(t)$ and $I(t-\tau)$ are uncorrelated. In order to find $< I^2(t) >$ we recognize that, for truly incoherent light, we can replace the time averaging by ensemble averaging, i.e., we have

$$< I^2(t) >= \int_0^\infty p(I)I^2\, d \tag{138}$$

where $p(I)$ is the intensity probability distribution so that $p(I)\, d$ is the probability of finding an intensity between I and $I + d$. For incoherent light, $p(I) = e^{I/<I>}/ < I >$ [89]. Substituting this into Eq. 138 gives the result that

$$< I^2(t) >= 2 < I(t) >^2\ . \tag{139}$$

Using this in Eq. 135 gives

$$i'_{\mathrm{d,incoherent}}(\tau > 0) \propto 1 + 2\frac{< I(t) >^2}{< I^2(t) >} = 2\,. \tag{140}$$

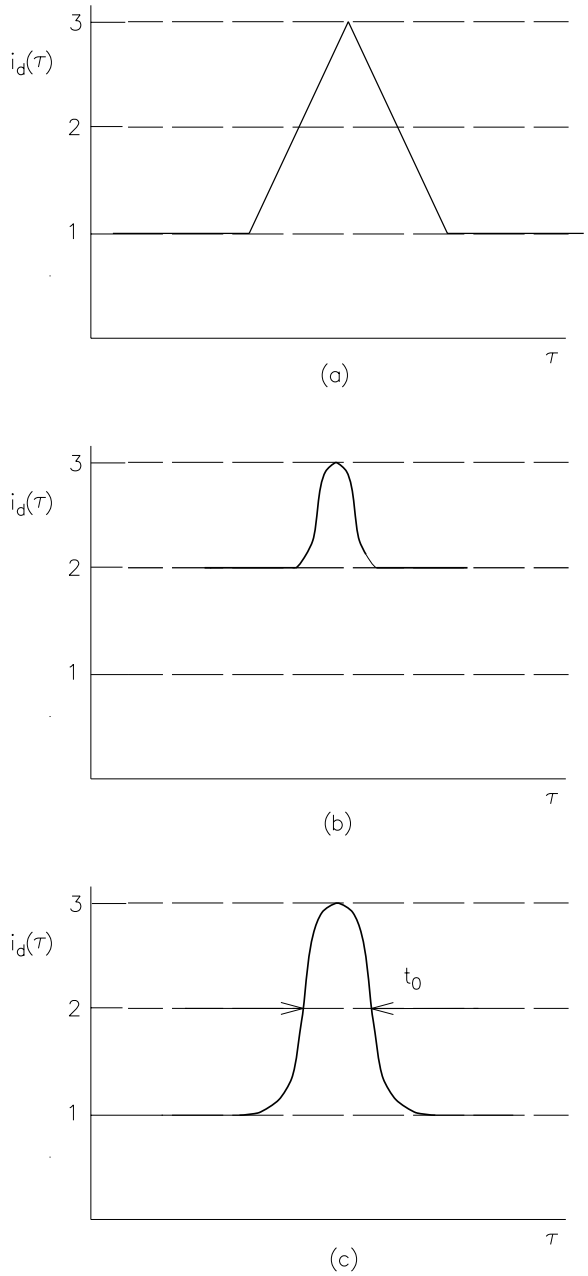

Figure 61: Representative autocorrelation curves. (a) Ideal square coherent pulse. (b) Partially coherent pulse. (c) Representative coherent pulse, showing location of pulse width measurement.

$I(t)$	t_0/τ_0
$\mathrm{rect}(t/t_0)$	1
$\exp\left\{-\frac{(4\ln 2)t^2}{\tau_0^2}\right\}$	$\sqrt{2}$
$\mathrm{sech}^2\left(\frac{1.76t}{\tau_0^2}\right)$	2

Table 11: Ratio of autocorrelation width to intensity pulse width for three standard mathematical representations of optical pulses.

Hence, the autocorrelation curve for a weakly coherent source looks like that in Fig. 61b. While the value at zero delay is still 3, the curve rapidly falls off to a pedestal value of 2 (rather than the value of 1 achieved by coherent light.

The determination of the pulse width of the original pulses, τ_0 from the measured width of the autocorrelation curve, t_0, can be determined from Eq. 137 on page 79. (Note that the width of the autocorrelation curve is taken as the full-width at the half-maximum values *disregarding the value of the pedestal*. Table 11 [89] shows value of t_0/τ_0 for three "standard" waveforms. The first wave is an ideal square pulse with zero rise and fall times and a width of τ_0; it is not reached in practice, but is used because it simplifies computations and represents the ideal limit for a modelocked pulse. The second wave is a pulse with Gaussian temporal shape; it represents a good approximation to the output from modelocked lasers that do not implement any pulse compression or soliton generation. The third standard wave represents the ideal output of a soliton laser; it is a good approximation to modelocked lasers that implement pulse compression techniques within their operation. Obviously there is some ambiguity in choosing which waveform to use to determine the ratio of widths. If the user does not want to choose a pulse shape, some curve-fitting techniques can be used to match the autocorrelation curve to the theoretical autocorrelation of the curves.

C Characteristic Functions

Recall from the probability theory that the characteristic function for a continuous random variable is defined as

$$\Phi(\omega) = \int_{-\infty}^{\infty} f(x) e^{j\omega x} dx\,. \tag{141}$$

This is the Fourier transform with the sign of ω reversed. Also note that the original function can be recovered as

$$f(x) = \frac{1}{2\pi}\int_{-\infty}^{\infty} \Phi(\omega) e^{-j\omega x}\, d\omega \tag{142}$$

which is the inverse Fourier transform with the sign of x reversed. Also,

$$\Phi(-\omega) = \int_{-\infty}^{\infty} f(x) e^{-j\omega x}\, dx\,. \tag{143}$$

The characteristic function has essentially the same properties as the Fourier transform and has a maximum at the origin because $f(x) \geq 0$.

$$|\Phi(\omega)| \leq \Phi(0) = 1 \tag{144}$$

$$\Phi(\omega) = E\left\{e^{j\omega x}\right\} \tag{145}$$

If $y = ax + b$ then

$$\Phi_y(\omega) = e^{jb\omega} E\left\{e^{ja\omega x}\right\} \tag{146}$$

Part IV
Bibliography

References

[1] H. F. Taylor, "An optical analog-to-digital converter—Design and analysis," *IEEE J. Quantum Electronics*, vol. QE-15, no. 4, pp. 210–216, 1979.

[2] I. Duling, III, "Subpicosecond all-fibre erbium laser," *Electronics Letters*, vol. 27, no. 6, pp. 544–545, 1991.

[3] I. Duling, III, C.-J. Chen, P. Wai, and C. Menyuk, "Operation of a nonlinear loop mirror in a laser cavity," *IEEE J. Quantum Electronics*, vol. 30, no. 1, pp. 194–199, 1994.

[4] I.N. Duling, III and R. Esman, "Single-polarisation fibre amplifier," *Electronics Letters*, vol. 28, no. 12, pp. 1126–1128, 1992.

[5] T. Carruthers, I.N. Duling III, and M. Dennis, "Active-passive modelocking in a single-polarisation erbium fibre laser," *Electronics Letters*, vol. 30, no. 13, pp. 1051–1053, 1994.

[6] T. F. Carruthers and I. N. Duling III, "10-GHz, 1.3-ps erbium fiber laser employing soliton pulse shortening," *Optics Letters*, vol. 21, no. 23, pp. 1927–1929, 1996.

[7] D. Foursa, P. Emplit, R. Leners, and L. Meulman, "18 GHz from a σ-cavity Er-fibre laser with dispersion management and rational harmonic mode-locking," *Electronics Letters*, vol. 33, no. 6, pp. 486–488, 1997.

[8] I. N. Duling, III, "Mode locked figure eight lasers," in *LEOS '93 Conference proceedings*, (New York), pp. 270–271, IEEE, 1993.

[9] K. Tamura, E. Ippen, H. Haus, and L. Nelson, "77-fs pulse generation from a stretched-pulse mode-locked all-fiber ring laser," *Optics Letters*, vol. 18, no. 13, pp. 1080–1082, 1993.

[10] H. Haus, E. Ippen, and K. Tamura, "Additive-pulse modelocking in fiber lasers," *IEEE J. Quantum Electronics*, vol. 30, no. 1, pp. 200–208, 1994.

[11] H. Haus, K. Tamura, L. Nelson, and E. Ippen, "Stretched-pulse additive pulse mode-locking in fiber ring lasers: theory and experiment," *IEEE J. Quantum Electronics*, vol. 31, no. 3, pp. 591–598, 1995.

[12] F. Kärtner, D. Kopf, and U. Keller, "Solitary-pulse stabilization and shortening in actively mode-locked lasers," *J. Optical Soc. of America B*, vol. 12, no. 3, pp. 486–496, 1995.

[13] D. Kuizenga and A. Siegman, "FM and AM mode locking of the homogeneous laser—Part I: Theory," *IEEE J. Quantum Electronics*, vol. QE-6, pp. 694–708, 1970.

[14] D. Walker, D. Crust, W. Sleat, and W. Sibbet, "Reduction of phase noise in passively mode-locked lases," *IEEE J. Quantum Electronics*, vol. 28, no. 1, pp. 289–296, 1992.

[15] D. von der Linde, "Characterization of the noise in continuously operating mode-locked lasers," *Applied Physics B*, vol. 39, pp. 201–217, 1986.

[16] M. J. Rodwell, D. M. Bloom, and K. J. Weingarten, "Subpicosecond laser timing stabilization," *IEEE J. Quantum Electronics*, vol. 25, no. 4, pp. 817–827, 1989.

[17] U. Keller, K. D. Li, M. Rodwell, and D. M. Bloom, "Noise characterization of femtosecond fiber Raman soliton lasers," *IEEE J. Quantum Electronics*, vol. 25, no. 3, pp. 280–288, 1989.

[18] M. Rodwell, K. Weingarten, D. Bloom, T. Baer, and B. Kolner, "Reduction of timing fluctuations in a mode-locked Nd:YAG laser by electronic feedback," *Optics Letters*, vol. 11, no. 10, pp. 638–640, 1986.

[19] K. S. Giboney, S. T. Allen, M. J. Rodwell, and J. E. Bowers, "Picosecond measurements by free-running electro-optic sampling," *IEEE Photonics Technology Letters*, vol. 6, no. 11, pp. 1353–1355, 1994.

[20] M. Fermann, M. Hofer, F. Haberl, and S. Craig-Ryan, "Femtosecond fibre laser," *Electronics Letters*, vol. 26, no. 20, pp. 1737–1738, 1990.

[21] K. Smith, J. Armitage, R. Wyatt, N. Doran, and S. Kelly, "Erbium fibre soliton laser," *Electronics Letters*, vol. 26, no. 15, pp. 1149–1151, 1990.

[22] R. Davey, N. Langford, and A. Feurguson, "Subpicosecond pulse generation from erbium doped fibre laser," *Electronics Letters*, vol. 27, no. 9, pp. 726–728, 1991.

[23] F. Haberl, M. Ober, M. Hofer, M. Fermann, E. Wintner, and A. Schmidt, "Low-noise operation modes of a passively mode-locked fiber laser," *IEEE Photonics Technology Letters*, vol. 3, no. 12, pp. 1071–1073, 1991.

[24] D. Richardson, R. Laming, D. Payne, V. Matsas, and M. Phillips, "Selfstarting, passively modelocked erbium fibre ring laser based on the amplifying Sagnac switch," *Electronics Letters*, vol. 27, no. 6, pp. 542–544, 1991.

[25] D. Richardson, R. Laming, D. Payne, M. Phillips, and V. Matsas, "320 fs soliton generation with passively mode-locked erbium fibre laser," *Electronics Letters*, vol. 27, no. 9, pp. 730–732, 1991.

[26] M. Dennis and I. Duling III, "High repetition rate figure eight laser with extracavity feedback," *Electronics Letters*, vol. 28, no. 20, pp. 1894–1896, 1992.

[27] F. Fontana, G. Grasso, N. Manfredini, M. Romagnoli, and B. Daino, "Generation of sequences of ultrashort pulses in erbium doped fibre single ring lasers," *Electronics Letters*, vol. 28, no. 1, pp. 1291–1293, 1992.

[28] X. Shan, D. Cleland, and A. Ellis, "Stabilising Er fibre soliton laser with pulse phase locking," *Electronics Letters*, vol. 28, no. 2, pp. 182–184, 1992.

[29] K. Tamura, H. Haus, and E. Ippen, "Self-starting additive pulse mode-locked erbium fibre ring laser," *Electronics Letters*, vol. 28, pp. 2226–2227, 1992.

[30] S. Arahira, Y. Matsui, T. Kunii, S. Oshiba, and Y. Ogawa, "Optical short pulse generation at high repetition rate over 80 GHz from a monolithic passively modelocked DBR laser diode," *Electronics Letters*, vol. 29, no. 11, pp. 1013–1015, 1993.

[31] R. Davey, N. Langford, and A. Feurguson, "Role of polarisation rotation in the modelocking of an Er fibre laser," *Electronics Letters*, vol. 29, no. 9, pp. 758–760, 1993.

[32] E. DeSouza, C. Soccolich, W. Pleibel, R. Stolen, J. Simpson, and D. DiGiovanni, "Saturable absorber modelocked polarization maintaining erbium-doped fibre laser," *Electronics Letters*, vol. 29, no. 5, pp. 447–449, 1993.

[33] F. Fontana, G. Bordogna, P. Franco, M. Midrio, and M. Romagnoli, "Conditions for soliton generation in harmonically modelocked erbium-doped fibre lasers," *Electronics Letters*, vol. 29, no. 18, pp. 1652–1654, 1993.

[34] M. Nakazawa, E. Yoshida, and Y. Kimura, "Generation of 98 fs optical pulses directly from an erbium-doped fibre ring laser at 1.57 μm," *Electronics Letters*, vol. 29, no. 1, pp. 63–65, 1993.

[35] D. Noske, A. Boskovic, M. Guy, and J. Taylor, "Synchronously pumped, picosecond, ytterbium-erbium fibre laser," *Electronics Letters*, vol. 29, no. 21, pp. 1863–1864, 1993.

[36] H. Takara, S. Kawanishi, and M. Saruwatari, "20 GHz transform-limited optical pulse generation and bit-error-free operation using a tunable, actively modelocked Er-doped fibre ring laser," *Electronics Letters*, vol. 29, no. 13, pp. 1149–1150, 1993.

[37] K. Williams, D. Burns, I. White, W. Sibbett, and M. Fice, "Picosecond pulse generation with ultralow jitter in 1.5-μm multicontact MQW lasers using Q-switching," *IEEE Photonics Technology Letters*, vol. 5, no. 8, pp. 867–869, 1993.

[38] A. Deryagin, D. Kusenkov, V. Kuchinskii, E. Portnoi, and I. Khrushev, "Generation of 110 GHz train of subpicosecond pulses in 1.535 μm spectral region by passively modelocked InGaAsP/InP laser diode," *Electronics Letters*, vol. 30, no. 4, pp. 309–311, 1994.

[39] F. Fontana, L. Bossalini, P. Franco, M. Midrio, M. Romagnoli, and S. Wabnitz, "Self-starting sliding-frequency fibre soliton laser," *Electronics Letters*, vol. 30, no. 4, pp. 321–322, 1994.

[40] E. Greer, Y. Kimura, S. K, E. Yoshida, and M. Nakazawa, "Generation of 1.2 ps, 10 GHz pulse train from all-optically modelocked, erbium fibre ring laser with active nonlinear polarisation rotation," *Electronics Letters*, vol. 30, no. 21, pp. 1764–1765, 1994.

[41] M. Nakazawa, E. Yoshida, and Y. Kimura, "Ultrastable harmonically and regenratively modelocked polarisation-maintainig erbium fibre ring laser," *Electronics Letters*, vol. 30, no. 19, pp. 1603–1605, 1994.

[42] M. Nakazawa, E. Yoshida, H. Kubota, and Y. Kimura, "Generation of 170 fs, 10 GHz transform-limited pulse train at 1.55 μm using a dispersion-decreasing, erbium-doped active soliton compressor," *Electronics Letters*, vol. 30, no. 24, pp. 2038–2040, 1994.

[43] D. Pataca, M. Rocha, K. Smith, T. Whitely, and R. Wyatt, "Actively modelocked Pr^{3+}-doped fluoride fibre laser," *Electronics Letters*, vol. 30, no. 12, pp. 964–965, 1994.

[44] D. Patrick, "Modelocked ring laser using a nonlinearity in a semiconductor laser amplifier," *Electronics Letters*, vol. 30, no. 1, pp. 43–44, 1994.

[45] D. Peter, G. Onishchukov, W. Hodel, and H. Weber, "570 fs pulses from a Pr^{3+}-doped fibre laser modelocked by pump pulse induced cross-phase modulation," *Electronics Letters*, vol. 30, no. 19, pp. 1595–1596, 1994.

[46] M. Fermann, K. Sugden, and I. Bennion, "Generation of 10 nj picosecond pulses from a modelocked fibre laser," *Electronics Letters*, vol. 31, no. 3, pp. 194–195, 1995.

[47] S. Gray, A. Grudinin, W. Loh, and D. Payne, "Femtosecond harmonically mode-locked fibre laser with time jitter below 1 ps," *Optics Letters*, vol. 20, no. 2, pp. 189–191, 1995.

[48] S. Namiki, C. Yu, K. Tamura, H. Haus, and E. Ippen, "Noise characteristics of a polarization additive pulse modelocked fiber ring laser," in *IEEE Lasers and Electro-optics Society 1995 Annual Meeting Proceedings*, (New York), pp. 214–215, IEEE, 1995.

[49] H. Takara, S. Kawanishi, and M. Saruwatari, "Stabilisation of a modelocked er-doped fibre laser by supressing the relaxation oscillation frequency component," *Electronics Letters*, vol. 31, no. 4, pp. 292–293, 1995.

[50] E. Yamada, E. Yoshida, T. Kitoh, and M. Nakazawa, "Generation of terabit per second optical data pulse train," *Electronics Letters*, vol. 31, no. 16, pp. 1342–1344, 1995.

[51] E. Yoshida, Y. Kimura, and M. Nakazawa, "20 GHz, 1.8 ps pulse generation from a regeneratively modelocked erbium-doped fibre laser and its femtosecond compression," *Electronics Letters*, vol. 31, no. 5, pp. 377–378, 1995.

[52] J. Yu, D. Huhse, M. Schell, M. Schulze, D. Bimberg, J. Williams, L. Zhang, and I. Bennion, "Fourier-transform-limited 2.5 ps light pulses with electrically-tunable wavelength (15 nm) by hybridly modelocking a semiconductor laser in a chirped Bragg graing fibre external cavity," *Electronics Letters*, vol. 31, no. 23, pp. 2008–2009, 1995.

[53] M. Nakazawa and E. Yoshida, "Direct generation of a 750 fs, 10 GHz pulse train from a regenerativey mode-locked fibre laser with multiple harmonic modulation," *Electronics Letters*, vol. 32, no. 14, pp. 1291–1293, 1996.

[54] M. Nakazawa, E. Yoshida, and K. Tumura, "10 GHz 2 ps regeneratively and harmonically FM modelocked erbium fibre ring laser," *Electronics Letters*, vol. 32, no. 14, pp. 1285–1287, 1996.

[55] X. Shan and D. Spirit, "Novel method to suppress noise in harmonically modelocked erbium fibre lasers," *Electronics Letters*, vol. 29, no. 11, pp. 979–981, 1996.

[56] E. Yoshida and M. Nakazawa, "80–200 GHz erbium doped fibre laser using a rational harmonic modelocking technique," *Electronics Letters*, vol. 32, no. 15, pp. 1370–1372, 1996.

[57] J. Candy and G. Temes, "Oversampling methods for A/D and D/A conversion,," in *Oversampling Delta-Sigma Data Converters*, pp. 1–29, New York: IEEE Press, 1992.

[58] R. van de Plassche, *Integrated Analog-to-Digital and Digital-to-Analog Data Converters.* New York: Kluwer, 1994.

[59] B. P. Agrawal and K. Shenoi, "Design methodology for $\sigma\delta$m," *IEEE Trans. on Communications*, vol. COM–31, no. 3, pp. 360–370, 1983.

[60] B. E. Boser and B. A. Wooley, "The design of sigma–delta modulation analog–to–digital convertors," *IEEE J. of Solid–State Circuits*, vol. 23, no. 6, pp. 1298–1308, 1988.

[61] P. Pace, S. Ying, J. Powers, and R. Pieper., "Integrated optical sigma-delta modulators," *Optical Engineering*, vol. 35, no. 7, pp. 1828–1836, 1996.

[62] P. E. Pace and D. Styer, "High–resolution encoding process for an integrated optical analog–to–digital converter," *Optical Engineering*, vol. 33, no. 8, pp. 2638–2645, 1994.

[63] S. Ying, "Integrated optical sigma-delta modulators," Master's thesis, Naval Postgraduate School, December 1995.

[64] A. F. Atherton, "Integrated optical fiber lattice accumulator," Master's thesis, Naval Postgraduate School, March 1997.

[65] C. H. E and R. Minasian, "A solution to the synthesis problem of recirculating optical delay line filters," *IEEE Photonics Technology Letters*, vol. 6, no. 7, pp. 833–835, 1994.

[66] J. Capmany and J. Cascon, "Direct form fiber-optic discrete-time signal processors using optical amplifiers and embedded Mach-Zehnder structures," *IEEE Photonics Technology Letters*, vol. 5, no. 7, pp. 842–844, 1993.

[67] B. Moslehi, J. Goodman, M. Tur, and H. Shaw, "Fiber-optic lattice signal processing," *Proc. IEEE*, vol. 72, no. 7, pp. 909–930, 1984.

[68] K. Jackson, S. Newton, B. Moslehi, M. Tur, C. Cutler, J. Goodman, and H. Shaw, "Optical fiber delay–line signal processing," *IEEE Trans. Microwave Theory Tech.*, vol. MTT–33, no. 3, pp. 193–210, 1985.

[69] S. Ardalan and J. Paulos, "An analysis of nonlinear behavior in delta-sigma modulators," *IEEE Trans. Circuits and Systems*, vol. CAS-34, no. 6, pp. 593–603, 1987.

[70] B. Shoop and J. Goodman, "Optical oversampled analog-to-digital conversion," *Applied Optics*, vol. 31, no. 26, pp. 5654–5660, 1992.

[71] B. Shoop, "Second-order cascaded optical error diffusion modulators for oversampled analog-to-digital converters," *Optics Communications*, vol. 102, pp. 125–132, 1993.

[72] B. Shoop and J. Goodman, "A first-order error diffusion modulator for optical oversampled A/D conversion," *Optics Communications*, vol. 97, pp. 167–172, 1993.

[73] P. Pace, R. Leino, and D. Styer., "Use of the symmetrical number system in resolving single-frequency undersampling aliases," *IEEE Trans Signal Processing*, vol. 45, no. 5, pp. 1153–1154, 1997.

[74] P. Pace, P. Ramamoorthy, and D. Styer, "A preprocessing architecture for resolution enhancement in high-speed analog-to-digital converters," *IEEE Trans. on Circuits and Systems*, vol. 41, no. 6, pp. 373–379, 1994.

[75] J. Reif and A. Tyagi, "Efficient parallel algorithms for optical computing with the discrete Fourier transform (DFT) primitive," *Applied Optics*, vol. 36, no. 29, pp. 7327–7340, 1996.

[76] L. Zhang and L. Liu, "Incoherent optical implementation of 2-d complex discrete Fourier transform and equivalent 4-f system," *Optics Communications*, vol. 74, no. 5, pp. 295–300, 1990.

[77] J. Proakis and D. Manolakis, *Digital Signal Processing.* New York: Macmillan Publishing, 1992.

[78] Y.-C. Jenq, "Digital spectra of nonuniformly sampled signals: fundamentals and high-speed waveform digitizers," *IEEE Trans. Instrumentation and Measurement*, vol. 37, no. 2, pp. 245–251, 1988.

[79] Y.-C. Jenq, "Digital spectra of nonuniformly sampled signals: Theories and applications — Measuring clock/aperture jitter of an A/D system," *IEEE Trans. Instrumentation and Measurement*, vol. 39, no. 6, pp. 969–971, 1990.

[80] M. Shinagawa, Y. Akazawa, and T. Wakimoto, "Jitter analysis of high-speed sampling systems," *IEEE J. Solid-State Circuits*, vol. 25, no. 1, pp. 220–224, 1990.

[81] S. wad and M. Wagdy, "More on jitter effects on sinewave measurements," *IEEE Trans. Instrumentation and measurement*, vol. 40, no. 3, pp. 549–552, 1991.

[82] I. Sharfer and H. Messer, "The bispectrum of sampled data: Part i-detection of the sampling jitter," *IEEE Transactions on Signal Processing*, vol. 41, no. 1, pp. 296–312, 1993.

[83] I. Sharfer and H. Messier, "The bispectrum of sampled data: Part ii—Monte Carlo simulations of detection and estimation of the sampling jitter," *IEEE Trans. on Signal Processing*, vol. 42, pp. 2706–2714, 1994.

[84] A. Wojtkiewicz and M. Tuszynski, "Application of the Dirichlet transform in analysis of nonuniformly sampled signals," in *IEEE International Conference on Acoustics, Speech and Signal Processing, Vol. 5*, (New York), pp. 25–28, IEEE Press, 1992.

[85] F. Marvasti, M. Analoui, and M. Gamshadzahi, "Recovery of signals from nonuniform samples using iterative methods," *IEEE Trans. on Signal Processing*, vol. 39, no. 4, pp. 872–878, 1991.

[86] F. Marvasti, C. Liu, and G. Adams, "Analysis and recovery of multidimensional signals from irregular samples using non-linear and iterative techniques," in *Proceedings of the IEEE Custom Integrated Circuits Conference*, (New York), pp. 2445–2448, IEEE Press, 1992.

[87] F. Marvasti and C. Liu, "Feedback implementation of signal recovery from nonuniform samples," *Electronics Letters*, vol. 29, pp. 78–80, 1993.

[88] F. Marvasti, "Nonuniform sampling theorems for bandpass signals at or below the Nyquist density," *IEEE Trans. on Signal Processing*, vol. 44, pp. 572–576, 1996.

[89] A. Yariv, *Optical Electronics in Modern Communications, Fifth Edition*. New York: Oxford University Press, 1997.

INITIAL DISTRIBUTION LIST

		No. Copies
1.	Defense Technical Information Center 8725 John J. Kingman Rd, STE 0944 Ft. Belvoir, VA 22060-6218	2
2.	Dudley Knox Library, Code 52 Naval Postgraduate School 411 Dyer Road Monterey, CA 93943-5101	2
3.	Research Office, Code 09 Naval Postgraduate School 589 Dyer Road Monterey, CA 93943-5138	1
4.	Chairman, Code EC Department of Electrical and Computer Engineering Naval Postgraduate School 833 Dyer Road Monterey, CA 93943-5121	1
5.	Director, Center for Reconnaissance Research, Code EC/Po Department of Electrical and Computer Engineering Naval Postgraduate School 833 Dyer Road Monterey, CA 93943-5121	5
6.	Professor John Powers, Code EC/Po Department of Electrical and Computer Engineering Naval Postgraduate School 833 Dyer Road Monterey, CA 93943-5121	1
7.	Professor P. E. Pace, EC/Pc Department of Electrical and Computer Engineering Naval Postgraduate School 833 Dyer Road Monterey, CA 93943-5121	2
8.	Commanding Officer Naval Research Laboratory Attn: Dr. Tom Carruthers, Code 5670 Optical Sciences Division 4555 Overlook Ave. SW Washington D.C. 20375	1

9. Commanding Officer 1
Naval Research Laboratory
Attn: Dr. Irl Duling III, Code: 5670
Optical Sciences Division
4555 Overlook Ave. SW
Washington D.C. 20375

10. Commanding Officer 1
Naval Research Laboratory
Attn: Dr. Mike Dennis, Code 5670
Optical Sciences Division
4555 Overlook Ave. SW
Washington D.C. 20375

11. Commanding Officer 1
Naval Research Laboratory
Attn: Dr. William Burns, Code 5671
Optical Sciences Division
4555 Overlook Ave. SW
Washington D.C. 20375